A NUMERICAL STUDY OF HEAT AND MOMENTUM TRANSFER OVER A BANK OF FLAT TUBES

A Dissertation

by

HAITHAM M. S. BAHAIDARAH

Submitted to the Office of Graduate Studies of
Texas A&M University
in partial fulfillment of the requirements for the degree of

DOCTOR OF PHILOSOPHY

August 2004

Major Subject: Mechanical Engineering

A NUMERICAL STUDY OF HEAT AND MOMENTUM TRANSFER OVER A BANK OF FLAT TUBES

A Dissertation

by

HAITHAM M. S. BAHAIDARAH

Submitted to Texas A&M University
in partial fulfillment of the requirements
for the degree of

DOCTOR OF PHILOSOPHY

Approved as to style and content by:

Nagamangala K. Anand (Co-Chair of Committee)	Hamn-Ching Chen (Co-Chair of Committee)
Je-Chin Han (Member)	Ken Kihm (Member)
	Dennis O'Neal (Head of Department)

August 2004

Major Subject: Mechanical Engineering

ABSTRACT

A Numerical Study of Heat and Momentum

Transfer Over a Bank of Flat Tubes. (August 2004)

Haitham M. S. Bahaidarah, B.S.; M.S., King Fahd

University of Petroleum and Minerals, Saudi Arabia

Co-Chairs of Advisory Committee: Dr. Nagamangala K. Anand
Dr. Hamn-Ching Chen

The present study considers steady laminar two-dimensional incompressible flow over both in-line and staggered flat tube bundles used in heat exchanger applications. The effects of various independent parameters, such as Reynolds number (Re), Prandtl number (Pr), length ratio (L/Da), and height ratio (H/Da), on the pressure drop and heat transfer were studied.

A finite volume based FORTRAN code was developed to solve the governing equations. The scalar and velocity variables were stored at staggered grid locations. Scalar variables (pressure and temperature) and all thermophysical properties were stored at the main grid location and velocities were stored at the control volume faces. The solution to a one-dimensional convection diffusion equation was represented by the power law. The locations of grid points were generated by the algebraic grid generation technique. The curvilinear velocity and pressure fields were linked by the Semi-Implicit Method for Pressure Linked Equations (SIMPLE) algorithm. The line-by-line method,

which is a combination of the Tri-Diagonal Matrix Algorithm (TDMA) and the Gauss-Seidel procedure, was used to solve the resulting set of discretization equations.

The result of the study established that the flow is observed to attain a periodically fully developed profile downstream of the fourth module. The strength increases and the size of the recirculation gets larger as the Reynolds number increases. As the height ratio increases, the strength and size of the recirculation decreases because the flow has enough space to expand through the tube passages. The increase in length ratio does not significantly impact the strength and size of the recirculation.

The non-dimesionalized pressure drop monotonically decreased with an increase in the Reynolds number. In general, the module average Nusselt number increases with an increase in the Reynolds number. The results at Pr = 7.0 indicate a significant increase in the computed module average Nusselt number when compared to those for Pr = 0.7. The overall performance of in-line configuration for lower height ratio (H/Da = 2) and higher length ratio (L/Da = 6) is preferable since it provides higher heat transfer rate for all Reynolds numbers except for the lowest Re value of 25. As expected the staggered configurations perform better than the in-line configuration from the heat transfer point of view.

To

My Parents,

My Wife,

and

My Brothers and Sisters

ACKNOWLEDGEMENTS

First and foremost, thanks and praises go to Almighty God who gave me the power, support, and patience without which I could not have completed this effort.

I would like to express my gratitude and deepest appreciation to my Chair, Dr. N.K. Anand, for his tireless assistance, patience, and guidance during my study at Texas A&M University. I am also grateful to my Co-Chair, Dr. H. Chen, for his understanding of the subject that has helped me successfully accomplish this research. I extend my appreciation to Dr. J.C. Han and Dr. K.D. Kihm for their consideration shown by serving on my advisory committee. I am also grateful to Dr. K.C. Karki for being helpful and willing to discuses his previous thesis. I am also thankful to the staff of the Department of Mechanical Engineering at Texas A&M University for their kind help over the years. I am also grateful to King Fahd University of Petroleum and Minerals who sponsored me during this research.

Finally, to my parents, what can I possibly say? Thirty years of your unconditional and affectionate support cannot adequately be acknowledged in a few lines, if at all. I just want to say that I love you both very much and that I dedicate this dissertation to you. I am also indebted to my lovely wife for all her sacrifices and patience during the past seven years, and thanks goes to my sweet daughter, Layan, and brave son, Al-Hasan, for adding a sugary flavor to my life.

TABLE OF CONTENTS

CHAPTER Page

CHAPTER Page

LIST OF FIGURES

FIGURE Page

FIGURE Page

FIGURE Page

FIGURE Page

FIGURE Page

LIST OF TABLES

TABLE Page

NOMENCLATURE

A	area
a	base vector, coefficients
b	source term coefficient
C_p	specific heat
D	diameter, Diffusional conductance
Da	small diameter
Db	long diameter
e	unit vector
f	friction factor
F	flow rate though control volume
h	metric scale factor, heat transfer coefficient
H	height
J	total flux
Ja	Jacobian of transformation
k	thermal conductivity
L	length
LMTD	Log-Mean Temperature Difference
Nu	Nusselt number
P	Point, Pressure, Peclet number
Q	total heat flux

r	vector
Re	Reynolds number
S	source term, surface
t	time
T	temperature
u, v	Cartesian velocity components, velocity projection
V	velocity vector, volume
x, y, z	Cartesian coordinates
E, W, N, S	adjacent points to the main point P
e, w, n, s	adjacent faces to the main point P

Superscript

*	guessed value
‘	corrected value

Subscript

av	average
b	bulk
H	hydraulic
in	inlet
max	maximum
min	minimum

nb	neighboring points
NO	non-orthogonal
P	primary flux, main point
S	Secondary flux
w	wall

Greek

ξ, η, ζ	Curvilinear coordinates
α	primary area
β	secondary area
Γ	diffusion coefficient
ϕ	general dependent variable
ρ	mass density
μ	viscosity
ν	kinematic viscosity
θ	non-dimensional temperature

CHAPTER I

INTRODUCTION

1.1 Background

Tubular heat exchangers are used in many energy conversion and chemical reaction systems ranging from nuclear reactors to refinery condensers. The most important design variables of tubular heat exchangers are the outside heat transfer coefficient of the tube and the pressure drop of the fluid flowing externally. Based on previous studies reported in the literature, the effects of tube shape and arrangement have indicated that they could have a positive influence on heat transfer (Ota et al., 1984, 1986; Wung et al., 1986).

It has been of interest to many researchers to investigate the fluid flow and heat transfer over objects of different shapes. Flat tubes have not been investigated to the same extent, although they play an important role in many technical applications such as modern heat exchangers and automotive radiators. Flat tube designs have recently been introduced for use in automotive air conditioning evaporators and condensers. Recent developments in automotive brazed aluminum manufacturing technology have made the cost of the flat tube heat exchanger construction more favorable (Webb, 1993).

This dissertation follows the International Journal of Heat and Fluid Flow format.

Flat tube heat exchangers are expected to have lower air-side pressure drop and better air-side heat transfer coefficients compared to circular tube heat exchangers. The pressure drop is expected to be lower than that for circular tubes because of a smaller wake area. For the same reason, vibration and noise is expected to be less in flat tube heat exchangers compared to circular tube heat exchangers.

The development of computers has resulted in the use of numerical simulations of heat and momentum transfer problems in tubular heat exchangers. Numerical analysis of fluid flow and heat transfer in complex geometrical domains has been the focus of quite a few researchers in the past decade. Such flows typically are representative of those situations occurring in a numerous variety of practical engineering problems. Examples can be found in such diverse areas as aerodynamics, meteorology, nuclear reactor design, compact heat exchangers, turbo-machines, and the cooling of electronic packages. The numerical prediction of fluid flow has evolved over the last two decades into an established field known as Computational Fluid Dynamics and often referred to by the acronym CFD.

CFD codes are structured around the numerical algorithms that deal with fluid flow problems. There are four major streams of numerical solution techniques: finite difference, finite volume, finite element, and spectral methods. All numerical methods that form the basis of the solver follow the same steps. These steps are: (1) Domain Discretization: division of the computational domain into several control volumes, location of nodes at the geometric center of the control volumes, and systematic numbering of nodes constitutes domain discretization. Nodes are the locations (points)

where unknowns are calculated. (2) Development of Discretization Equations: in this step the exact mathematical operations, such as partial derivatives, are converted to approximate algebraic expressions at various nodes. (3) Solution of Discretization Equations: A set of linear equations, obtained as a result of step (2), are solved (inverted) to obtain the values of the variables at various nodes. The manner in which the discretization equations are obtained determines the technique. For example in the finite difference technique the discretization equations are obtained by differentiation. In the finite element technique the discretization equations are obtained by integration. In the finite volume technique the discretization equations are obtained by a combination of differentiation and integration.

Finite difference and finite element are the two methodologies employed most commonly in Computational Fluid Dynamics (CFD). With regard to the task of computing flows in complex geometries, the finite element method appears to be the most natural tool, because of its better geometric flexibility. However, the finite difference method takes advantage of coordinate transformations and grid generation techniques to exploit its simplicity and efficiency as mentioned by Napolitano and Orlandi (1985).

The finite volume method was originally developed as a special case of finite difference formulation. The numerical algorithm consists of the basic procedures available in any numerical solution technique. It integrates the governing equations of fluid flow over all the finite control volumes of the solution domain. The terms in the integrated equation, representing the flow processes such as convection, diffusion, and

source, need to be discretized which involves the substitution of a variety of finite difference approximations. This converts the integral equations into a system of algebraic equations which need to be solved by an iterative method. Therefore, the work in this thesis will adopt this most well established and thoroughly validated general purpose CFD technique. It is central to several commercially available CFD codes such as PHOENICS, FLUENT, FLOW3D, and STAR-CD.

Finite volume techniques are increasingly being used for computing incompressible flow in arbitrary geometries because of the recent developments in grid generation methods. Some of the earlier finite volume approaches were developed for orthogonal coordinate systems due to fewer terms resulting from a coordinate transformation. Sharatchandara (1995) mentioned that this approach is limited due to the difficulty of maintaining orthogonality throughout the entire domain and the undesirable grid clustering that results from the forced orthogonality constraints. The generalized non-orthogonal coordinate system approach appears to be the most appropriate choice for the majority of the recent finite volume approaches. This is not only on account of its generality, but also due to the fact that it is possible to orient the dependant variable along the grid lines conforming to the shape of the domain and therefore usually along principal streamlines, which will minimize the chance of false diffusion (Patankar, 1980).

The choice of a proper grid arrangement is closely related to that of the dependent variables in the momentum equations. The configuration should be such that it does not admit spurious solutions such as a checkerboard pressure field. The staggered

grid arrangement wherein scalar variables are stored at cell nodal centers and velocity components at cell faces, has long been preferred on account of its desirable pressure-velocity coupling characteristics as described by Patankar (1980).

When Cartesian velocity components are retained as dependent variables and the coordinates are transformed, such formulation of the governing equations is considered partial transformation. This has been extensively used in the past, primarily on account of its simplicity. The Cartesian velocity components have been widely used as the dependent variables in non-orthogonal coordinate systems (Maliska and Raithby, 1984, and Shyy et al., 1985). The curvilinear components of velocity change their directions and tend to "follow" the grid lines. This feature makes them more attractive for highly non-orthogonal grids and geometries with strong curvature. However, due to the changes in their direction the governing equations are very complicated and involve curvature source terms that account for the fact that momentum is conserved along a straight line. These source terms can also be derived by using tensor analysis.

1.2 General Curvilinear Coordinate System

1.2.1 Body-Fitted Coordinate

The Cartesian coordinate system is the most common coordinate system used to describe the location of a point in space. It takes advantage of the three base vectors that characterize the system of an orthonormal system. Computational Fluid Dynamics methods, based on Cartesian or cylindrical coordinate systems, have certain limitations in irregular geometries. When the boundaries of the domain of the physical problem are

not aligned along the Cartesian base vector directions, the use of the Cartesian coordinate system is inconvenient and often impractical. However, it can only be approximated in Cartesian coordinate systems by treating surfaces in a stepwise manner as illustrated in Fig. 1.1a.

The cylindrical surface has to be replaced by a step approximation to calculate the flow over the circular cylinder. One may consider that the more stair-steps are used a closer approximation is obtained to the exact boundary shape. This procedure has considerable disadvantages since the approximate boundary description is tedious to set up and introduces errors, especially if the wall shear stresses need to be calculated to good accuracy as mentioned by Versteeg and Malalasekera (1995). This is accompanied by an increase in the computer storage resources due to the higher number of computational nodes required in the analysis. The introduction of a fine Cartesian grid in a specific area of particular interest could result in unnecessary refinement in the other region of minimal interest.

The above referred problems can be avoided by using a coordinate system where principal coordinate directions are aligned along the domain boundaries of any physical problem. Such a system is referred to as a body-fitted coordinate system and is specific to the particular domain of interest. Methods based on the body-fitted grid or non-orthogonal grid system have been developed and used increasingly in the present CFD procedure, for details one can refer to Rhie and Chow, 1983; Peric, 1985; Demirdzic et al, 1987; Shyy et al, 1988; and Karki and Patankar, 1988.

The advantages of using a body-fitted coordinate system are illustrated in Fig 1.1b. The flexibility offered by body-fitted grid techniques is useful in the modeling of practical problems involving irregular geometries. All geometrical details can be accurately incorporated and the grid properties can be controlled to capture useful features in the region of interest. However, the governing equations using the body-fitted coordinate system are much more complex than their Cartesian counterpart. The major differences between the two formulations are based on the grid arrangement and the choice of dependant variables in the momentum equations. Detailed discussion of the available methods of formulating the governing equations can be found in Demirdzic (1982) and Shyy and Vu (1991).

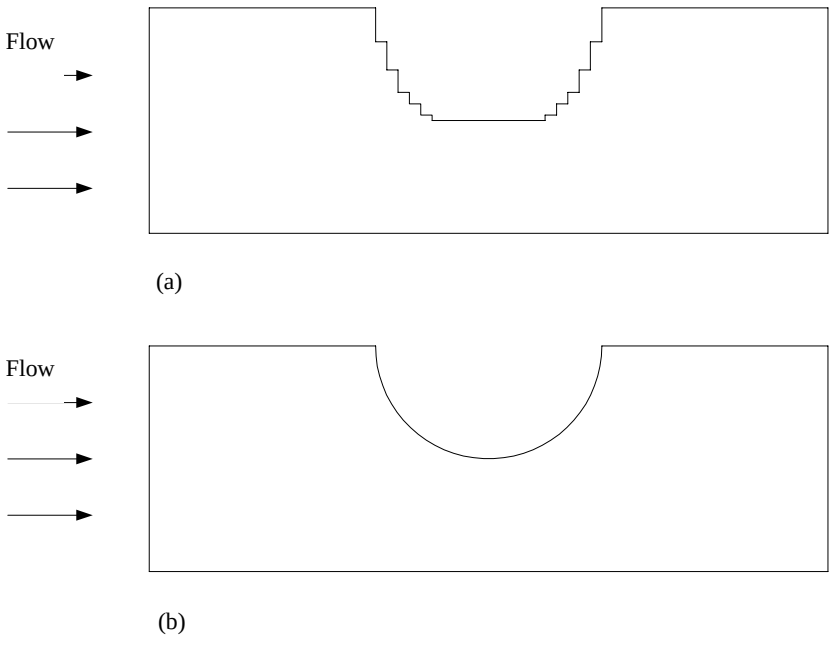

Fig. 1.1 Grid arrangement of flow over a circular cylinder in: (a) stepwise approximation and (b) real domain.

1.2.2 Generalized Coordinate Transformation

The well-known Cartesian coordinate system is characterized by the three base vectors, which have preferable properties of orthogonality and spatial invariance. However, in the General Curvilinear Coordinate System, each coordinate needs to be described by two sets of base vectors. Sharatchandara (1995) explained that one of the base vectors will be parallel to the coordinate lines and the second one will be normal to the coordinate surfaces, in order to characterize the system. Fig. 1.2 shows the covariant (tangential to a line along which the coordinate ξ varies) base vector in the ξ direction and the contravariant (normal to the surface $S(\eta,\zeta)$ on which ξ is constant) base vector associated with the ξ coordinate direction. Covariant and contravariant base vectors may be similarly described for the other two coordinate directions (η,ζ).

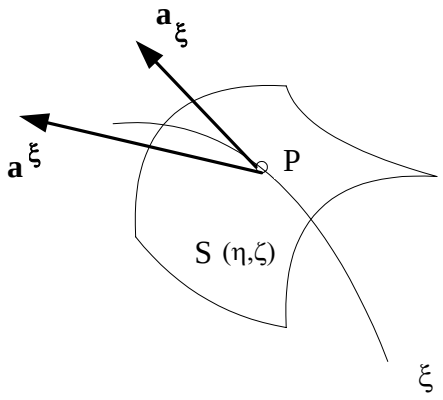

Fig. 1.2 Covariant and contravariant base vectors.

The coordinate system will be considered as non-orthogonal, if the surfaces of the constant ξ are not normal to the lines along which the coordinate ξ varies, even if the

coordinate system is orthogonal at some points of the domain. It has to be noted that if the surface S(η,ζ) is perpendicular to the line ξ at point P, then there will be no distinction between the covariant and contravariant base vectors as can be seen in Fig. 1.2.

When the covariant and contravariant base vectors, at different locations, are oriented in different directions, the body-fitted coordinate system is not spatially invariant. It is more preferable to have a spatially invariant basis for the representation of the base vectors at all points of the domain. The Cartesian coordinate basis, the only such basis in three-dimensional space, is generally used in the representation of the base vectors in a general curvilinear non-orthogonal coordinate system.

Fig. 1.3 shows a non-uniform non-orthogonal physical plane x-y which is to be transformed to a uniform orthogonal computational plane ξ-η. Where ξ and η are known to be as: $\xi = \xi(x, y)$ and $\eta = \eta(x, y)$. It is highly recommended that this transformation be one-to-one and invertible. It is this kind of mapping transformation from the x-y plane to the ξ-η plane where every single-point in the physical domain has its own corresponding point in the computational domain. By following this procedure, we will end up with a number of rows and columns in the computational domain that correspond to rows and columns in the physical domain as mentioned by Sharatchandara (1995).

1.3 Grid Generation Methods

The field of grid generation is very wide and the number of studies on this subject are numerous. Thompson (1982) and Thompson et al. (1985) present a

comprehensive introduction to the methods of grid generation. Grid generation in one dimension is straightforward. The two boundaries (i.e., end points) of the physical space must be defined, and the problem reduces to determining the grid spacing in one dimension. One-dimensional grid generation is important in itself for the use of one-dimensional problems and in two-dimensional grid generation, where the boundaries of two-dimensional space consist of several one-dimensional spaces, and so forth. Grid generation within two- and three-dimensional spaces is considerably more complicated than one-dimensional grid generation (Hoffman, 1992).

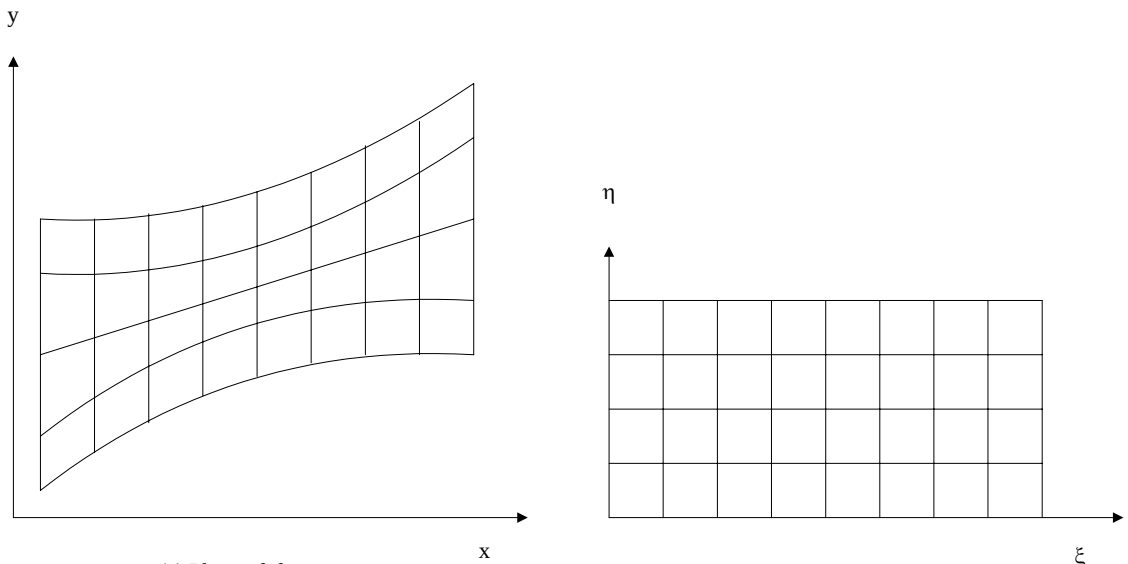

Fig. 1.3 Transformation from (a) physical to (b) computational space.

Available grid generation techniques can be generally classified into three general categories: (i) Conformal mapping, (ii) Algebraic methods, and (iii) Differential

equation methods. Conformal mapping is based on a complex variable theory, which has limitations to two-dimensional problems. Consequently, this method is not as general as the other methods and will not be considered further. Algebraic methods and differential equation methods can be applied to both two- and three-dimensional spaces. Consequently, they are the methods of choice. A brief overview of both of these will be mentioned next.

1.3.1 Algebraic Methods

The algebraic grid generation technique is based on the specification of algebraic equations for the Cartesian coordinates x, y, and z in terms of general curvilinear coordinates ξ, η, and ζ. Karki (1986) summarized the algebraic features of such equations as stretching transformation, shearing transformation, and blending function or isoparametric transformation. For example, the shearing transformation is a linear transformation used to non-dimensionalize the distance between two physical boundaries. The physical domain illustrated in Fig. 1.4a can be discretized using the algebraic sheared transformation. The x-coordinate can be transformed by any one-dimensional transformation, if needed. It is simply discretized into equally spaced points. The y-coordinate is then discretized into equally spaced points at each x location by the normalizing transformation technique as:

$$y = \left(\frac{\eta - 1}{\eta_{\max} - 1} \right) Y(x) \qquad (1 \le \eta \le \eta_{\max}) \qquad (1.1)$$

where Y(x) is the upper boundary. The results of the complete transformation are illustrated in Fig. 1.4b. The reader is referred to Hoffman (1992) for further information.

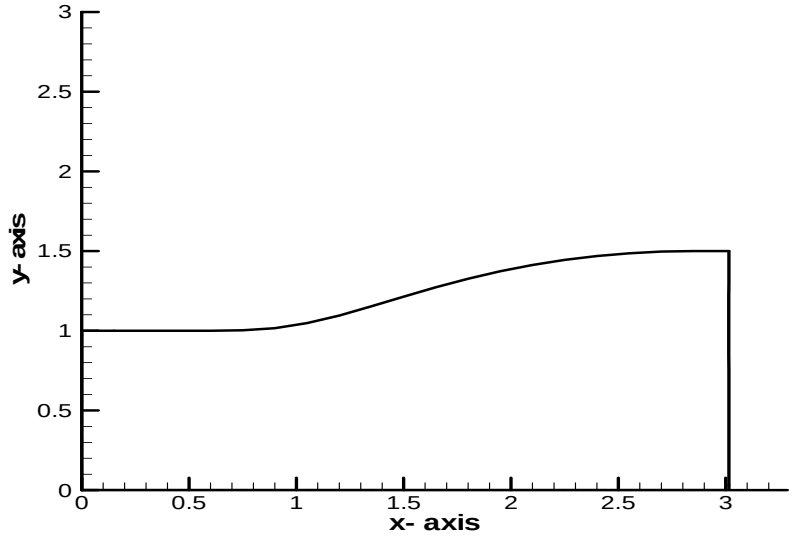

(a)

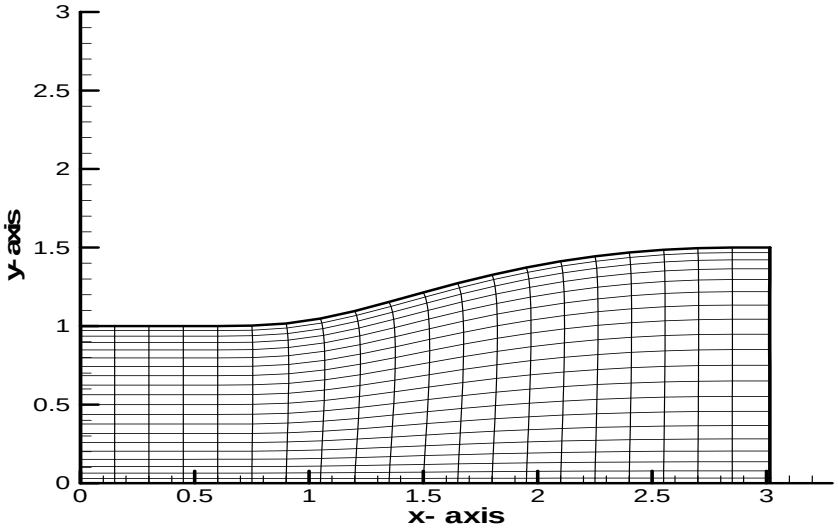

(b)

Fig. 1.4 Grid generation using normalizing transformation technique (a) physical domain and (b) grid point distribution.

Transfinite interpolation is considered to be a highly advanced method of algebraic grid generation technique as described by Gordon and Hall (1973). The location of the grid points inside the domain is determined by a series of uniform variation interpolations between the boundaries. The degree of freedom of the blending function can be either linear or higher order which controls the grid spacing and angles at the intersection. The choice of higher order is preferable because it gives more flexibility in controlling the gridline spacings and the angles at which grid lines meet the boundaries. However, this may create an overlapping and crossover of the grid lines. For further information the reader may refer to Thompson et al. (1985).

1.3.2 Differential Equation Methods

Algebraic grid generation techniques mentioned above have some disadvantages associated with the grid. Discontinuities at the intersection of cell faces, crossover of the gridlines, and undesirable gridline spacings are some of them. A more consistent method to overcome these problems is the use of a system of partial differential equations to obtain a higher degree of grid smoothness. Grid generation using partial differential equations involves the following steps: (i) determining the grid point distributions on the boundaries of the physical domain, and (ii) specifying the interior grid points by using partial differential equations that satisfies the grid point distributions on the boundaries.

Any of the three classical types of partial differential equations (i.e., elliptic, parabolic, or hyperbolic) may be used as the governing grid generation equation. The

elliptic grid generation technique discussed by Thompson et al. (1985) is considered as the well-known method in this field. The most common elliptic partial differential equation is the Poisson equation (in two-dimensional domain):

$$\nabla^2 \xi = \xi_{xx} + \xi_{yy} = P(\xi, \eta) \tag{1.2}$$

$$\nabla^2 \eta = \eta_{xx} + \eta_{yy} = Q(\xi, \eta) \tag{1.3}$$

using the inverse transformation and some mathematical manipulations, one can derive the following elliptic partial differential equations for the Cartesian coordinates:

$$\alpha x_{\xi\xi} - 2\beta x_{\xi\eta} + \gamma x_{\eta\eta} = -Ja^2 (P x_{\xi} + Q x_{\eta}) \tag{1.4}$$

$$\alpha y_{\xi\xi} - 2\beta y_{\xi\eta} + \gamma y_{\eta\eta} = -Ja^2 (P y_{\xi} + Q y_{\eta}) \tag{1.5}$$

where

$$\alpha = x_{\eta}^2 + y_{\eta}^2 \tag{1.6}$$

$$\beta = x_{\xi} x_{\eta} + y_{\xi} y_{\eta} \tag{1.7}$$

$$\gamma = x_{\xi}^2 + y_{\xi}^2 \tag{1.8}$$

and *Ja* is the Jacobian of the coordinate transformation defined as:

$$Ja = x_{\xi} y_{\eta} - x_{\eta} y_{\xi} \tag{1.9}$$

These sets of equations need to be solved numerically, for x and y with respect to ξ and η, with the known prior boundary condition specifications. The parameters or control functions that can control the coordinate line spacing are P and Q.

The three-dimensional grid generation method is a combination of a series of two-dimensional grid slices, as referenced by many researchers. For both internal and

external flows, the elliptic grid generation method works fine. However, the hyperbolic grid generation method is preferred for external flow since the hyperbolic equations can be solved by non-iterative marching techniques as proposed by Steger and Sorenson (1980).

1.4 Numerical Simulation Process and Accuracy

The starting point of any numerical simulation process is the physical system which should be described. Fig. 1.5 shows schematically the whole procedure that will be performed in a numerical simulation. First, a mathematical formulation for the behavior of the physical system has to be described. This step will yield the first of the three types of systematic errors involved in the simulation procedure as mentioned by Breuer (1998). The *formulation error* describes the difference between the behavior of the physical system and the exact solution of the mathematical formulation.

After the mathematical formulation, the basic equations have to be discretized because often no analytical solution exists for a non-linear system of equations. This introduces the second type of error, called *discretization error*, defined as the difference between the exact solution of the mathematical formulation and the exact solution of the discretized equations. In Computational Fluid Dynamics, the size of this error can be minimized by choosing the proper discertization method and a sufficiently fine grid. Finally the third type of error, called *convergence error*, is due to the difference between the iterative and the exact solution of the discertized equations. It depends on the solver and the convergence criteria chosen.

These types of errors should be clearly distinguished even though they are in general completely mixed up in the numerical solution of a physical problem. However, one should be aware of these errors that strongly affect the quality of any CFD simulation.

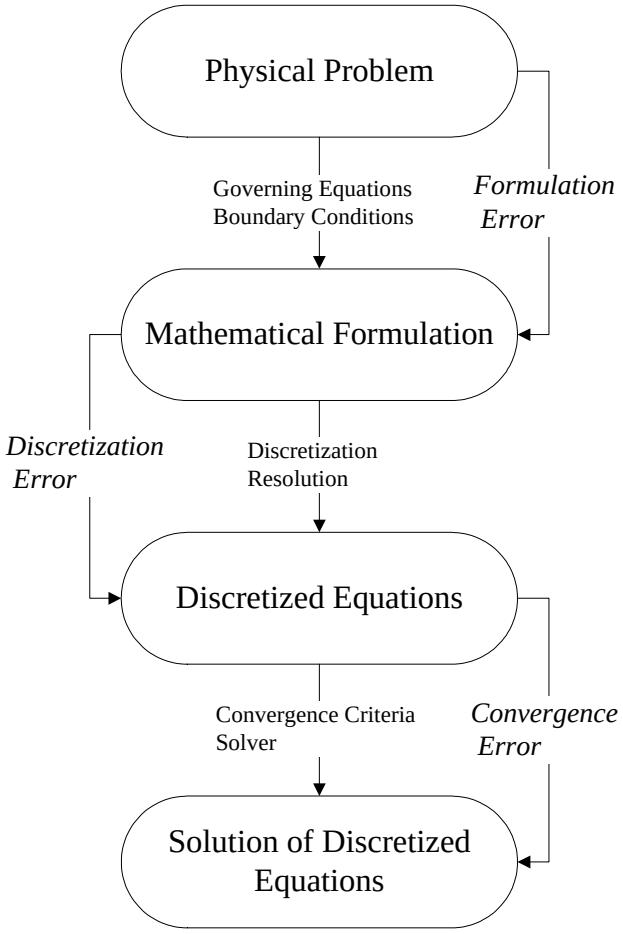

Fig. 1.5 Different types of errors involved in a numerical simulation.

1.5 Outline of the Dissertation

In this chapter a brief introduction is presented to the huge field of fluid flow computations in complex geometries. The essential concept involved in the various

numerical methodologies and grid generation concerning body-fitted coordinates has been summarized. Chapter II presents the literature relevant to the computation of flow in irregular geometries. In addition, the objective of the present dissertation will be clearly stated and explained.

In Chapter III, various methodologies of dependent variable selections have been outlined with a brief section about grid configurations. The theory of coordinate transformation is described in Chapter IV followed by a detailed description of the mathematical formulation used in this study.

In Chapter V, demonstrations of the accuracy of and reliability of the calculations are presented by means of computing some standard benchmark test cases and comparing the results to those of previous investigations as well as established solutions. Chapter VI presents the test problem studied in this work as well as the effect of changing parameters on fluid flow and heat transfer characteristics. Chapter VII will present the conclusions of this study and outlines some recommendations for further studies.

CHAPTER II

PRIOR WORK AND PRESENT OBJECTIVES

2.1 Grid Arrangement and Velocity Components

2.1.1 Orthogonal Coordinate

Orthogonal grid formulation is the most employed scheme for computing fluid flow in complex geometrical domains. This type of grid is popular because either the domain of interest can be mapped onto orthogonal coordinates or nearly orthogonal grids can be generated by using an advanced grid generation technique such as elliptic differential equations. The merit of such a formulation is the simplicity of the governing equations of fluid flow when compared to its non-orthogonal grid counterparts. Additional terms arise because of the non-orthogonality of the coordinate system which would vanish if an orthogonal system were to be employed.

The derivation of the orthogonal formulation is quite similar to the standard Cartesian coordinates with using additional geometric quantities and source terms. An implicit finite difference method using orthogonal coordinates was presented by Hung and Brown (1977). They applied it to two-dimensional corrugated channel flow using a non-conservative form of momentum equations and pressure was solved by the differential Poisson equation. Raithby et al. (1986) have developed a new orthogonal coordinate formulation technique in which it becomes more flexible to cover a broad range of geometrical applications, but it requires more computer storage. In this

technique, the discretization equations retained the stress tensor instead of the formal way of replacing them in terms of strain rate tensor. Another robust orthogonal coordinate formulation is the approach developed by Kadja (1987) to compute the flow in constricted tube banks.

The disadvantage of using orthogonal grid generation is the limitation of its applicability. In two-dimensional, not to mention three-dimensional, the controlling of the gridline spacings is hard even if special techniques were to be used. The generality of the non-orthogonal coordinate formulation makes it more favorable. Hence, a non-orthogonal grid is adopted in this study.

2.1.2 Non-Orthogonal Coordinates with Staggered Grid Arrangement

Non-orthogonal coordinate formulation techniques are classified based into two categories: (i) grid arrangement and (ii) the velocity components used in the momentum equations as the dependent variables. Early methods for non-orthogonal coordinate formulation involve Cartesian velocity components, as the dependent variables in the momentum equations, in a staggered grid arrangement in which they were stored at each control-volume face.

Shyy et al. (1985) employed elliptic equations for the grid generation to compare three different differencing schemes. In their method, one Cartesian velocity component was stored at each cell face in a two-dimensional staggered grid arrangement. The terms arising due to the non-orthogonality of the coordinates were neglected in the solution of the pressure correction equation. This approach is limited to the domains that have aligned boundaries to the Cartesian plane coordinates.

The limitation mentioned above can be removed by storing all Cartesian velocities at all cell faces. This method has been developed by Maliska and Raithby (1984) to compute flow in a square cavity with a moving wall. This arrangement is not free of difficulties. The resulting pressure equation in this case is not diagonally dominant and may prevent the use of an iterative solver for highly non-orthogonal coordinates. Shyy and Vu (1991) have shown that the use of Cartesian velocity components on staggered grids would give, in general, an acceptable solution. However, they have agreed on certain conditions that if such an approach were to be used to analyze flow in a 90^{O} pipe bend, false oscillations could occur.

2.1.3 Non-Orthogonal Coordinate with Non-Staggered Grid Arrangement

The simplicity of using the non-orthogonal grid formulation led to significant developments in this approach. The approach proposed by Hsu (1981) modified special interpolation procedures to calculate the cell face velocities instead of using the straightforward central differencing. This approach may be considered as being the first attempt to eliminate the false oscillations linked with the use of non-orthogonal grid formulation. However, the use of Cartesian velocity components may result in the prevention of diagonal dominance.

Rhie and Chow (1983) presented a novel way of treating the convective terms in the momentum equations. They used the pressure difference between adjacent nodes instead of alternate nodes to calculate the cell face velocities. This is equivalent to the linear interpolation of the velocity components. The non-orthogonal terms in the

pressure equation were ignored in the calculation, which may be essential for geometries of high curvatures. Thus, the scheme may have limited applicability.

2.1.4 Curvilinear Velocity Components

The drawbacks related to the approaches presented above guided the researchers to test the implementation of the curvilinear velocity components on different grid configurations. The covariant (tangential component) or contravariant (normal component) velocity components are the viable option because they change their direction in the computational domain as if they lean to follow the grid lines. With all these positive aspects of using covariant or contravariant velocity components, the complications of such formulation would make its use less popular or a bit limited.

Demirdzic et al. (1980) presented a finite volume methodology involving contravariant velocity components which solve the semi-strong form of the Navier-Stokes equations. They used a staggered grid arrangement and the negative coefficients in the pressure equation were neglected to ensure diagonal dominance. Another finite-difference technique was proposed by Faghri et al. (1984) in which one curvilinear coordinate was used for problems where one boundary of the domain was not aligned along either of the Cartesian coordinates. Their method was based on an algebraic transformation using covariant velocities as the dependent variables, where such a method is limited in applicability.

Yang et al. (1988) have derived a formulation involving non-orthogonal grid with spatially invariant metrics for buoyant flows in parallelopiped enclosures. Their approach is based on an expansion of the orthogonal methodology of Raithby et al.

(1986) for conditions concerning grid skewness. A study conducted by the same team later by Yang et al. (1990) has removed the restriction of spatial invariance, but the weak formulation was retained. They have studied natural convection in a horizontal cylinder with annular baffles.

Karki (1986) derived the discretization equations in terms of covariant velocity components directly from the corresponding discretization equations in terms of the Cartesian velocity components. The SIMPLER algorithm was used in this formulation to couple velocity and pressure fields. The formulation was accomplished by projecting the Cartesian velocity components, in a strong conservation form, in the direction of the curvilinear base vectors. The benefit of the above method is that no orientations need to be made to the differential form of the scalar transport equation in terms of curvilinear velocities. It has to be noted, that the above mentioned projections do not produce a formulation in terms of velocity components and that transformation or interpolations will still be required to evaluate the cell face contravariant mass flux terms.

The study of Sharatchandra and Rhode (1994a & b) was based on maintaining the conservation form of the Navier-Stokes equation, by means of a straight discretization of the vector momentum equation. The necessity of a transformation to obtain the interface mass flux terms was eliminated due to the use of contravariant velocity components as the dependent variables. It is well shown as to how the choice of base vector directions, in which the discretized vector equation may be projected, affects the stability of the computational scheme. They have demonstrated the efficiency of the

formulation by means of comparison with preceding computations for some standard benchmark test problems.

2.2 Geometry and Flow Conditions

Tubular heat exchangers are found in many energy conversion applications ranging from nuclear reactors to refinery condensers. The heat transfer coefficient of the tube and the pressure drop of the fluid flowing externally are the most important design variables for the tubular heat exchangers. Based on studies, reported in literature, the effects of tube shape and arrangement have indicated that they could have a positive influence in the heat exchanger Ota et al. (1984); Ota et al. (1986); and Wung et al. (1986).

It has been of interest to many researchers to investigate fluid flow and heat transfer over objects of many different shapes. Flat tubes have not been investigated to the same extent, although they play an important role in many engineering applications such as modern heat exchangers and automotive radiators. Flat tube designs have recently been introduced for use in automotive air conditioning evaporators and condensers. Developments in automotive brazed aluminum manufacturing technology have made the construction cost of the flat tube heat exchangers more favorable (Webb, 1993).

A brief preview of different studies involving flow over a variety of shapes with various types of flow conditions is worth mentioning at this time for the reader. The effect of flow past bluff bodies, especially cylinders, has been a major attraction for fluid mechanics investigations for a long time. Most of these studies were concerned with the

flow over a circular cylinder. Williamson (1996) and Zdrakovich (1997) wrote comprehensive reviews on this topic.

Chang et al. (1989) has developed a numerical scheme to predict the heat transfer and pressure drop coefficient in cross flow through rigid tube bundles. The scheme uses the Galerkin finite element technique. The conservation equations for laminar steady-state flow are cast in stream-function and vorticity form. A Picard iteration method was used for the solution of the resulting system of non-linear algebraic equations. Results for heat transfer and pressure drop coefficients are obtained for tube arrays of pitch ratios of 1.5 and 2. Very good agreement, of the predicted numerical results and experimental data obtained, was observed up to Reynolds number (Re = 1000).

Chen and Weng (1990) numerically studied flow and thermal fields in forced convection over a heated cylinder for both incompressible and compressible flow. The governing system of equations included full two-dimensional Navier-Stokes momentum, energy, and continuity equations in body-fitted coordinates. The effect of the Reynolds number was investigated. In their study, a grid generation technique proposed by Thomas and Middecoff (1980) was adopted to handle an arbitrary shaped domain by which a body-fitted coordinate system was generated and the irregular physical domain was transformed into a square meshed computational domain. The finite difference approximation for the transformed conservation equation was obtained by the integration over the control volume and subsequently discretized it in the transformed coordinate system. The upwind scheme was adopted for the convection term and the central difference scheme for the diffusion term. The velocity and pressure fields were linked by

the Semi-Implicit Method for Pressure Linked Equation (SIMPLE) algorithm (Patankar, 1980).

Kundu et al. (1991a & b) numerically studied heat transfer and fluid flow over a row of in-line cylinders placed between two parallel plates. Incompressible, two-dimensional, and laminar flow was considered. The spacing between cylinders causes three different separation patterns. When the spacing is small, the separated flow between cylinders is stable. As the spacing increases, flow in the separated zone becomes periodic. At higher values of spacing, the separated flow is local and does not extend to the next cylinder. The cylinder and plate temperatures were assumed to be constant but not necessarily the same. The spacing between cylinders alters the flow in the separated zone and subsequently affects the heat transfer. The heat transfer data for different aspect ratios and Reynolds numbers are reduced to form a single formula for ease of interpolation. In general, the pressure drop and heat transfer were spatially periodic, indicating periodically fully developed characteristics.

Numerical solutions were obtained, by Grannis and Sparrow (1991), for the fluid flow in a heat exchanger consisting of an array of diamond shaped pin-fins. The model that underlines the solutions was based on the concept of the periodically fully developed regime, whereby the velocity field repeats itself from row to row and the pressure drop per module remains constant. Implementation of the model was accomplished via the finite element method, whereby the solution domain was discretized by subdividing it into an assemblage of two-dimensional, nine-noded quadrilateral elements. As a prelude to the final numerical solution, a systematic study

was performed to establish the number of elements needed for the attainment of accurate results. For validation purposes, solutions were run for arrays of circular cylindrical pin-fins (i.e., tube bank) and specific arrays of diamond shaped pin-fins to enable comparison of pressure drop prediction with available experimental data. The final set of numerical solutions encompassed 18 different arrays. The parameters were the vertex angle of the diamond shaped fins, dimensionless transverse, and longitudinal center to center distance between the fins. The result included representative streamline maps and isobar and an in depth display of pressure drop information. The results were presented as a function of the Reynolds number.

Yu et al. (1995) applied the weighted residuals method to analyze mixed convection heat transfer in a 3x3 in-line horizontal tube bundles placed between two vertical parallel plates. The flow regimes of Reynolds numbers up to 500 and Grashof numbers up to 53,000 were investigated and the local data of the different geometries were reported. Data for both pure forced and mixed convection were presented for the purpose of comparison. It was shown that the thermal performance for the front sector of downstream cylinders was strongly affected by the presence of the upstream cylinders, while the backward sector of downstream cylinders remains basically uninfluenced by the upstream cylinders. The average Nusselt number for the array increases 20-30% when streamwise spacing was increased by 50%.

Flow and conjugate heat transfer in a high-performance finned oval tube heat exchanger element have been calculated for a thermally and hydrodynamically developing three-dimensional laminar flow by Chen et al. (1998a & b). The influence of

Reynolds numbers in the range 100-500 was studied. Computations were performed with a finite volume method based on the SIMLPEC algorithm for pressure correction. Flow patterns and pressure distributions were presented. A helical vortex in the tube wake was observed. The shape of the separation zone in the tube wake shows a paraboloid. Also, heat transfer characteristics were presented, including heat flux in the tube, fin temperatures, fin Nusselt numbers, heat flux distributions, fin efficiency, Colburn *J* factor, and apparent friction factors (f_{app}). For the investigated configuration, the ratio of heat transfer on the tube to that on the fin remain under 10%. The fin temperature and fin efficiency were found to depend weakly on fin parameter.

Breuer et al. (2000) investigated in detail the confined flow around a cylinder of square cross-section mounted inside a plane channel (blockage ratio B = 1/8) by two entirely different numerical techniques, namely a Lattice-Boltzmann Automata (LBA) and a finite volume method (FVM). In order to restrict the approach to 2D computations, the largest Reynolds number chosen was Re = 300 based on the maximum inflow velocity and chord length of the square cylinder. The LBA was builtup on the (D2Q9) model and the single relaxation time method called the Lattice-BGK method. The finite-volume code was based on an incompressible Navier-Stokes solver for arbitrary non-orthogonal, body-fitted grids. Both numerical methods are of second-order accuracy in space and time. Accurate computations were carried out on grids with different resolutions. The results of both methods were evaluated and compared in detail. Both velocity profiles and integral parameters such as drag coefficient, re-circulation length,

and Strouhal number were investigated. Excellent agreement between the LBA and FVM computation was found.

2.3 Present Objectives and Aim of this Work

The main objective of this work is to develop a computer code to predict the heat transfer and pressure drop characteristics of flows around or through rigid complex geometry, namely domains whose boundaries do not coincide with coordinate lines of a Cartesian or any simple coordinate system. The present study considers steady laminar two-dimensional incompressible flow past flat tube bundles found in heat exchanger applications. The effects of various independent parameters such as Reynolds number (Re), Prandtl number (Pr), length ratio (L/Da), and height ratio (H/Da) on pressure drop and heat transfer were studied.

The use of a staggered grid arrangement is preferable for solving the incompressible Navier-Stokes equations in generalized coordinates. Therefore, this kind of grid arrangement will be adopted for this study. The schemes which store one Cartesian velocity component at each face have limited applicability. The most appropriate choice for the dependent variables in the momentum equations are the covariant and contravariant physical components of velocities. Hence it will be the choice in this study.

CHAPTER III

DEPENDENT VARIABLES AND GRID CONFIGURATION

Transformation relations from the Cartesian system of physical plane to a general two-dimensional coordinate system will be shown in this chapter. In numerical solutions, the curvilinear gradients in these expressions are represented by differences along the coordinate lines. Hence, the derivatives can be expressed in terms of points along the coordinate lines without requiring any interpolation. The expressions will be obvious if one refers to the general element as shown in Fig. 3.1. Four curved lines are the boundaries of this element, each of which lies on a surface where one of the curvilinear coordinates is constant.

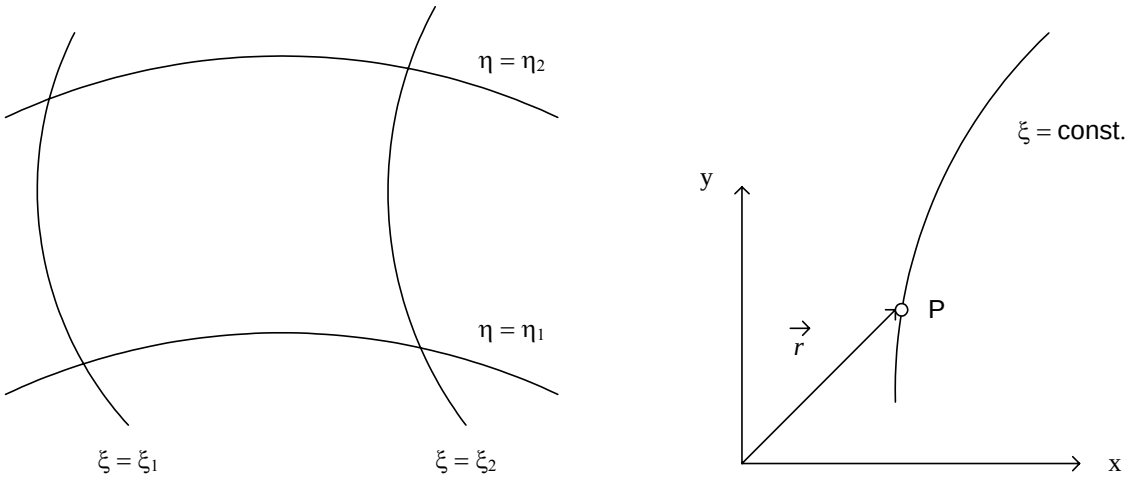

Fig. 3.1 General element with the position vector of a general point P(x,y).

The tangent (covariant) and the normal (contravariant) base vectors were described in physical terms in Section 1.2.2. It is necessary, from a computational point of view, to have a mathematical representation of the coordinate base vectors. Consideration of the curvilinear and non-orthogonal nature of the coordinate systems would make the generalized tensor notation the appropriate choice; however, for simplicity, the Cartesian vector notation will be used throughout this study. This will be shown in the next section.

3.1 Mathematical Representation of Base and Unit Vectors

3.1.1 Covariant and Contravariant Base Vector

The covariant base vector in the ξ or η coordinate direction at point P in a two-dimensional plane, as shown in Fig. 3.2, is defined as the tangent vector to the ξ or η coordinate line at P, respectively. Following the mathematical definition of the tangent vector, as the directional derivative of the position vector $\vec{r}$, the covariant base vector in the ξ and η coordinate direction may be expressed as:

$$\vec{a}_{\xi} = \frac{\partial \vec{r}}{\partial \xi} = \frac{\partial x}{\partial \xi}\vec{e}_x + \frac{\partial y}{\partial \xi}\vec{e}_y \tag{3.1}$$

$$\vec{a}_{\eta} = \frac{\partial \vec{r}}{\partial \eta} = \frac{\partial x}{\partial \eta}\vec{e}_x + \frac{\partial y}{\partial \eta}\vec{e}_y \tag{3.2}$$

The contravariant base vector in the ξ or η coordinate direction at point P in a two-dimensional plane, as shown in Fig. 3.2, is defined as the normal vector to the ξ or η

coordinate line at P, respectively. The normal vector can be expressed mathematically as the cross product of the directional derivative of the position vector $\vec{r}$ of the other coordinate and the base vector $\vec{e}_z$ normal to the two-dimensional plane. The contravariant base vector in the ξ and η coordinate direction (Karki, 1986) may be expressed as:

$$\vec{a}^{\xi} = \frac{1}{Ja}\left(\frac{\partial \vec{r}}{\partial \eta} \times \vec{e}_z\right) = \frac{1}{Ja}\left(\frac{\partial y}{\partial \eta}\vec{e}_x - \frac{\partial x}{\partial \eta}\vec{e}_y\right) \tag{3.3}$$

$$\vec{a}^{\eta} = \frac{1}{Ja}\left(\frac{\partial \vec{r}}{\partial \xi} \times \vec{e}_z\right) = \frac{1}{Ja}\left(\frac{\partial y}{\partial \xi}\vec{e}_x - \frac{\partial x}{\partial \xi}\vec{e}_y\right) \tag{3.4}$$

where Ja, given earlier in Equation (1.9), is the Jacobian of the transformation. It represents either the area of a two-dimensional control volume or the volume of a three-dimensional control volume. For easier reference it will be given here as:

$$Ja = \left(\frac{\partial \vec{r}}{\partial \xi} \times \frac{\partial \vec{r}}{\partial \eta}\right) \bullet \vec{e}_z = \frac{\partial x}{\partial \xi}\frac{\partial y}{\partial \eta} - \frac{\partial y}{\partial \xi}\frac{\partial x}{\partial \eta} \tag{3.5}$$

It may be observed that the covariant and the contravariant base vectors were expanded in the Cartesian basis. It is the most suitable reference basis because the Cartesian base vectors constitute a spatially invariant orthonormal set in three-dimensional space. The above expressions for covariant and contravariant base vectors are similar to those which can be written in the tensor notation.

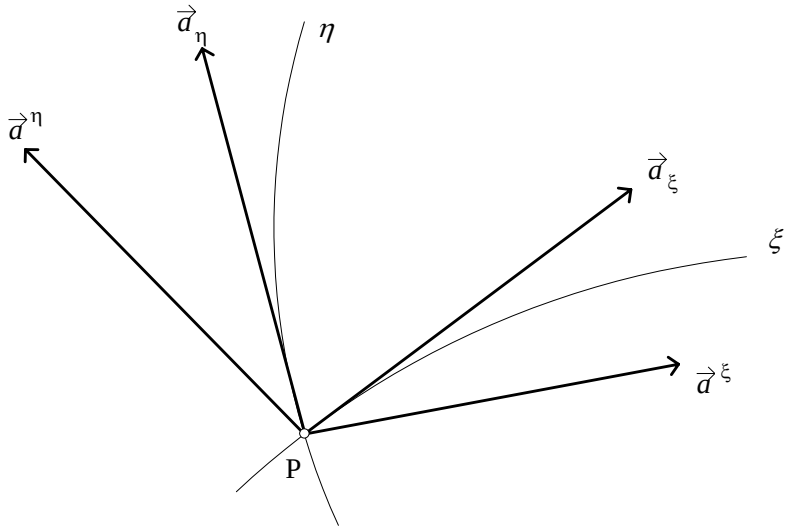

Fig. 3.2 The covariant and contravariant base vectors in a two-dimensional plane.

The planar two-dimensional coordinate system, shown in Fig. 3.2, illustrates the covariant and the contravariant base vectors on the ξ and η coordinate directions. It represents an important relationship between the covariant and the contravariant base vectors. The covariant base vector in the ξ coordinate direction, $\vec{a}_\xi$, is perpendicular (normal) to the contravariant base vector in the η coordinate direction, $\vec{a}^\eta$. However, the covariant base vector in the ξ coordinate direction, in general, is not parallel to the contravariant base vector in the ξ coordinate direction, $\vec{a}^\xi$. The orthogonality among

$\vec{a}_\xi$ and $\vec{a}^\eta$ and between $\vec{a}_\eta$ and $\vec{a}^\xi$ as well, can be clarified by taking the dot (inner) product of the two as follows:

$$\vec{a}_\xi \bullet \vec{a}^\eta = \left(\frac{\partial x}{\partial \xi}\vec{e}_x + \frac{\partial y}{\partial \xi}\vec{e}_y \right) \bullet \left(\frac{\partial y}{\partial \xi}\vec{e}_x - \frac{\partial x}{\partial \xi}\vec{e}_y \right) = 0 \tag{3.6}$$

If tensor notation is used in this formulation, it will result in the appearance of the Kronecker delta and the Identity tensor which represents an important relationship between the covariant and the contravariant base vectors. These will be very useful tools in determining expressions for the gradient and divergence operators in a curved space as well as the curvilinear components of the velocity vectors. This work is adopting the Cartesian notation. Therefore, tensor notation will not be discussed any further.

3.1.2 Covariant and Contravariant Unit Vector

It should be noted that the magnitude of the base vectors (i.e., $\vec{a}_\xi$, $\vec{a}_\eta$ etc.) are not in general equal to unity, due to the involvement with metric scale factors resulting from the partial derivatives in the mathematical representations. Therefore, it is appropriate to bring in *unit* base vectors by scaling the base vectors with the suitable metric scale factors (in the ξ or η coordinate direction). The unit covariant (tangent) base vectors in the ξ and η directions are defined as:

$$\vec{e}_{\xi} = \frac{\dfrac{\partial \vec{r}}{\partial \xi}}{\left|\dfrac{\partial \vec{r}}{\partial \xi}\right|} = \frac{\dfrac{\partial x}{\partial \xi}\vec{e}_x + \dfrac{\partial y}{\partial \xi}\vec{e}_y}{h_{\xi}} \tag{3.7}$$

$$\vec{e}_{\eta} = \frac{\dfrac{\partial \vec{r}}{\partial \eta}}{\left|\dfrac{\partial \vec{r}}{\partial \eta}\right|} = \frac{\dfrac{\partial x}{\partial \eta}\vec{e}_x + \dfrac{\partial y}{\partial \eta}\vec{e}_y}{h_{\eta}} \tag{3.8}$$

Similarly, the unit contravariant (normal) base vectors in the ξ and η directions are given by:

$$\vec{e}^{\,\xi} = \frac{\dfrac{\partial y}{\partial \eta}\vec{e}_x - \dfrac{\partial x}{\partial \eta}\vec{e}_y}{h_{\eta}} \tag{3.9}$$

$$\vec{e}^{\,\eta} = \frac{\dfrac{\partial y}{\partial \xi}\vec{e}_x - \dfrac{\partial x}{\partial \xi}\vec{e}_y}{h_{\xi}} \tag{3.10}$$

where h_{ξ} and h_{η} are the covariant and contravariant metric scale factors, respectively, defined as:

$$h_{\xi} = \left[\left(\frac{\partial x}{\partial \xi}\right)^2 + \left(\frac{\partial y}{\partial \xi}\right)^2\right]^{1/2} \tag{3.11}$$

$$h_{\eta} = \left[\left(\frac{\partial x}{\partial \eta}\right)^2 + \left(\frac{\partial y}{\partial \eta}\right)^2\right]^{1/2} \tag{3.12}$$

In most analyses, it is typical to consider the curvilinear coordinates as dimensionless quantities. Consequently the covariant and contravariant metric scale factors typically have physical units of length. In fact, h_ξ and h_η are the arc lengths along the coordinate lines. They are reciprocally related only in an orthogonal curvilinear coordinate system.

3.2 Curvilinear Velocity Components and Projections

3.2.1 Covariant and Contravariant Velocity Components

Curvilinear velocity components are linked with base vector directions. They are conversely related. The covariant velocity components are aligned along the contravariant base vector directions and the contravariant velocity components are aligned along the covariant base vector directions. Sharatchandra (1995) discussed that the velocity components, in a generalized non-orthogonal coordinate system, along the base vector directions follow the "parallelogram law" while the projections do not. The Parallelogram law is a geometric interpretation of the way in which velocity components constitute a vector. These characteristics of non-orthogonal coordinate systems will address the issues of curvilinear velocity components and projections to put them in the proper perspective.

Consider $\vec{V}$ as a velocity vector in a two-dimensional plane. Therefore, the covariant velocity components in general curvilinear coordinates can be defined as:

$$V_{\xi} = \vec{V} \bullet \vec{a}_{\xi} \tag{3.13}$$

$$V_{\eta} = \vec{V} \bullet \vec{a}_{\eta} \tag{3.14}$$

Similarly, the contravariant velocity components in the general curvilinear coordinates can be defined as:

$$V^{\xi} = \vec{V} \bullet \vec{a}^{\xi} \tag{3.15}$$

$$V^{\eta} = \vec{V} \bullet \vec{a}^{\eta} \tag{3.16}$$

It has to be noted that since the base vectors (not the unit vectors) were used in the inner (dot) product with the velocity vector, the result would be the velocity components (*not* the projections) of $\vec{V}$ along the base vectors. This may be demonstrated by consideration of the geometric understanding of the inner (dot) product which states that $\vec{V} \bullet \vec{a}$ is the product of the norms (lengths) of $\vec{V}$, $\vec{a}$, and the cosine of the included angle. While, the projection of $\vec{V}$ along $\vec{a}$ is simply the product of the norm (length) of $\vec{V}$ and the cosine of the included angle between $\vec{V}$ and $\vec{a}$.

The aforementioned velocity components are the non-physical components due to the involvement with the metric scale factor resulting from the partial derivatives in the mathematical representations as mentioned earlier. It is typically preferable to deal with physical components in the computational scheme. The physical components have

the same dimension of the velocity vector. Therefore, for the velocity vector $\vec{V}$ in a two-dimensional plane, the physical covariant velocity components in the general curvilinear coordinates can be defined as:

$$V_{(\xi)} = V_{\xi} \frac{h_{\eta}}{Ja} \tag{3.17}$$

$$V_{(\eta)} = V_{\eta} \frac{h_{\xi}}{Ja} \tag{3.18}$$

In the same way, the physical contravariant velocity components in the general curvilinear coordinates can be defined as:

$$V^{(\xi)} = V^{\xi} h_{\xi} \tag{3.19}$$

$$V^{(\eta)} = V^{\eta} h_{\eta} \tag{3.20}$$

With simple dimensional analysis, one can verify that the physical covariant and contravariant velocity components have the same dimension of the velocity vector. It has to be noted that the physical covariant velocity components are aligned along the contravariant base vector directions and vice versa. This will be clarified by referring to Fig. 3.3.

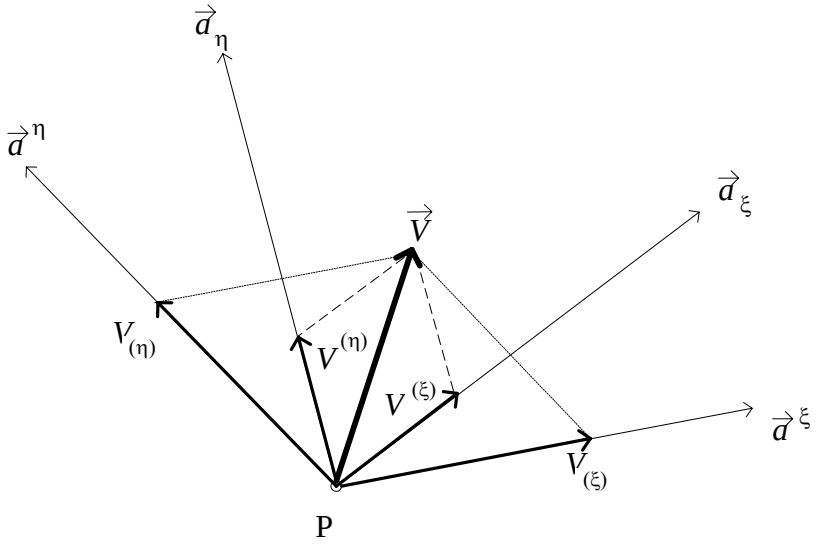

Fig. 3.3 The physical covariant and contravariant velocity components in a two-dimensional plane.

3.2.2 Covariant and Contravariant Velocity Projections

The projections of the velocity vector $\vec{V}$ at any point in the flow field, in the directions of the unit covariant and contravariant base vectors, are known as the velocity projections. The projections of $\vec{V}$ in the direction of unit vectors entails that the projections are physical quantities and have the same dimensions of the velocity vector. The physical covariant velocity projections are formally defined as:

$$u_\xi = \vec{V} \bullet \vec{e}_\xi = \left(u \frac{\partial x}{\partial \xi} + v \frac{\partial y}{\partial \xi} \right) / h_\xi \tag{3.21}$$

$$u_\eta = \vec{V} \bullet \vec{e}_\eta = \left(u \frac{\partial x}{\partial \eta} + v \frac{\partial y}{\partial \eta} \right) / h_\eta \tag{3.22}$$

Similarly, the physical contravariant velocity projections can be defined as:

$$u^{\xi} = \vec{V} \bullet \vec{e}^{\,\xi} = \left(u \frac{\partial y}{\partial \eta} - v \frac{\partial x}{\partial \eta} \right) / h_{\eta} \tag{3.23}$$

$$u^{\eta} = \vec{V} \bullet \vec{e}^{\,\eta} = \left(u \frac{\partial y}{\partial \xi} - v \frac{\partial x}{\partial \xi} \right) / h_{\xi} \tag{3.24}$$

The directions of the various velocity components and projections in a general non-orthogonal coordinate system can be shown in Fig. 3.3 and 3.4. From a geometrical point of view, both figures illustrate a fundamental difference between velocity components and velocity projections. Velocity components follow the "parallelogram law" in yielding the velocity vector $\vec{V}$ as a linear combination of the associated base vectors, while velocity projections do not. The only exception comes into view in the case of an orthogonal coordinate system, in which both the velocity vector component and projection are coincident.

3.3 Dependent Variables in Momentum Equations

The dependent variables in momentum equations are the velocity components. Attention is now focused on certain possible choices. While in principal, the possible choices are many, only certain choices are meaningful from the standpoint of interpretation. For a simple coordinate system, such as a Cartesian or cylindrical, the choice of the dependent variable is clear. However, in a non-orthogonal coordinate system, the selection of the dependent variable has no clear choice but has several

alternatives. To this end it is proper to introduce a brief discussion about the three choices used in the past: (i) velocity components in a Cartesian coordinate system, (ii) physical covariant or contravariant velocity components, or (iii) physical covariant or contravariant velocity projections.

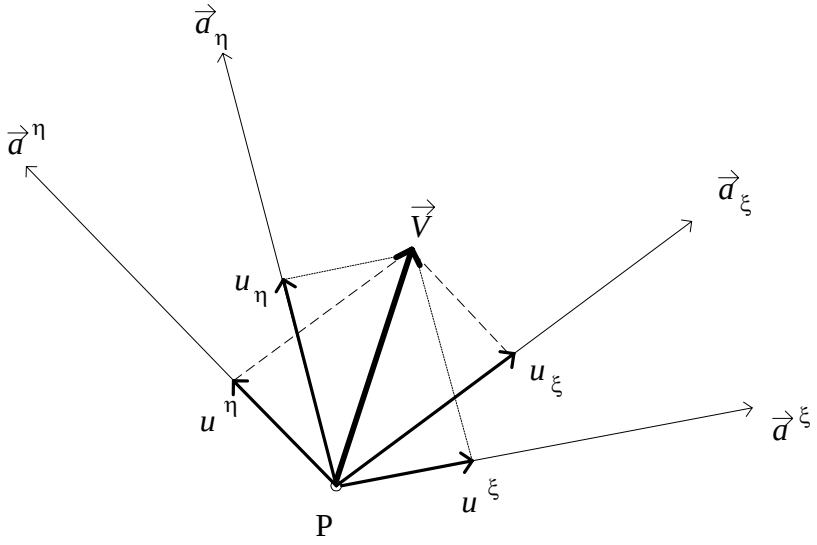

Fig. 3.4 The physical covariant and contravariant velocity projections in a two-dimensional plane.

3.3.1 Velocity Components in a Cartesian Coordinate System

The Cartesian velocity components u and v in the x- and y-directions have been widely used as the dependent variables in non-orthogonal coordinate systems as mentioned earlier in Maliska et al. (1984) and Shyy et al. (1985). The advantage of this

choice is that the formulation is relatively simple in terms of implementations and the solution of the momentum equations is very straightforward. However, for highly non-orthogonal grid, these velocity components are typically not aligned along gridlines which may introduce the problem of false diffusion. Twice the number of momentum equations has to be solved because both velocity components must be stored at each face of a control volume which results in additional computational effort.

The highly non-orthogonal grid introduces additional source terms in the pressure correction equation, as will be described in a later chapter. The explicit treatment of these source terms may cause convergence difficulty if iterative solvers are used, since the pressure correction equation is rather sensitive to small changes in the source terms. The formulation involving Cartesian velocity components has been widely popular on account of its simplicity in the implementation. Many prior investigators have shown reasonably good accuracy and convergence characteristics in the absence of high grid skewness and curvature.

3.3.2 Physical Covariant or Contravariant Velocity Components

The covariant and contravariant velocity components and projections change their directions and tend to "track" the grid lines. This characteristic makes them more attractive for highly non-orthogonal grids and geometries with strong curvature. However, due to the change in their direction, the governing equations are very complicated and involve curvature source terms that account for the non-orthogonality of the coordinate lines.

The physical contravariant velocity components in the ξ- and η-directions have been used as the dependent variables in a non-orthogonal coordinate system by Demirdzic et al. (1980). The main advantage of such formulation is the facilitation of the calculation of flow rate through a control-volume face. Furthermore, since these velocity components are aligned along the gridlines, the false diffusion will be minimized.

There are however, some drawbacks related to this formulation. The existence of the cross pressure gradient terms, due to the non-orthogonality of the coordinate system, requires the use of nine point solvers or these extra terms need to be treated explicitly. The lack of diagonal dominance in the pressure equation comes as a result of using nine point solvers. Moreover, the explicit treatment of the cross pressure gradient terms could result in a source dominant condition in strongly pressure driven flows. This is not a desirable characteristic of any computational scheme.

Another drawback of this formulation is the possibility of violating the "Scarborough Criterion" even with a slightly curved grid as illustrated in Fig. 3.5. The grid was generated by the normalization transformation method, mentioned earlier in section 1.3.1, to simulate flows in a gradual expansion channel. Here the contravariant base vector in the ξ-directions is spatially invariant while the covariant base vector changes their directions in a manner such that it tends to "follow" the grid lines.

3.3.3 Physical Covariant or Contravariant Velocity Projections

Since the solution of the pressure equation constitutes one of the most important ingredients of the overall solution strategy, the use of the physical covariant and contravariant projection is preferred in this work. Karki (1986) developed a finite

volume method for predicting viscous flows in complex geometries using covariant and contravariant projection as the dependent variable in the momentum equation. This formulation is still a well-known choice among studies employing curvilinear velocity projections as dependent variables. His formulation was based on the contravariant mass flux term at each face of a control volume. Then, each term was replaced or expressed as a linear combination involving both covariant velocity projections at that face of the control volume.

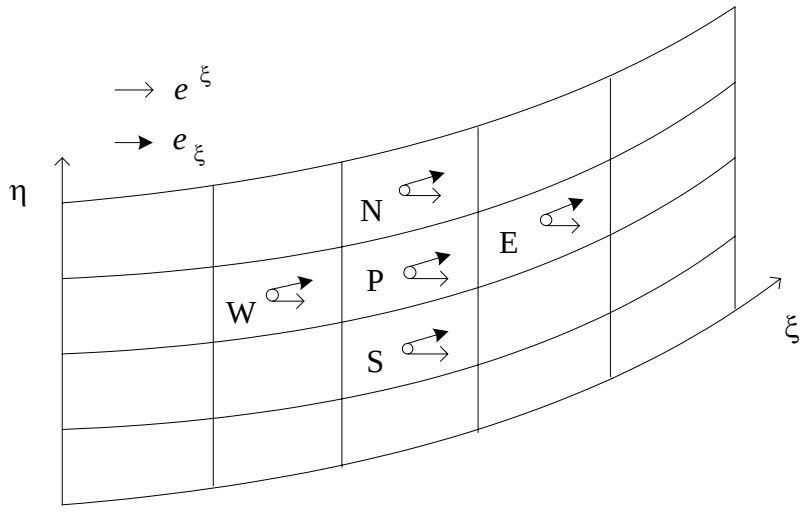

Fig. 3.5 How covariant and contravariant unit vectors change their directions.

The advantages of this formulation lie in the elimination of most of the drawbacks mentioned earlier. A less considerable and solvable drawback exists, which if ignored however, could lead to slow convergence or even divergence of the

computational scheme. The curvature source terms that arise due to the velocity components, which are used as the dependent variables, do not have a fixed direction. Therefore, these source terms could be avoided if the discretization is performed in a locally fixed coordinate system as mentioned by Karki (1986). This methodology is adopted in this work and will be explained in more detail in the next chapter.

3.4 Grid Configuration

The discrete location at which the variables are to be calculated are defined by the numerical grid which is essentially a discrete representation of the geometric domain on which the problem is to be solved. It divides the solution domain into a finite number of subdomains (e.g. control volumes). An appropriate choice of grid arrangement is as important as the choice of the dependent variables in the momentum equations. The configuration should be such that it does not let in unrealistic solutions such as a checkerboard pressure field. This section will give a detailed discussion on this subject.

3.4.1 Structured and Unstructured Grid

In case of very complex geometries, the most flexible type of grid is the unstructured grid which can fit an arbitrary solution domain boundary. Such grids could be used with any discretization scheme, but they are best adapted to the finite element and finite volume approaches. The control volume may have any shape (most often triangles or quadrilaterals in two-dimensional problems, and tetrahedral or hexahedral in three-dimensional problems). There is no restriction on the number of neighbor nodes or grids, the aspect ratio is easily controlled, and the grid may easily be locally refined.

However, grid generation and pre-processing are usually much more difficult. An example of a two-dimensional unstructured grid is shown in Fig. 3.6.

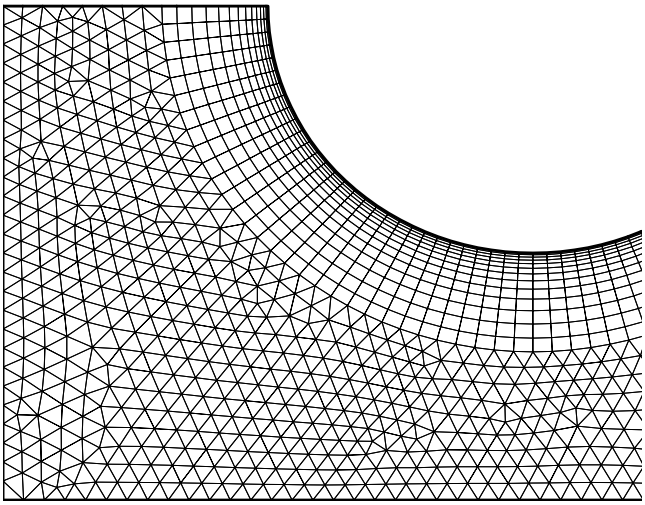

Fig. 3.6 Example of a two-dimensional unstructured grid.

Ferziger and Peric (1996) mentioned that the disadvantage of the unstructured grid is due to the irregularity of the data structure. The matrix of the algebraic equation system no longer has regular diagonal structure and the band width needs to be reduced by reordering the points. The solvers for the algebraic equations for such systems are always slower than those for regular grids. This drawback can be eliminated by using a structured grid.

Regular or structured grids consist of sets of gridlines with the characteristic that cells or elements of a single set do not cross each other and intersect each cell of the

other set only once. This allows the lines of a given set to be numbered consecutively. The position of each grid point or control volume within the domain is uniquely identified by a set of indices (e.g. I, J, and K), in which it requires two in two-dimension and three in three-dimension. This simplifies the grid structure because each grid point has four adjacent neighbors in two-dimension and six in three-dimension. The index of a point P, in the domain, differs by 1 from the indices of each neighbor point to P. Fig. 3.7 shows an example of a two-dimensional structured grid.

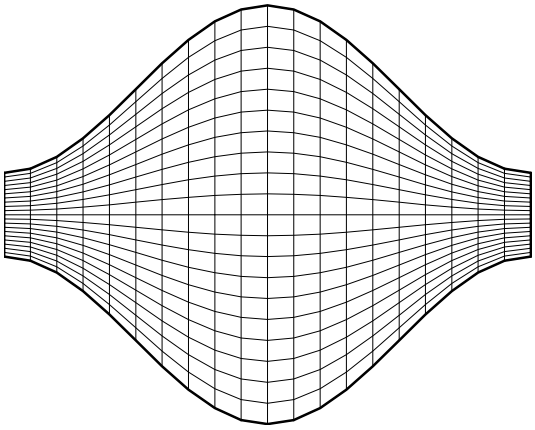

Fig. 3.7 Example of a two-dimensional structured grid.

The structured grid is not as flexible as the unstructured grid. However, the neighbor connectivity of a structured grid arranges the programming procedure and would make the matrix of the algebraic equation system have a regular structure which can be exploited in developing more efficient solvers. Such a grid facilitates the use of

line-by-line calculation procedures of discretized equations. These features make this technique more attractive than the other, and will be adopted in this work.

3.4.2 Staggered and Non-Staggered Grid

It is an issue to select the points in the domains at which the values of the unknown dependent variables are to be computed. The obvious choice is to store all the variables at the same locations and to use the same control volumes to all variables. Such a grid is called “collocated” or non-staggered grid. Since many of the terms in each of the discretized equations are essentially identical, the number of coefficients, that must be computed and stored, are reduced and the programming effort is simplified by this type of grid.

The non-staggered grid arrangement also has significant advantages in complicated solution domains, particularly when the boundaries have slope discontinuities or the boundary condition itself is discontinuous. A set of control volumes can be intended to fit the boundary including the discontinuity. Other arrangements of the variables lead to some of the variables to be located at the singularities of the grid, which may lead to singularities in the discretized equation as mentioned by Ferziger and Peric (1996). However, a serious drawback of this arrangement is that it may give rise to a checkerboard pressure pattern and a wavy pressure field may be interpreted as uniform by the momentum equations as explained by Patanker (1980).

Here comes the staggered arrangement, in which there is no need for all variables to share the same grid. It is a different arrangement that turns out to be more

advantageous. This arrangement is illustrated in Fig. 3.8. Several terms that require interpolation with the collocated grid arrangement, can be calculated without interpolation. Both the pressure and the diffusion terms are naturally approximated by central difference approximation without interpolation, since the pressure nodes are located at the center of the control volume and the velocity derivatives needed for the diffusive terms are promptly calculated at the control volume faces. Moreover, the calculation of the mass fluxes in the continuity equation on the face of the pressure control volume is straightforward. This type of grid arrangement is adopted in this work.

The best advantage of the staggered arrangement is the strong coupling between the velocities and the pressure. This will help to avoid some convergence problems and oscillation in the pressure and velocity fields. To maintain strong coupling between the momentum equations and the pressure equation, the velocity control volumes of the adjacent grid points to the boundary have to be one and a half the size of the interior control volumes (if uniform control volumes are used).

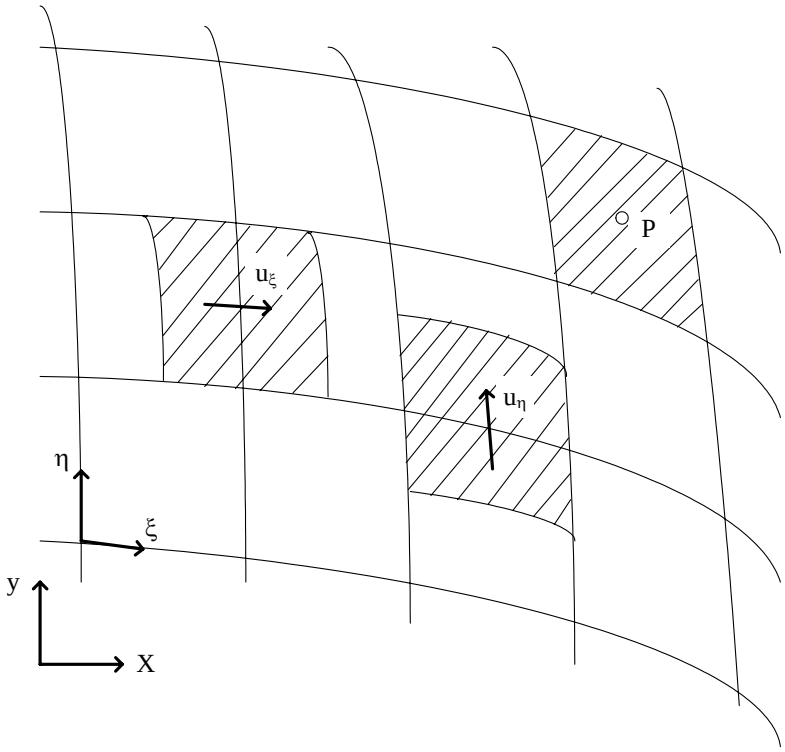

Fig. 3.8 Example of staggered grid in two-dimension.

CHAPTER IV

MATHEMATICAL FORMULATION AND NUMERICAL PROCEDURE

4.1 Governing Equations

The fundamental governing differential equations of fluid flow are the equations of conservation of mass and momentum. Moreover, the fundamental governing differential equation for heat transfer is the equation of conservation of energy. The equation of conservation of mass can be derived from a balance of the mass fluxes across a differential control element and the rate of mass accumulation within the element. The equation of conservation of momentum is derived from a force balance on the control element in conjunction with Newton's second law of motion. The conservation of energy equation is derived from an energy balance on the control element in conjunction with the first law of thermodynamics. The differential equations governing the conservation of mass, momentum, and energy can be cast into a general form as:

$$\frac{\partial(\rho\phi)}{\partial t} + \nabla \bullet \vec{J} = S \tag{4.1}$$

where

$$\vec{J} = \rho\vec{V}\phi - \Gamma\nabla\phi \tag{4.2}$$

In these equations, ϕ is a general dependent variable, ρ is the mass density, Γ is the effective diffusion coefficient, $\vec{V}$ is the velocity vector, and *S* designates the volumetric source (or sink) of ϕ. In Equation 4.2, $\vec{J}$ corresponds to the total flux of ϕ, i.e., it takes account of both the convective and diffusive fluxes. For convenience, expressions in the Cartesian vector notation for steady-state incompressible flow are given below.

Continuity: $$\nabla\bullet\vec{V} = 0 \tag{4.3}$$

Momentum: $$\rho(\vec{V}\bullet\nabla)\vec{V} = -\nabla P + \mu\nabla^2\vec{V} \tag{4.4}$$

Energy: $$\rho C_p(\vec{V}\bullet\nabla)T = k\nabla^2 T \tag{4.5}$$

Equation 4.4 above is referred to as the Navier-Stokes equation for the general constant property incompressible flow of a Newtonian fluid. The Navier-Stokes equation in the above form constitute a system of two equations (in two-dimensional flow) with two unknowns, P and $\vec{V}$. Therefore, with a given set of boundary conditions for both variables on the boundary of a certain domain, the above equations may be solved (at least in principle) for the velocity vector and pressure field inside that domain. In this chapter, the finite volume technique has been used to discretize the general conservation equations. From this point onward, only steady state, incompressible, two-dimensional

problems will be considered. The extension to unsteady or three-dimensional flow formulation is quite straightforward.

4.2 Control Volume Formulation

The first step to derive the discretized equation from the general conservation equation is to divide the computational domain into a set of non-overlapping control volumes then the conservation equations are expressed in an integral form in each of these control volumes. The advantage of this control volume approach is to preserve the conservation property, which is important for engineering applications in which the overall balance of mass, momentum, and energy are usually of major significance. The formulation presented here is identical to the formulation proposed by Karki (1986).

As mentioned earlier in Section 3.4.1, the neighbor connectivity of a structured grid arranges a programming procedure and enables the matrix of the algebraic equation system to have a regular structure which can be exploited in developing more efficient solvers. Therefore, the computational domain, in two-dimension, is divided into quadrilateral elements by using any of the grid generation techniques talked about *a priori*.

Fig. 4.1 shows a typical two-dimensional discretized computational domain. The dashed lines divide the domain into a set of quadrilateral control volumes, in which each one of them preserves the conservation property. The grid points are placed at the geometrical centers of the quadrilateral control volumes. The way of treating the placement of the grid points and the control volume faces (practice B) was suggested by Patankar (1980). The main characteristic of this practice is that the control volume faces

are placed first then the grid points are located at the geometrical centers of these control volumes. This methodology makes the treatment of discontinuities easier in the boundary conditions. Moreover, it prevents “half” control volumes at grid points adjacent to the boundary which result in simplifications when handling the boundary of the domain.

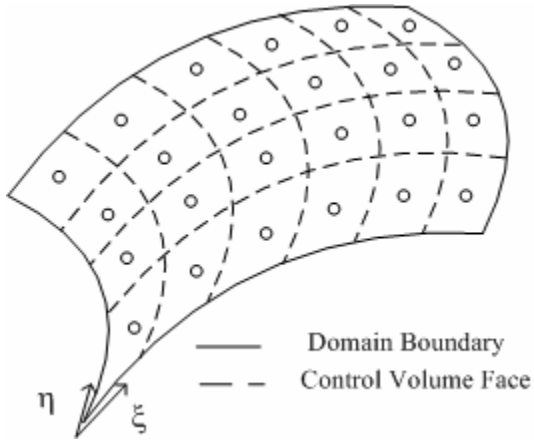

Fig. 4.1 A typical two-dimensional discretized computational domain.

Now is the time to discretize the two-dimensional, steady state form of the generalized Equation 4.1. The equation being considered is

$$\nabla \bullet \vec{J} = S \tag{4.6}$$

This equation will be discretized in terms of fluxes. Then, the general transport equation for property ϕ is derived by using a proper profile assumption. The control

volume integration, which represents the main step of the finite volume technique, yields the following form:

$$\int_A \vec{J} \bullet \vec{e}^{\,\chi} ds = \int_V S dV \tag{4.7}$$

Where V is the volume of a curvilinear element with a fixed boundary, $A's$ (the quadrilateral cell faces of P) as shown in Fig. 4.2 and $\vec{e}^{\,\chi}$ is a general unit normal vector that can either be $\vec{e}^{\,\xi}$ or $\vec{e}^{\,\eta}$, in two-dimension, depending on the cell face. It has to be noted that the capital letters E, W, N, and S denote the nodal points while the small letters e, w, n and s represent the cell faces.

The LHS of the above equation represents the total integrated fluxes through the control surfaces, which can be rewritten as:

$$\int_A \vec{J} \bullet \vec{e}^{\,\chi} ds = J_e + J_w + J_n + J_s \tag{4.8}$$

where the terms J_e, J_w, J_n, and J_s are the fluxes through each face of the elementary cell shown in Fig. 4.2. The methodology that will be followed to derive the mathematical expression for each one of these terms is similar. Therefore, one of these terms (i.e. J_e) is derived below:

$$J_e = \int_{A_I} \vec{J} \bullet \vec{e}^{\,\xi} ds \tag{4.9}$$

where $\vec{e}^{\xi}$ is the unit normal vector, mentioned earlier in Section 3.1.2, to A_I surface.

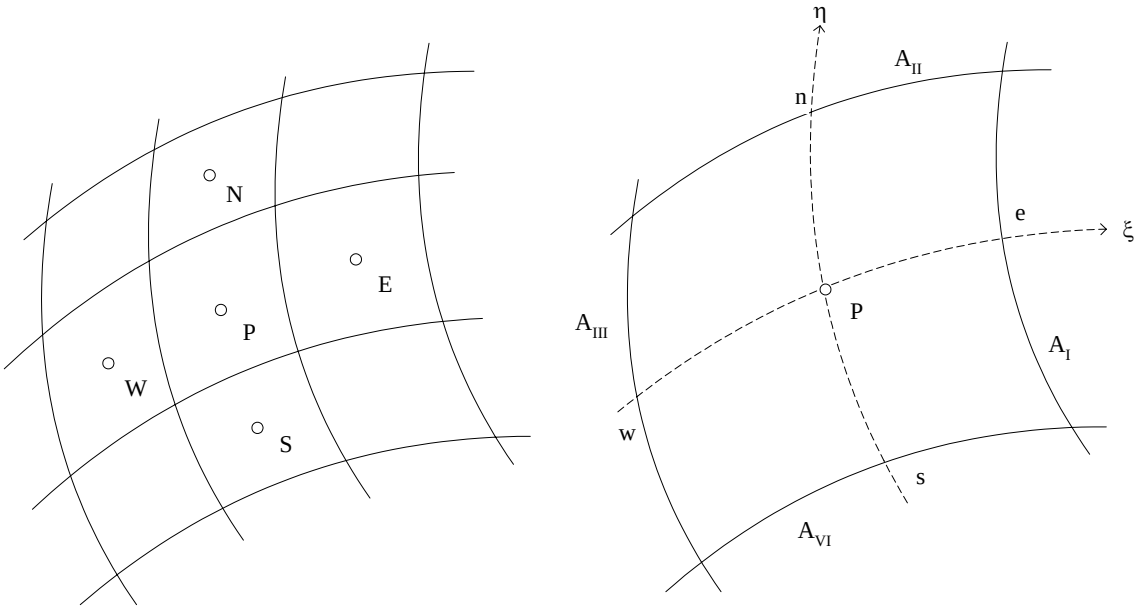

(a) (b)

Fig. 4.2 (a) General curvilinear control volumes in 2-D (b) Enlarged view showing the control volume with nodal center "P" and the location of the cell faces.

As mentioned earlier that,

$$\vec{e}^{\xi} = \frac{\frac{\partial y}{\partial \eta}\vec{e}_x - \frac{\partial x}{\partial \eta}\vec{e}_y}{h_\eta} \tag{4.10}$$

and ds is the length of elemental arc and can be expressed as $ds = h_\eta d\eta$. The total flux $\vec{J}$ can be written mathematically in vector notations as:

$$\vec{J} = J_x \vec{e}_x + J_y \vec{e}_y = \left(\rho u \phi - \Gamma \frac{\partial \phi}{\partial x} \right) \vec{e}_x + \left(\rho v \phi - \Gamma \frac{\partial \phi}{\partial y} \right) \vec{e}_y \tag{4.11}$$

substituting Equations (4.10) and (4.11) into Equation (4.9) to obtain

$$J_e = \int_{A_I} \left[\rho \left(u \frac{\partial y}{\partial \eta} - v \frac{\partial x}{\partial \eta} \right) \phi - \Gamma \left(\frac{\partial \phi}{\partial x} \frac{\partial y}{\partial \eta} - \frac{\partial \phi}{\partial y} \frac{\partial x}{\partial \eta} \right) \right] d\eta \tag{4.12}$$

The gradient of a generic scalar field ϕ is expressed in Cartesian coordinates and needs to be represented by their counterparts in the transformed (ξ, η) physical plane. This can be accomplished by using the Chain-Rule as follows:

$$\frac{\partial \phi}{\partial x} = \frac{1}{Ja} \left(\frac{\partial y}{\partial \eta} \frac{\partial \phi}{\partial \xi} - \frac{\partial y}{\partial \xi} \frac{\partial \phi}{\partial \eta} \right) \tag{4.13}$$

$$\frac{\partial \phi}{\partial y} = \frac{1}{Ja} \left(\frac{\partial x}{\partial \xi} \frac{\partial \phi}{\partial \eta} - \frac{\partial x}{\partial \eta} \frac{\partial \phi}{\partial \xi} \right) \tag{4.14}$$

Substituting these relationships (Eqs. 4.13 and 4.14) into Equation 4.12 and with some mathematical manipulations, the following expression is obtained:

$$J_e = \left(\rho u^{\xi} h_\eta \phi \right)_e \Delta\eta - \frac{h_\xi h_\eta^2 \Delta\eta}{Ja} \left(\frac{\Gamma}{h_\xi} \frac{\partial \phi}{\partial \xi} \right)_e + \frac{h_\xi h_\eta^2 \Delta\eta}{Ja} \left(\vec{e}_\xi \bullet \vec{e}_\eta \right) \left(\frac{\Gamma}{h_\eta} \frac{\partial \phi}{\partial \eta} \right)_e \tag{4.15}$$

The third term in the RHS of the above equation contains the value of $\left(\vec{e}_\xi \bullet \vec{e}_\eta\right)$ which appears due to the non-orthogonality of the coordinate system and would disappear in an orthogonal system. This value can be represented mathematically as follows:

$$\vec{e}_\xi \bullet \vec{e}_\eta = \vec{e}^{\,\xi} \bullet \vec{e}^{\,\eta} = \frac{\frac{\partial x}{\partial \xi}\frac{\partial x}{\partial \eta} + \frac{\partial y}{\partial \xi}\frac{\partial y}{\partial \eta}}{h_\xi h_\eta} \tag{4.16}$$

For simplicity Equation (4.15) can be rewritten as:

$$J_e = J_{P,e} - J_{S,e} \tag{4.17}$$

where

$$J_{P,e} = \left(\rho u^\xi h_\eta \phi\right)_e \Delta\eta - \alpha_{\xi,e}\left(\frac{\Gamma}{h_\xi}\frac{\partial \phi}{\partial \xi}\right)_e \tag{4.18}$$

$$J_{S,e} = -\beta_{\xi,e}\left(\frac{\Gamma}{h_\eta}\frac{\partial \phi}{\partial \eta}\right)_e \tag{4.19}$$

$$\alpha_\xi = \frac{h_\xi h_\eta^2 \Delta\eta}{Ja} \tag{4.20}$$

$$\beta_\xi = \alpha_\xi \left(\vec{e}_\xi \bullet \vec{e}_\eta\right) \tag{4.21}$$

The J_P and J_S are referred to as the primary flux and secondary flux, respectively. As shown in Equation (4.18), the first term of the RHS represents the effects of convection in fluid flow problems, while the second term symbolizes the

diffusion contribution. This implies that the primary flux has both convection and diffusion input. In Equation (4.19), the secondary flux is solely diffusive and comes up due to the non-orthogonality of the coordinate system and would disappear in an orthogonal coordinate system in which $\vec{e}_\xi \bullet \vec{e}_\eta = 0$, thus highlighting the fact that the non-orthogonality is one of the many sources of false diffusion.

Equations (4.20) and (4.21), for the quantities α_ξ and β_ξ, express the primary and secondary areas, respectively. These quantities assist the calculation of normal flux through a face from the gradiant along the grid lines. It should be noted that the grid spacing $\Delta\eta$, or $\Delta\xi$ that appear in calculations of the other fluxes (e.g. J_n), being set equal to unity in the computational plane and can be ignored in this formulation. These procedures can be repeated in the calculation of the other fluxes (i. g. J_n etc.) by switching to $\vec{e}^{\,\eta}$ instead of $\vec{e}^{\,\xi}$, such a procedure can be found in APPENDIX A.

It has to be noted that the contravariant velocity projection was used in the primary flux Equation (4.18) to facilitate the calculation of flow rate through a control volume face, as explained in Section 3.3.2. It can be proven that the contravariant velocity projection can be expressed as a linear combination of both (ξ and η) covariant velocity projections at that face of the control volume to obtain the following:

$$u^\xi = \vec{V} \bullet \vec{e}^{\,\xi} = \frac{\left(u\frac{\partial y}{\partial \eta} - v\frac{\partial x}{\partial \eta} \right)}{h_\eta} = \frac{\left(\alpha_\xi u_\xi - \beta_\xi u_\eta \right)}{h_\eta} \tag{4.22}$$

The RHS of governing Equation (4.7) is the volumetric source term over the control volume and can be evaluated as:

$$\int_V SdV = \int_V (S) Jad\xi d\eta \tag{4.23}$$

If the source term is assumed to be constant over the control volume, then Equation (4.23) can be rewritten as:

$$\int_V SdV = (SJa)\Delta\xi\Delta\eta = SJa \tag{4.24}$$

Combining the expression for various flux quantities and the volume integral of the source term into one equation as:

$$\left(J_{P,e} - J_{S,e}\right) - \left(J_{P,w} - J_{S,w}\right) + \left(J_{P,n} - J_{S,n}\right) - \left(J_{P,s} - J_{S,s}\right) = SJa \tag{4.25}$$

The secondary fluxes have to be calculated explicitly in order to avoid a nine-point formulation. These terms turn out to be less significant if the grid is almost orthogonal. All terms that represent the secondary fluxes will be treated as a source term and the above equation can be rewritten as:

$$J_{P,e} - J_{P,w} + J_{P,n} - J_{P,s} = b_S + b_{NO} \tag{4.26}$$

where

$$b_S = SJa \tag{4.27}$$

$$b_{NO} = J_{S,e} - J_{S,w} + J_{S,n} - J_{S,s} \tag{4.28}$$

Equation (4.27), for b_S, denotes the volumetric source term and b_{NO}, Equation (4.28), represents the source term due to the non-orthogonality of the coordinate system.

The primary flux in Equation (4.18) includes the value of ϕ and its gradient at the control volume interface. From a computational point of view, it is more convenient to express the cell fluxes in terms of nodal quantities. The next section explains how the interface fluxes may be properly and consistently expressed in terms of nodal values.

4.3 Differencing Scheme

Equation (4.26) represents the conservation of a generic transport equation over a control volume in terms of interface quantities. In order to find an equation involving ϕ in terms of the neighboring grid points, an appropriate profile assumption expressing the variation of ϕ at the interface is required. Several schemes are available for this intention, which have lead to the study of the properties of differencing schemes.

4.3.1 Properties of Differencing Schemes

Conservation is one of the most important properties of a differencing scheme. To ensure conservation of ϕ for the entire solution domain the flux of ϕ leaving a control volume across a particular face must be equal to the flux of ϕ entering the neighboring control volume through the same face. The flux through a common face must be represented in a consistent manner in adjacent control volumes. Consequently, such a scheme will maintain the conservation of the property of ϕ.

The discretized equations at each grid point correspond to a set of algebraic equations that need to be solved. In general, iterative numerical techniques are used to solve these sets of equations. These techniques initiate the solution process from a guessed value for ϕ in the entire domain of interest, and then a successive update is carried out until convergence is achieved. The condition for the convergent iterative technique, known as Scarborough criterion, is expressed in terms of the values of the coefficients of the discretized equations. If the differencing scheme results in coefficients that fulfill this criterion, the resulting matrix of coefficients is diagonally dominant. Diagonal dominance is a desirable feature for satisfying the convergence criterion, and if the discretization scheme does not satisfy this requirement it is possible that the solution converges slowly or does not converge at all.

The transport property of fluid flow can be illustrated by considering the non-dimensional cell Peclet number as a measure of the relative strengths of convection and diffusion. In case of pure diffusion the fluid is stagnant and the property ϕ will be spread equally in all directions, in which a simple central differencing scheme would be

a good choice. However, as the Peclet number increases, the property ϕ at a certain nodal point becomes increasingly influenced towards the upstream direction and the central differencing scheme is not a choice here. It is very important that the differencing scheme bear out the relationship between the magnitude of the Peclet number and the flow direction.

It has to be noted that all of the available schemes are concerned with the calculation of the primary fluxes due to the combination of two different natures of fluxes (e.g. convection and diffusion fluxes). The gradients in the secondary fluxes are typically evaluated by simple central differences across the cell faces. The assumption of a linear profile is inappropriate in convection-diffusion flow especially if the convection term is dominant. Hence, another profile that accounts for the "upwind" influence nature of convection must be considered.

4.3.2 Upwind Differencing Scheme

In central differencing, the value of a property ϕ at a cell face is always influenced by both nodal points adjacent to that face. The inability of sensing the flow direction associated with the central differencing scheme underestimates the value of this scheme. The above treatment is unsuitable in case of a strong convective flow because the cell face should receive more influence from the upstream nodal point. The upwind differencing scheme considers the flow direction when assigning the cell face value. The property ϕ at a cell face is set to be equal to the value of the upstream nodal point.

The upwind differencing scheme has a consistent expression and the formulation is conservative. The coefficients of the discretized equations construct a diagonally dominant matrix which ensures convergence. Since the scheme is based on the backward differencing formulation, its accuracy is only first order on the basis of Taylor series truncation error which accounts for wide applications in early CFD applications. The major drawback of this scheme is that it produces false diffusion terms in the calculation when the flow is not aligned with the grid lines. In flows of high Reynolds numbers, false diffusion can be large enough to result in physically incorrect solutions. Therefore, the upwind differencing scheme is not totally suitable for accurate flow calculations and an improved discretization scheme has been sought.

4.3.3 Power-law Scheme

The power law scheme presented by Patankar (1980) is a very popular scheme used in finite volume methods and produces better results than the upwind scheme. It is actually a curve fit to the exact exponential solution of the steady state one-dimensional convection-diffusion problem with constant diffusivity and no source term. The power law scheme has the ability to switch between a central differencing scheme and an upwind differencing scheme depending on the value of the Peclet number. This scheme has proved to be useful in practical flow calculations and has been used by some commercial computer cods.

Following Patankar's formulation, the primary flux $J_{P,e}$ (Eq. 4.18) which combines both convective and diffusive fluxes is evaluated by using a polynomial expression in terms of the cell Peclet number as follows:

$$J_{P,e} = F_e\phi_E + A(P_e)D_e(\phi_P - \phi_E) \tag{4.29}$$

where $A\left(\left|P_e\right|\right)$ is the polynomial expression defined by Patankar (for interface e) as:

$$A\left(\left|P_e\right|\right) = \max\left[\left[0,\left(1-0.1\left|P_e\right|^5\right)\right]\right] \tag{4.30}$$

The non-dimensional cell Peclet number, P, is defined as the measure of the relative strengths of the flow rate through a control surface, F, and the diffusional conductance, D, as follows:

$$P_e = \frac{F_e}{D_e} \tag{4.31}$$

where

$$F_e = \left(\rho u^{\xi} h_{\eta}\right)_e = \rho_e\left(\alpha_{\xi}u_{\xi} - \beta_{\xi}u_{\eta}\right)_e \tag{4.32}$$

and

$$D_e = \left(\frac{\Gamma\alpha_{\xi}}{h_{\xi}}\right)_e \tag{4.33}$$

It has to be noted that equation (4.29) represents the total flux at interface e in terms of the nodal points adjacent to it unlike Equation (4.18). It may be recalled that on account of the grid spacing, $\Delta\xi$ and $\Delta\eta$ being set equal to unity in the computational plane, they do not appear in the above equations. Equations (4.29-4.33) can easily be repeated for other interfaces (i.e., w, n and s) and they can be found in APPENDIX B.

Now is the time to find the discretization equations that constitute a set of linear algebraic equations which are solved to get the value of ϕ at nodal points in the calculation domain. This will be discussed in the following section.

4.4 Discretization Equation for a Generic Transport Property ϕ

Before finding the generic transport property ϕ in the discretized form, the source term S, in Equation (4.25), needs to be discretized first. In a practical situation, the source term S is a function of the dependent variable ϕ_P itself, and this relationship should be employed in constructing the discretization equations. Since the linear algebra method is used to solve the algebraic equations, only a linear relationship can be considered as an acceptable choice. The linearized source term is expressed as $S = S_C + S_P\phi_P$ where S_C is a constant and S_P must be negative to fulfill the Scarborough criterion.

Substituting the expression for the primary fluxes and the source term, the discretization equation for ϕ can be written as:

$$a_P \phi_P = a_E \phi_E + a_W \phi_W + a_N \phi_N + a_S \phi_S + b \tag{4.34}$$

where

$$a_E = D_e A(|P_e|) + \max[[0, -F_e]] \tag{4.35}$$

$$a_W = D_w A(|P_w|) + \max[[0, F_w]] \tag{4.36}$$

$$a_N = D_n A(|P_n|) + \max[[0, -F_n]] \tag{4.37}$$

$$a_S = D_s A(|P_s|) + \max[[0, F_s]] \tag{4.38}$$

$$a_P = a_E + a_W + a_N + a_S - S_P Ja \tag{4.39}$$

The source b in Equation (4.34) can be expressed as $b = b_S + b_{NO}$ where $b_S = S_C Ja$ and b_{NO} is given earlier in Equation (4.28).

Following the same procedure, the discretized continuity equation can be easily derived as follows:

$$F_e - F_w + F_n - F_s = 0 \tag{4.40}$$

4.5 Discretization of the Momentum Equations

Equation (4.4) represents the governing equations of the conservation of momentum. These equations can be discretized along the same steps outlined in the above sections if Cartesian velocity components were used, irrespectively of the choice of the dependent variables in the momentum equations. On the other hand, when choosing the curvilinear velocity components or projections as the dependent variables in the momentum equations the procedure is slightly different. The differential equations for curvilinear velocity will have curvature source terms because these velocity components/projections do not have a fixed direction.

Karki (1986) presented a formulation in which the curvature source terms are obtained by algebraic manipulation of the discretization equations. This would eliminate the complications and difficulties of programming these extra terms if the discretization equations were obtained by the conventional method. These curvature source terms could be avoided if discretization is carried out in a locally fixed coordinate system. In his formulation, the derived discretization equation includes parallel velocities, instead of the actual velocities, at the neighboring points for the velocity $u_{\xi,P}$ in a local coordinate system, as shown in Fig. 4.3.

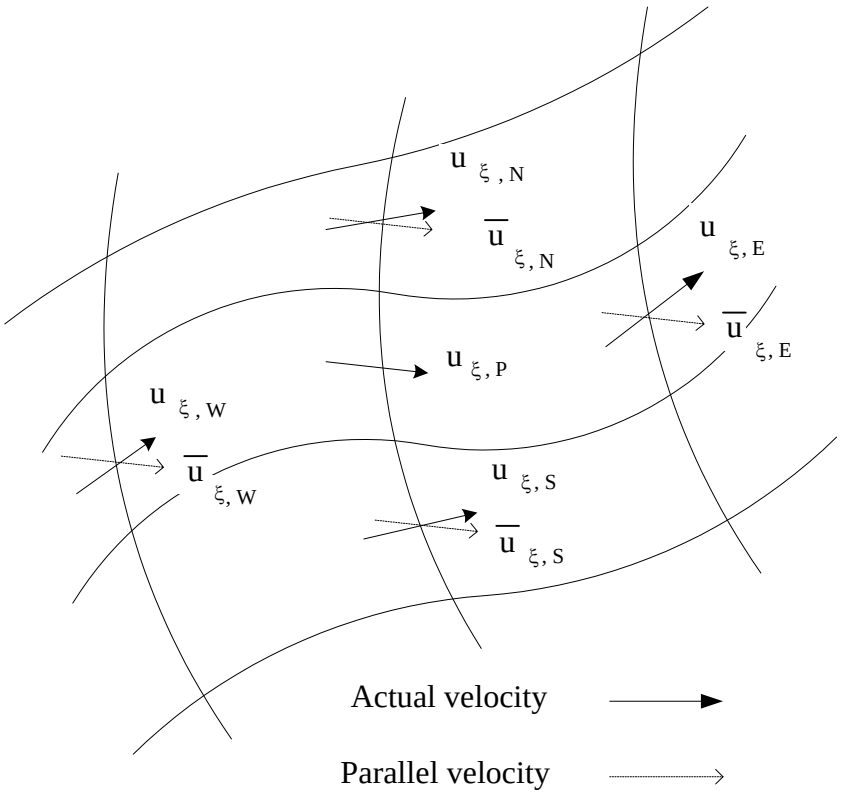

Fig. 4.3 Actual and parallel neighboring velocity to $u_{\xi,P}$.

For a highly non-orthogonal grid, the numerical scheme of the discretization equation as such may not give a converged solution. This problem can be eliminated by adding and subtracting the actual velocities in the discretization equation, as follows:

$$\begin{aligned} a_P u_{\xi,P} = {} & a_E u_{\xi,E} + a_W u_{\xi,W} + a_N u_{\xi,N} + a_S u_{\xi,S} + b \\ & + a_E \left(\overline{u}_{\xi,E} - u_{\xi,E} \right) + a_W \left(\overline{u}_{\xi,W} - u_{\xi,W} \right) \\ & + a_N \left(\overline{u}_{\xi,N} - u_{\xi,N} \right) + a_S \left(\overline{u}_{\xi,S} - u_{\xi,S} \right) \end{aligned} \tag{4.41}$$

where the source term b represents the external body force (e.g., pressure gradient) and the terms $\bar{u}_{\xi,E}$, $\bar{u}_{\xi,W}$, $\bar{u}_{\xi,N}$, and $\bar{u}_{\xi,S}$ are the neighboring velocity components parallel to $u_{\xi,P}$. Thus, $\bar{u}_{\xi,E}$, as an example, can be expressed as:

$$\bar{u}_{\xi,E} = \vec{V}_E \bullet \vec{e}_{\xi,P} = \frac{\left[u_E \left(\frac{\partial x}{\partial \xi} \right)_P + v_E \left(\frac{\partial y}{\partial \xi} \right)_P \right]}{h_{\xi,P}} \tag{4.42}$$

It has to be noted that the last four terms in RHS of Equation (4.41) represent the curvature source terms and are equivalent to the discretized non-orthogonal source terms. The same procedure can be used to find the discretized equation in η-direction which is given here for ease of reference:

$$\begin{aligned} a_P u_{\eta,P} = {} & a_E u_{\eta,E} + a_W u_{\eta,W} + a_N u_{\eta,N} + a_S u_{\eta,S} + b \\ & + a_E \left(\bar{u}_{\eta,E} - u_{\eta,E} \right) + a_W \left(\bar{u}_{\eta,W} - u_{\eta,W} \right) \\ & + a_N \left(\bar{u}_{\eta,N} - u_{\eta,N} \right) + a_S \left(\bar{u}_{\eta,S} - u_{\eta,S} \right) \end{aligned} \tag{4.43}$$

Equation (4.41) and (4.43) represent the momentum discretization equations in ξ- and η-direction, respectively, to be solved for the velocity field. An additional equation is needed to be solved for the pressure field. Discretization of the continuity Equation (4.40) cannot be considered as the governing equation for the pressure variable. In this

case, coupling between the velocity and continuity equations is needed to come up with a proper equation for the pressure variable and this will be discussed in the next section.

4.6 Coupling of the Momentum and Continuity Equations

Solving the momentum equations would give the solution of the velocity field if the pressure gradient is known *a priori*. Hence, the resulting velocity field should satisfy the continuity equation. In general principle of flow computations, the calculation of the pressure field is part of the solution and its gradient is not typically known in advance. Coupling between pressure and velocity initiates a constraint on the solution of the flow field because all equations are highly coupled since every velocity component appears in each momentum equation and the continuity equation.

The Semi-Implicit Method for Pressure Linked Equations (SIMPLE) algorithm of Patankar and Spalding (1972) is an iterative solution strategy, in which the convective fluxes through cell faces are evaluated from a so-called guessed velocity field. Moreover, a guessed pressure field is employed to solve the momentum equations and a pressure correction equation, constructed from the continuity equation, is solved to get a pressure correction field which is sequentially used to update the velocity and pressure field. This process is repeated until convergence is achieved for the velocity and pressure fields.

To start the SIMPLE calculation process a guessed pressure field p^* is assumed first. Then, the guessed velocity u_ξ^*, at point e, can be obtained from the following momentum equation:

$$a_e u_{\xi,e}^* = \sum a_{nb} u_{\xi,nb}^* - \Delta V \frac{dp^*}{dx} + b \tag{4.44}$$

where the subscript nb stands for the neighboring points. The guessed pressure field p^* is corrected by adding the correction pressure field p' as follows:

$$P = P^* + P' \tag{4.45}$$

Similarly, the velocity correction field u_ξ' can be related to the correct velocity and to the guessed velocity u_ξ^* as follows:

$$u_\xi = u_\xi^* + u_\xi' \tag{4.46}$$

Substitution of the correct pressure field p into the momentum equation yields the correct velocity field u_ξ by solving the following equation:

$$a_e u_{\xi,e} = \sum a_{nb} u_{\xi,nb} - \Delta V \frac{dp}{dx} + b \tag{4.47}$$

From Equation (4.46), the relationship between the pressure correction and the velocity correction can be found by subtracting Equation (4.44) from Equation (4.47) as follows:

$$a_e u'_{\xi,e} = \sum a_{nb} u'_{\xi,nb} - \Delta V \frac{dp'}{dx} \tag{4.48}$$

The first term in the RHS of the above equation will be omitted. This omission is considered as the main approximation of the SIMPLE algorithm. In fact, the omission of such terms does not affect the final solution because both pressure and velocity correction will be zero in a converged solution. Therefore, Equation (4.48) can be rewritten as:

$$u'_{\xi,e} = \frac{\Delta V}{a_e} \frac{dp'}{dx} \tag{4.49}$$

It has to be noted that a_e is not the same as a_E. The quantity a_e represents the summation of the neighboring coefficients at that node e, and a_E were given earlier in Equation (4.35). So far, the pressure gradient in Equation (4.49) is in the differential form and has to be discretized. The discretization of the continuity Equation requires the value of the pressure gradient at a location midway between the nodes. A quasi-one-dimensional central differencing scheme is appropriate in this case (Karki 1986). The pressure gradients at the interface e, for example, can be written as follows:

$$\left(\frac{\partial P}{\partial x}\right)_e = \frac{P_E - P_P}{\Delta x} \tag{4. 50}$$

Therefore, the velocity correction in Equation (4.49) can be written as:

$$u'_{\xi,e} = d_e \left(p'_P - p'_E \right) \tag{4. 51}$$

where

$$d_e = \frac{\Delta V}{a_e \Delta x} \tag{4. 52}$$

The discretized continuity equation given in Equation (4.40) represents the summation convective fluxes through all interfaces of an element. The flux through interface e, for example, is given earlier as:

$$F_e = \rho_e \left(\alpha_\xi u_\xi - \beta_\xi u_\eta \right)_e \tag{4. 53}$$

As can be seen, the flow rate at the interface involves two velocities. The term involving the secondary area β arises due to the non-orthogonality of the coordinate system. The first term can be treated as guessed and corrected velocity as follows:

$$\rho_e \alpha_{\xi,e} \left(u_\xi \right)_e = \rho_e \alpha_{\xi,e} \left(u_\xi^* + u'_\xi \right)_e \tag{4. 54}$$

The velocity corrections are related to the pressure corrections by Equation (4.51). Substituting these terms back in the flow rate expression, F_e can be expressed as:

$$F_e = \rho_e \left[\alpha_{\xi,e} u_{\xi,e}^* + \alpha_{\xi,e} d_e \left(P'_P - P'_E \right) - \beta_{\xi,e} u_{\eta,e} \right] \tag{4. 55}$$

Expressions similar to this equation are obtained for the other flow rates and substituted in the discretized continuity equation to derive an expression involving the pressure corrections. Rearranging the terms, the result is the pressure correction equation and can be cast into the following form:

$$a_P P'_P = a_E P'_E + a_W P'_W + a_N P'_N + a_S P'_S + b + b_{NO} \tag{4. 56}$$

where

$$a_E = \alpha_{\xi,e} \rho_e d_e \tag{4. 57}$$

$$a_W = \alpha_{\xi,w} \rho_w d_w \tag{4. 58}$$

$$a_N = \alpha_{\eta,n} \rho_n d_n \tag{4. 59}$$

$$a_S = \alpha_{\eta,s} \rho_s d_s \tag{4. 60}$$

$$a_P = a_E + a_W + a_N + a_S \tag{4. 61}$$

and

$$b = \left(\alpha_\xi \rho u_\xi^*\right)_w - \left(\alpha_\xi \rho u_\xi^*\right)_e + \left(\alpha_\eta \rho u_\eta^*\right)_s - \left(\alpha_\eta \rho u_\eta^*\right)_n \tag{4. 62}$$

$$b_{NO} = \left(\beta_\xi \rho u_\eta\right)_e - \left(\beta_\xi \rho u_\eta\right)_w + \left(\beta_\eta \rho u_\xi\right)_n - \left(\beta_\eta \rho u_\xi\right)_s \tag{4. 63}$$

Equations (4.41), (4.43), and (4.56) should be solved iteratively until convergence is achieved. The resulting solution would give the pressure and velocity field of the domain of interest if the boundary conditions were specified. The discretization of the boundary control volume depends on the given boundary conditions. This will be discussed in the following section.

4.7 Boundary Conditions

It is important to specify the boundary conditions correctly because they play a significant role in all CFD problems. This section describes the implementation of various kinds of boundary conditions that will be encountered in this study. The boundary conditions can be classified as: (i) inlet, (ii) outlet, (iii) wall, and (iv) symmetry conditions.

4.7.1 Inlet Boundary Conditions

Normally the values of the various variables in the computational domain entrance are known *a priori*. Therefore, a direct substitution of these values into the disceretization equations for the boundary control volume can easily be done with no further complications. It has to be noted that the boundary condition for pressure is not necessary as a result of employing the staggered grid arrangement.

4.7.2 Outlet Boundary Conditions

Limiting the computations to a predetermined region can be done by applying an artificial boundary condition at the outflow boundary. The location of the outlet has to be set in a position far away from the physical boundary to attain a fully developed state where no change takes place in the flow direction. Therefore, the position of such a boundary would not affect the results in the domain of interest. With such a boundary condition, the streamwise gradients of all variables is set to zero.

4.7.3 Wall Boundary Conditions

The most common boundary condition that comes across in a confined fluid flow problem is the wall boundary condition. The no-slip condition, valid for viscous flows, can be enforced for the velocities. Consequently, the velocity of the fluid at the wall must be equal to the velocity of the wall (i.e., zero in most of the cases). Two types of conditions are available for temperature, either constant wall temperature or constant heat flux.

4.7.4 Symmetry Boundary Conditions

The condition is similar to the wall boundary conditions, in a sense, as no flow crosses the boundary. Therefore, the normal component of velocities and the normal gradient of the parallel component of velocity is zero. This can be achieved by setting the appropriate coefficient (a_N , a_E ,.. etc.) to zero.

At this point the explanation of the entire scheme is completed, and it is time to discuss the way this scheme can be implemented. In the next chapter, the convergence criteria along with the code validations will be presented.

CHAPTER V

CODE VALIDATION

A finite volume formulation was explained in the previous chapter for flows in a general curvilinear coordinate system. In order to validate the developed FORTRAN code, several test problems were solved and predictions using the developed code were compared with either exact or experimental solutions for the benchmark problems available in literature. In some cases the code was validated by comparing numerical predictions against the numerical solutions available in literature. The benchmark problems chosen for the purpose of validation are: (1) developing a flow in a parallel plate channel subjected to constant wall temperature; (2) viscous flow in gradual expansion; (3) flow through a wavy channel; and (4) flow over a series of circular cylinders confined in a parallel plate channel.

5.1 Convergence Criteria

Before going into the details of each test problem, the convergence criteria needs to be discussed. Since an iterative solution technique is used in this calculation, the widely used method to check for convergence is to compare the values of the field variables at successive iterative steps. However, low under-relaxation factors coupled with a small magnitude of field variables led to very slow and small changes in the

variables. These imply that this particular technique is unsuitable for declaring convergence criteria.

Another technique proposed by Patankar (1980) is to check the magnitude of the source term in the pressure equation, which is the mass residue in each control volume. The convergence could be declared if the maximum of the absolute value of the mass residue is less than a very small number ε (e.g. 10^{-5}). In this study, convergence is declared by monitoring the sum of the residues at each node. Since the magnitude of u_ξ and u_η are not known *a priori*, monitoring the relative residuals are more meaningful. The relative convergence criteria for u_ξ and u_η are defined as follows:

$$\bar{R}_{u_\xi} = \frac{\sum_{nodes} \left| a_e u_{\xi,e} - \sum a_{nb} u_{\xi,nb} - b_{u_{NO}} - A_e (P_P - P_E) \right|}{\sum_{nodes} \left| a_e u_{\xi,e} \right|} \leq \varepsilon \tag{5.1}$$

$$\bar{R}_{u_\eta} = \frac{\sum_{nodes} \left| a_n u_{\eta,n} - \sum a_{nb} u_{\eta,nb} - b_{u_{NO}} - A_n (P_P - P_N) \right|}{\sum_{nodes} \left| a_n u_{\eta,n} \right|} \leq \varepsilon \tag{5.2}$$

In the pressure equation, it is appropriate to check for mass imbalance in the continuity equation. The convergence criterion for pressure is defined as follows:

$$R_P = \sum_{nodes} \left| b + b_{NO} \right| \leq \varepsilon \tag{5.3}$$

where b and b_{NO} were defined previously and will be written again for the sake of convenience:

$$b = \left(\alpha_\xi \rho u_\xi^*\right)_w - \left(\alpha_\xi \rho u_\xi^*\right)_e + \left(\alpha_\eta \rho u_\eta^*\right)_s - \left(\alpha_\eta \rho u_\eta^*\right)_n \tag{4. 62}$$

$$b_{NO} = \left(\beta_\xi \rho u_\eta\right)_e - \left(\beta_\xi \rho u_\eta\right)_w + \left(\beta_\eta \rho u_\xi\right)_n - \left(\beta_\eta \rho u_\xi\right)_s \tag{4. 63}$$

The convergence criterion for temperature is defined as follows:

$$R_T = \sum_{nodes} \left| a_P T_P - \sum a_{nb} T_{nb} - b_{T,NO} \right| \le \varepsilon \tag{5.4}$$

The numerical iteration criterion required that the normalized residuals of mass, momentum, and energy be less than 10^{-6} for all test problems.

5.2 Test Problem #1: Flow Through Straight Channel Subjected to Constant Wall Temperature

The domain of interest in this test problem consists of an orthogonal rectangular grid as depicted in Fig. 5.1a. The main purpose of this part of this validation is to prove that all the non-orthogonal terms would vanish for an orthogonal grid and to show that

the code is capable of working in both orthogonal and non-orthogonal domains. These terms were explained earlier in the previous chapter.

As expected from classic results about this problem, the flow will be developing in the entrance region until it reaches a fully developed condition where no further changes in velocity profile takes place in the streamwise direction. Developing flow behavior is shown in Fig. 5.1b.

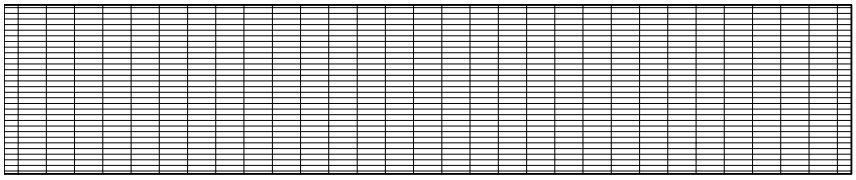

(a) Rectangular orthogonal grid.

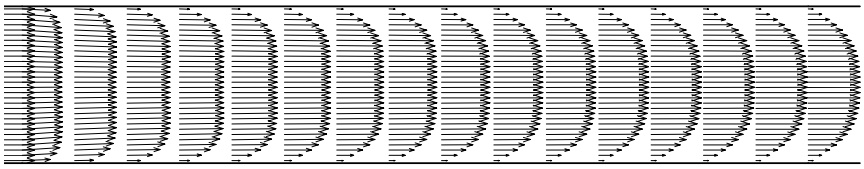

(b) Velocity profiles.

Fig. 5.1 Flow through a parallel plate channel: (a) Rectangular orthogonal grid (b) Velocity profiles.

Since the gradient of pressure at a fully developed region is constant, the velocity profile is parabolic where the point of maximum velocity is located along the centerline and equal to 1.5 of the mean velocity as shown in Fig. 5.2. The Nusselt number for a fully developed region between two parallel plates subjected to a constant wall temperature is 7.56 which agrees favorably with the Nusselt number 7.54 mentioned by many authors such as Incropera and DeWitt (1996).

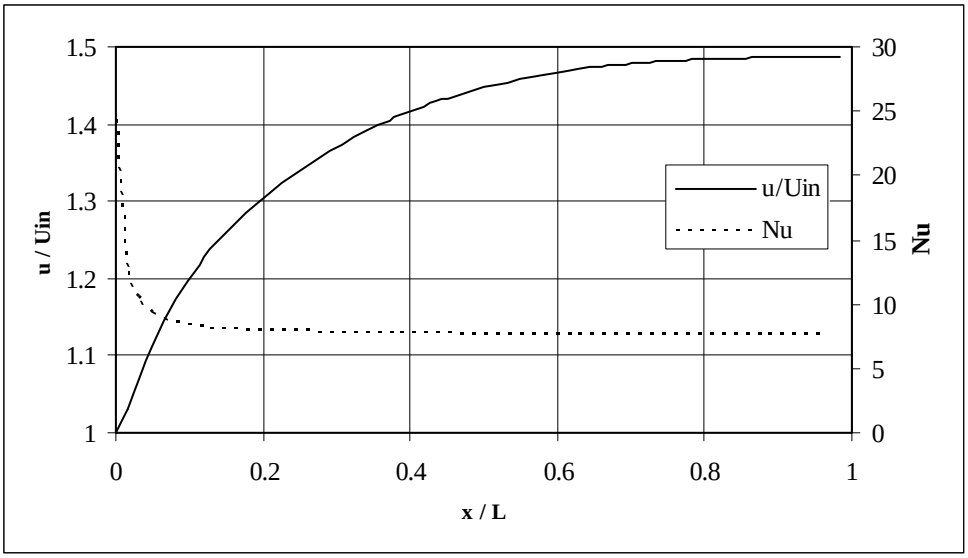

Fig. 5.2 Centerline velocity and Nusselt number distributions.

5.3 Test Problem #2: Flow Through a Gradual Expansion

The flow situation with smooth expansion was proposed as a test problem for the workshop of the International Association for Hydraulic Research (IAHR) by the Working Group on Refined Modeling of Flow in Rome (Napolitano and Orlandi 1985).

Fifteen different groups were involved separately in solving this problem and each result was compared with the benchmark solution. The computational schemes incorporated both finite difference (volume) and finite element techniques with either pressure-velocity coupling or vorticity-stream function formulation.

The shape of the channel wall was defined by the hyperbolic tangent function as:

$$Y_w = \frac{\tanh(2 - 30x/\mathrm{Re}) - \tanh(2)}{2} \tag{5.5}$$

where $0 < x < x_{out} = \mathrm{Re}/3$

As can be seen from Equation (5.5), the geometry of this domain or the boundary of the solid wall of the channel depends on the value of the Reynolds number (Re). The geometry is depicted in Fig. 5.3 for Re = 10 and becomes longer and smoother as the Re increases.

Half of the domain is studied because of the symmetric geometry. The governing equations for the flow are the continuity and momentum equations, the well-known Navier-Stokes equations in Cartesian coordinates. A no-slip boundary condition was specified at the wall boundary and both velocity components were assigned a value of zero. At the symmetry line, the transverse velocity and the normal gradient of the streamwise velocity are zero as follows:

$$v = \frac{\partial u}{\partial y} = 0 \tag{5.6}$$

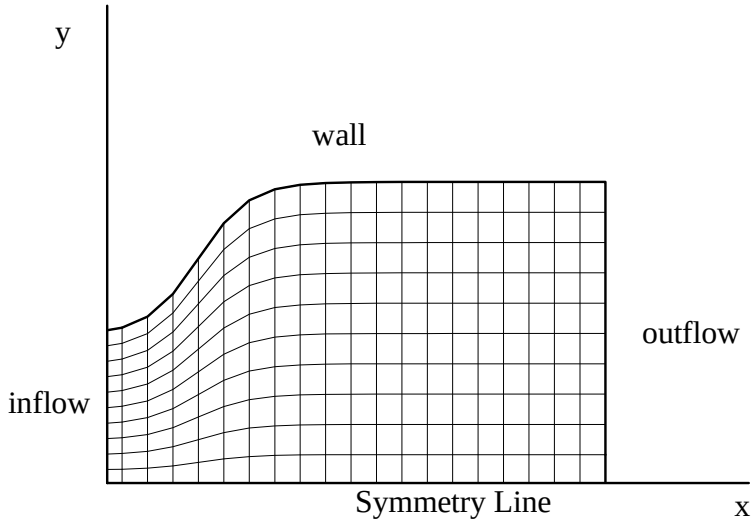

Fig. 5.3 Shape of gradual expansion channel for Re=10 with a discretized domain.

At the outflow boundary, an artificial boundary was set to pre-assumed (extrapolated) values for all variables from the interior of the computational domain. The flow is assumed to be fully developed at the inflow boundary and the velocity profile is given by the following expression:

$$u(0, y) = 3(1 - y) - (3/2)(1 - y)^2 \tag{5.7}$$

The discretized domain in Fig. 5.3 was generated algebraically using a normalizing transformation technique which was explained earlier in Section 1.3.1. The results presented in the workshop were obtained using 21x21 mesh with equal spacing between the grid points. The characteristic length is taken to be the channel half height at

the inflow boundary and the characteristic velocity is taken to be the bulk velocity at the inlet.

Solutions to the problems were requested from several researchers for both Re = 10 and Re = 100 and all results were assembled in one paper by Napolitano and Orlandi (1985). Among these results, the Solution by Cliffe et al. obtained by using the finite element technique on a 60x30 grid was the chosen (Benchmark) solution as it was believed to be grid independent. Values at locations $x = 0$ and $x = x_{out}$ were excluded from all presented results to minimize the impact of the singularity at the inlet and the arbitrariness of the outflow boundary condition.

The quantity used for comparison of the results was the predicted values of the pressure distribution at the solid wall of the channel. It was decided to fix the value of the pressure equal to zero on the wall at the mid section, where $x = x_{out} / 2$. Fig. 5.4a and b show the pressure distribution along the solid wall computed on a 21x21 staggered grid for Re = 10 and Re = 100, respectively. The predictions using the developed code (present work) were compared with the CJG which refers to the benchmark (interpolated) solution by Cliffe et al. (cited by Napolitano and Orlandi, 1985).

It was determined at the Rome conference to define the error estimates based on the deviation of the computed wall pressure from those of CJG as follows:

$$\varepsilon_P = \frac{100}{18} \sum_{i=2}^{20} \left| \frac{P_i - P_{i,CJG}}{P_{i,CJG}} \right| \tag{5.8}$$

The above error estimate is based on computed values at 19 equally spaced points. Both solutions for Re = 10 and 100 are seen to be remarkably accurate, despite the coarseness of the grid, even in the region with the steepest gradient. The average percentage error ε_P is found to be 3.34 and 2.06 for Re = 10 and 100, respectively. Errors are reduced by significantly reducing skewness and curvature of the generated grid at Re = 100.

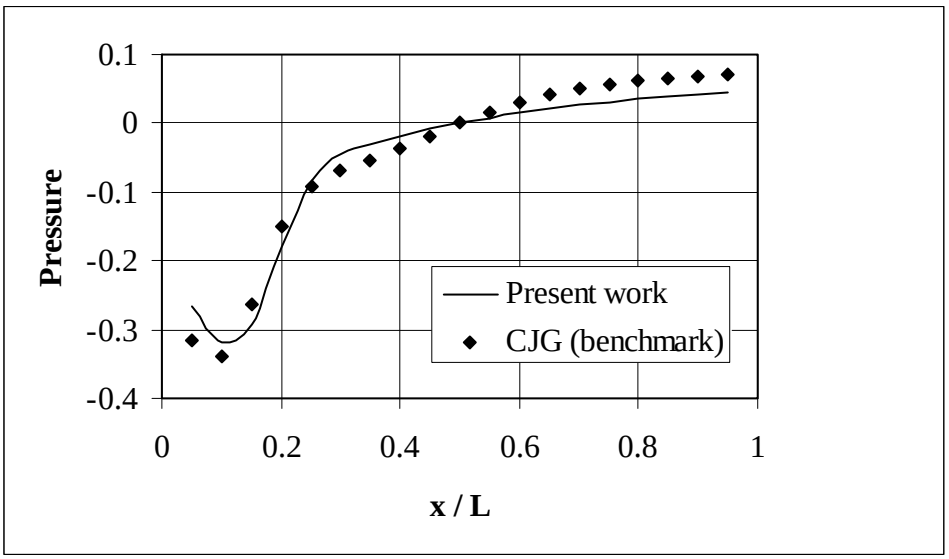

(a) Re = 10.

Fig. 5.4 Pressure distribution along the solid wall with gradual expansion at (a) Re = 10 (b) Re = 100.

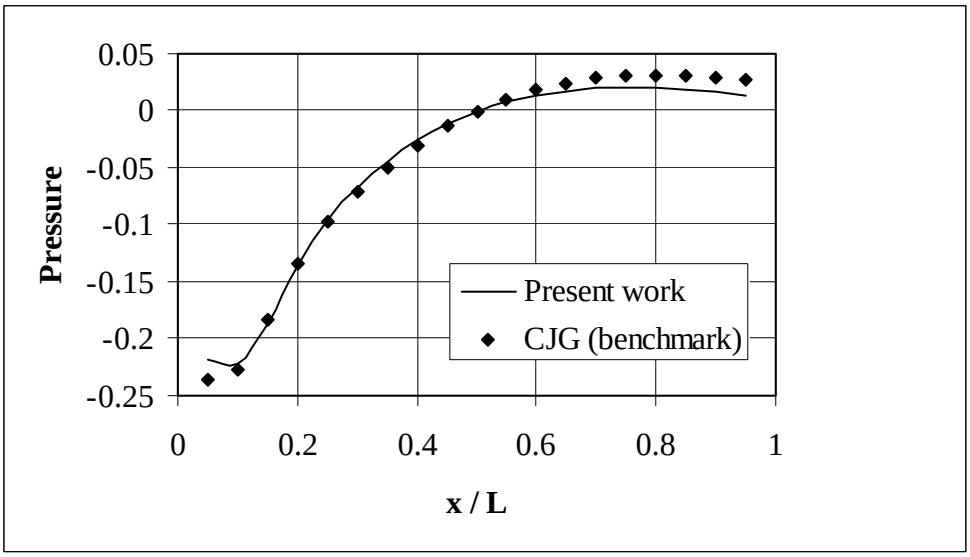

(b) Re = 100.

Fig. 5.4 (Continued).

5.4 Test Problem #3: Flow Through Wavy Channels

Niceno and Nobile (2001) studied numerically the two-dimensional steady and time-dependent fluid flow and heat transfer through periodic, wavy channels, for fluid with a Prandtl number of 0.7, by means of an unstructured co-volume method. The two geometrical configurations considered are the sinusoidal channel and the arc-shaped channel for H_{min}/H_{max} = 0.3 and L/a = 8 which are shown in Fig. 5.5a and 5.5b, respectively.

The numerical method used in their study is based on a time-accurate, control volume (CV) approach. The main characteristic of this method is the use of two families of CVs which are mutually orthogonal, and called complementary volumes or co-volumes for short. The computational domain is subdivided into a finite number of non-

overlapping polygon CVs for which a circumcircle can be defined. This family of CVs is called the primal grid. The other family of CVs (dual grid) is obtained by connecting the circumcenters of the primal grid polygons. For further information the reader may refer to Niceno and Nobile (2001).

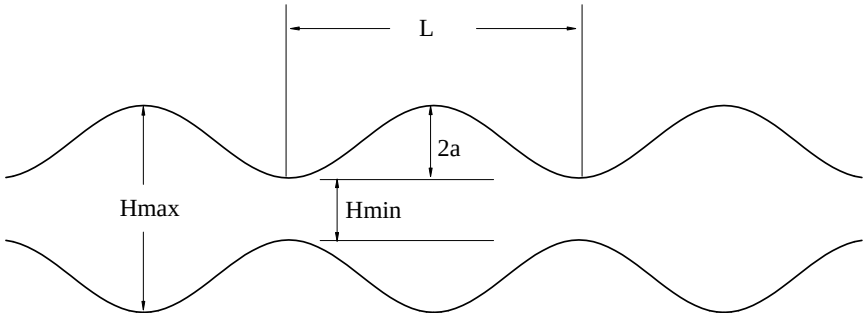

(a) Sinusoidal channel.

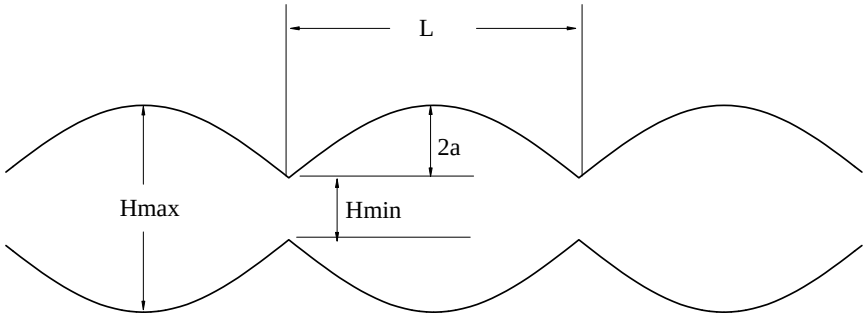

(b) Arc-shaped channel.

Fig. 5.5 Geometrical configurations of wavy channel (a) sine-shaped channel, (b) arc-shaped channel.

The flow is assumed to be two-dimensional and incompressible. For simplicity constant thermo-physical properties were assumed. Under these assumptions, the governing equations for fluid flow and energy transport can be written as:

Continuity: $$\nabla \bullet \vec{V} = 0 \tag{5.9}$$

Momentum: $$\frac{\partial \vec{V}}{\partial t} + (\vec{V} \bullet \nabla)\vec{V} = -\frac{1}{\rho}\nabla P + \nu \nabla^2 \vec{V} + S \tag{5.10}$$

Energy: $$\frac{\partial T}{\partial t} + (\vec{V} \bullet \nabla)T = \alpha \nabla^2 T \tag{5.11}$$

where $\vec{V}$ is the velocity field, τ is the time, ρ is the density, ν is the kinematic viscosity, S is the source term, T is the temperature and α is the thermal diffusivity. In this study, attention will be given only to the steady state solution part of their work.

The flow and temperature fields were studied under the assumption of a fully developed flow, which means that the flow repeats itself from module to module, and the heat transfer coefficient has reached its asymptotic value. Based on this assumption Niceno and Nobile (2001) analyzed only one module of the geometry. In this work, six consecutive modules were studied instead. The fully developed condition could be reached at the second or the third module and the results are comparable to those of Niceno and Nobile (2001).

A no-slip condition for velocity is enforced on the walls of the channels. For the temperature field, the channel was subjected to a constant wall temperature condition. A

non-dimensional temperature is introduced for the solution of the temperature field as follows:

$$\theta(x) = \frac{T(x) - T_w}{T_b(x) - T_w} \tag{5.12}$$

where T_w is the wall temperature, and T_b is the bulk temperature defined by:

$$T_b(x) = \frac{\int_H T(x)\vec{V} \cdot \vec{n} dy}{\int_H \vec{V} \cdot \vec{n} dy} \tag{5.13}$$

The heat transfer rate is represented by the Nusselt number, which is defined as:

$$Nu = \frac{\bar{h} D_H}{k} \tag{5.14}$$

where D_H is the hydraulic diameter, defined as twice the average channel height (H_{av} = $H_{max}/2 + H_{min}/2$). The space-averaged heat transfer coefficient $\bar{h}$, is given simply as a Riemann sum, which is defined as:

$$\bar{h} = \frac{Q}{(2L)(LMTD)} \tag{5.15}$$

with Q being the instantaneous, total heat flux in the module, and defined as follows:

$$Q = \rho C_P \left(T_b\left(MI\right) - T_b\left(MO\right)\right) \int_H \vec{V} \cdot \vec{n} dy \tag{5.16}$$

and LMTD is the log-mean temperature difference in a module, and defined as follows:

$$LMTD = \frac{\left(Tw - T_b\left(MO\right)\right) - \left(Tw - T_b\left(MI\right)\right)}{\ln\left(Tw - T_b\left(MO\right)\right) - \left(Tw - T_b\left(MI\right)\right)} \tag{5.17}$$

where *MI* and *MO* stand for module inlet and module outlet, respectively. The friction factor was computed based on its standard definition:

$$f = \frac{\left(P_m(MI) - P_m(MO)\right) H_{av}}{\left(L\right)\left(2\rho u_{av}^2\right)} \tag{5.18}$$

where P_m is the mean pressure and u_{av} is the average mean velocity of one module in the channel. The Reynolds number is defined as:

$$\mathrm{Re} = \frac{u_{av} H_{av}}{\nu} \tag{5.19}$$

Structured symmetric grids were used for the computations similar to the ones shown in Section 3.4.1 to ensure symmetric solutions. A grid refinement study was performed in order to assess the accuracy of the results. Table 5.1 gives a summary of a

grid independence test for both channels at different Reynolds numbers. It can be seen from the results that the values of the friction factor (f) and Nusselt number (Nu), obtained at different grids, vary by less than 1.8%, thus demonstrating the adequacy of the grid adopted and the numerical accuracy of the method.

TABLE 5.1 Results of grid independence test for test problem #3.

Sine-Shaped Channel		Grid 1 (1681 grid pts)	Grid 2 (3721 grid pts)	Grid 3 (6561 grid pts)
Re= 100	f	0.4153	0.4124	0.4115
	Nu	9.176	9.1527	9.1463
Re= 150	f	0.3096	0.3039	0.301
	Nu	9.4428	9.3689	9.3355

Arc-Shaped Channel		Grid 1 (1681 grid pts)	Grid 2 (3721 grid pts)	Grid 3 (6561 grid pts)
Re= 25	f	1.3907	1.4366	1.4651
	Nu	8.0156	7.7906	7.668
Re= 50	f	0.8061	0.8258	0.8407
	Nu	8.2336	7.9797	7.8408

All calculations presented here were obtained with the finest grid (6561 grid points). Figs. 5.6 and 5.7 show the calculated streamlines and the isotherms (normalized temperature) for the fourth module of both Sinusoidal-shaped and Arc-shaped channels at different Reynolds numbers.

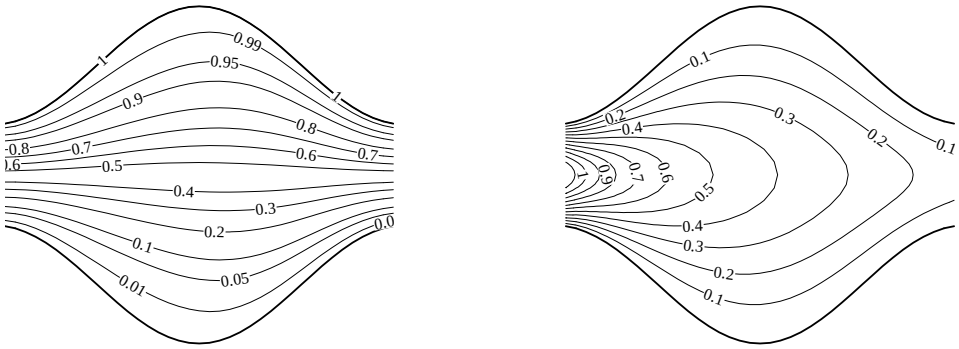

(a)

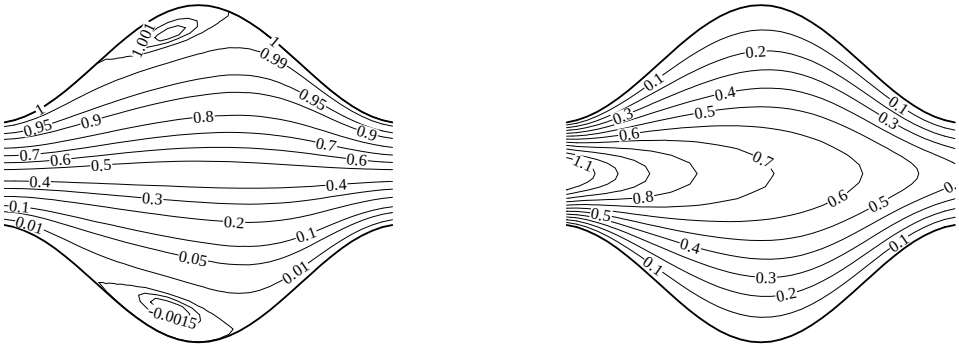

(b)

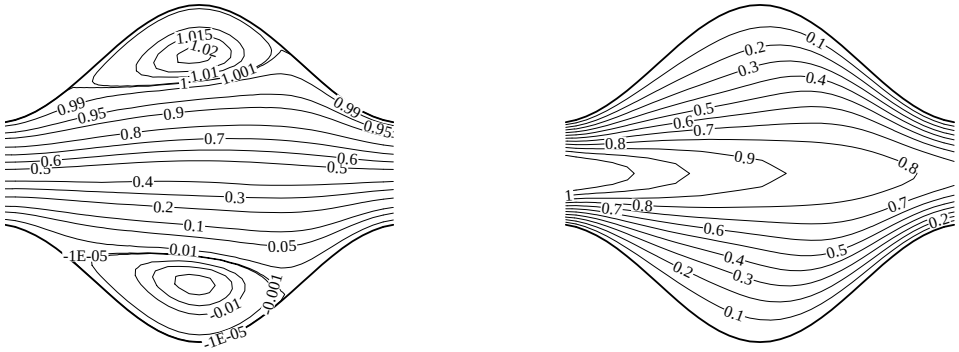

(c)

Fig. 5.6 Contours of stream functions (left) and normalized temperature (right) of the fourth module for a sine-shaped channel at various Reynolds numbers: (a) Re = 25; (b) Re = 50; (c) Re = 100.

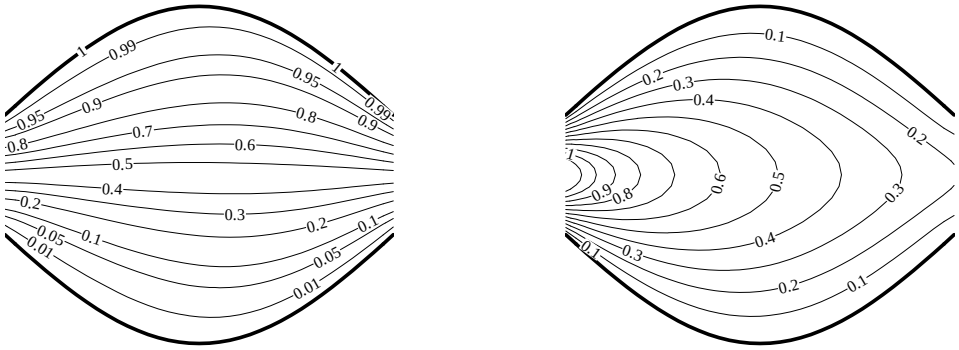

(a)

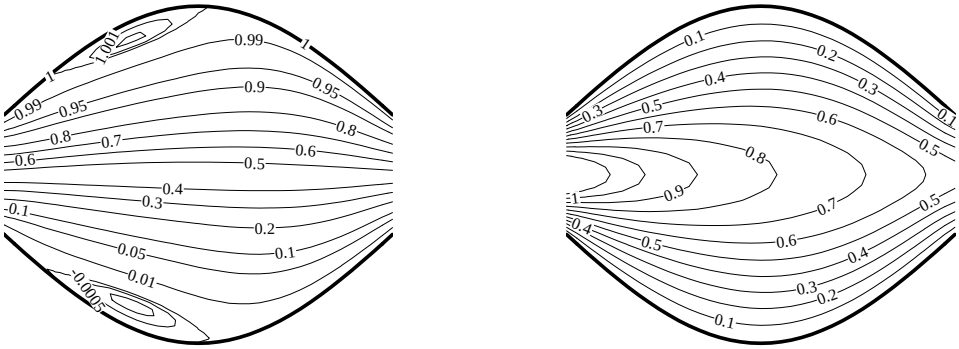

(b)

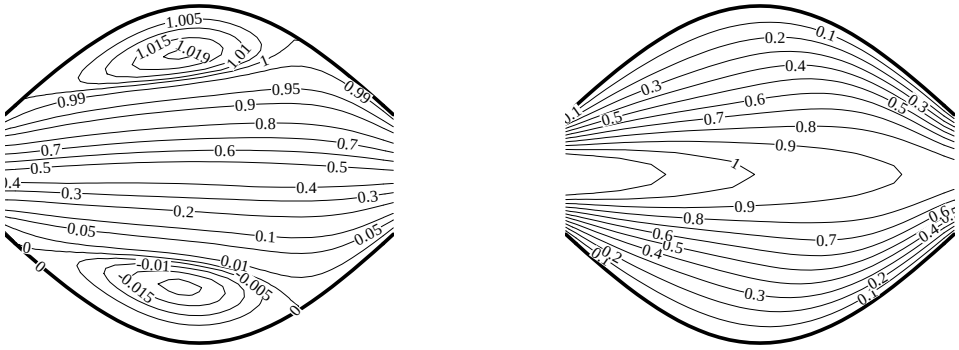

(c)

Fig. 5.7 Contours of stream functions (left) and normalized temperature (right) of the fourth module for an arc-shaped channel at various Reynolds numbers: (a) Re = 25; (b) Re = 50; (c) Re = 100.

The flow is seen to separate with an increase in Re, and the recirculation bubble increases in size and shifts downstream. Wang and Vanka (1995) presented a comparison of the calculated separation and reattachment points with the experimental data of Nishimura et al. (1990). They also presented the Nusselt number distributions along the walls of the sine-shaped channel. Fig. 5.8 shows the local Nusselt number presented by Wang and Vanka (1995) for one Periodically Fully Developed (PDF) module and the results generated from the present work of six consecutive modules. Disregarding the first module, the next five modules show that the flow has reached the fully developed condition as they have the same behavior and the results of PDF can fit to any one of them.

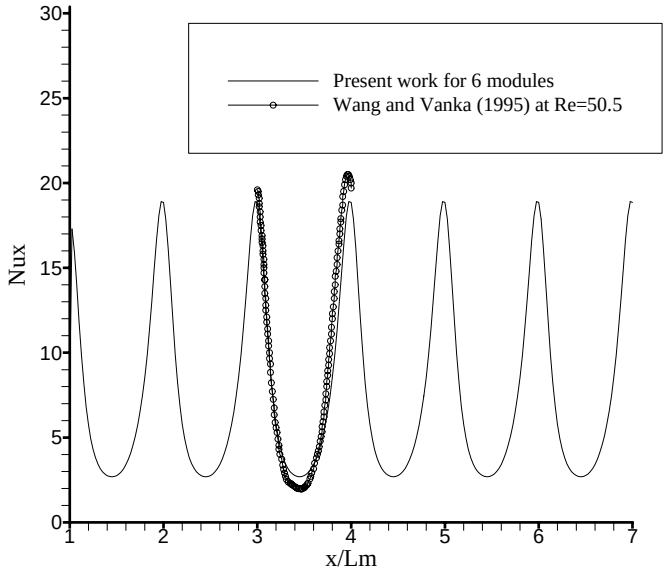

Fig. 5.8 Local Nusselt number along the walls of a sine-shaped channel.

The results obtained for the Sine-Shaped geometry are summarized in Fig. 5.9, where the Nusselt number (*Nu*) and the friction factor (*f*) for the periodically fully developed flows are given as a function of the Reynolds number (Re). The results obtained with the developed code agree with the numerical results of Niceno and Nobile (2001) and the experimental observations of Nishimura et al. (1990).

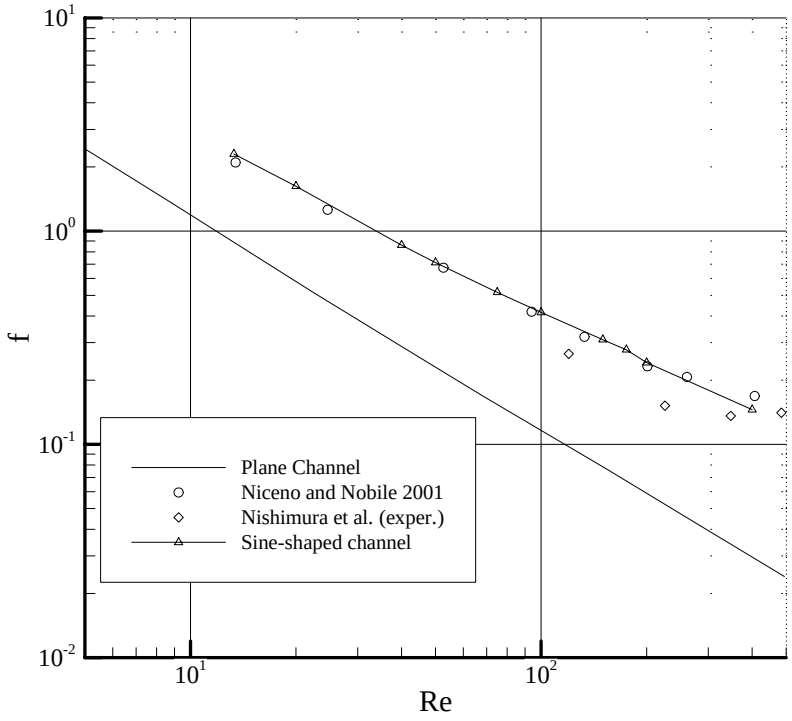

(a) Friction factor

Fig. 5.9 Code validation test problem #3 (a) Friction factor (b) Nusselt number.

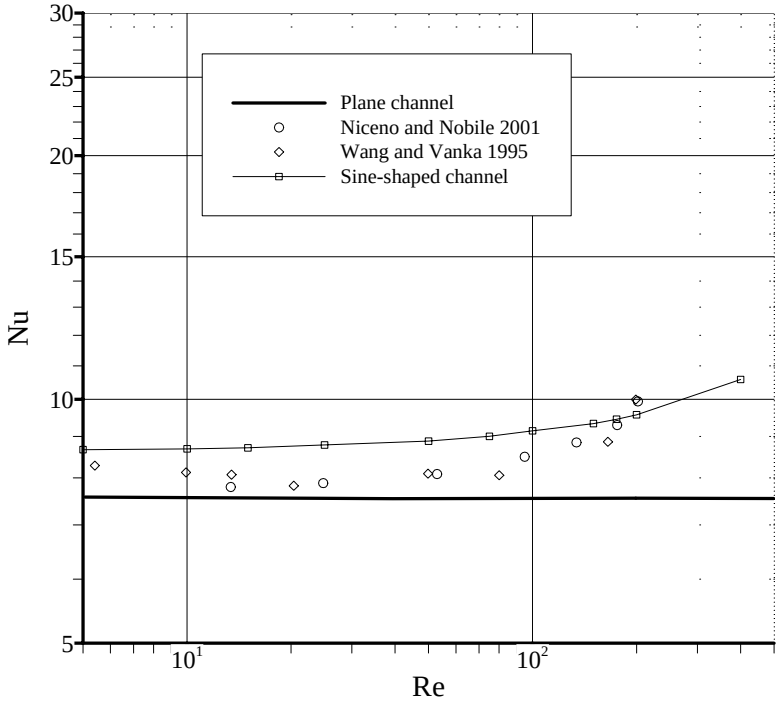

(b) Nusselt number as a function of Re.

Fig. 5.9 (Continued).

5.5 Test Problem #4: Flow Over Circular Cylinders

Fluid flow and heat transfer over a row of in-line cylinders placed between two parallel plates was studied numerically by Kundu et al. (1991a). A two-dimensional flow field is shown in Fig. 5.10. Kundu et al. (1991a) computed the flow field using a finite difference method. The physical domain was transformed into a computational domain so that a rectangular domain could be used. The fluid was assumed to be incompressible with constant thermophysical properties.

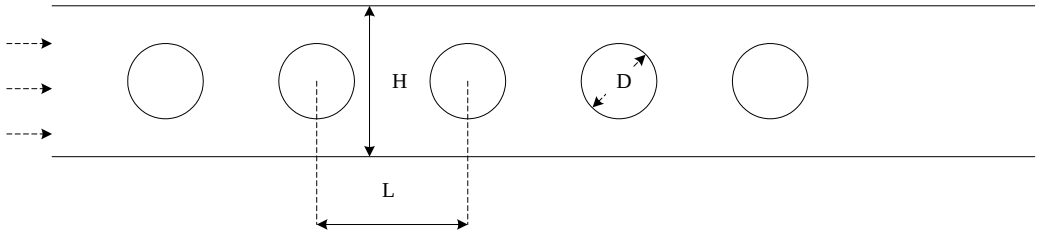

Fig. 5.10 Test problem #4: Two-dimensional flow field over a row of in-line cylinders placed between two parallel plates.

The numerical results were obtained by solving the vorticity and the streamfunction equations in the dimensionless form. Those equations were given as:

$$\frac{\partial \zeta}{\partial t} + u\frac{\partial \zeta}{\partial x} + v\frac{\partial \zeta}{\partial y} = \frac{1}{\mathrm{Re}}\left(\frac{\partial^2 \zeta}{\partial x^2} + \frac{\partial^2 \zeta}{\partial y^2}\right) \tag{5.20}$$

where ζ is the vorticity defined by the following relation:

$$\zeta = \frac{\partial v}{\partial x} - \frac{\partial u}{\partial y} \tag{5.21}$$

and the relation between the stream function ψ equation and vorticity is:

$$\frac{\partial^2 \psi}{\partial x^2} + \frac{\partial^2 \psi}{\partial y^2} = -\zeta \tag{5.22}$$

where $u = \partial\psi / \partial y$ and $v = -\partial\psi / \partial x$. Finally, the energy equation was given as:

$$u\frac{\partial \theta}{\partial x} + v\frac{\partial \theta}{\partial y} = \frac{1}{Pe}\left(\frac{\partial^2 \theta}{\partial x^2} + \frac{\partial^2 \theta}{\partial y^2}\right) \tag{5.23}$$

where Pe is the Peclet number known as $Pe = \mathrm{Re}\,\mathrm{Pr}$, and θ is the normalized temperature given as follows:

$$\theta = \frac{T - T_{in}}{T_w - T_{in}} \tag{5.24}$$

where T_w is the wall temperature of both plates and cylinders, and T_{in} is the inlet temperature.

The inlet boundary condition was assumed to be fully developed, and the velocity profile was assumed to be parabolic (v = 0). Since u and v were known at the inlet, the values of ζ and ψ can be estimated from the definition of the vorticity and the streamfunction given in the above equations. A no-slip condition was assigned at the plates and the cylinder walls. So, u and v were both zero. It was assumed that v = 0 and $\partial\zeta / \partial x = 0$ at the exit. The boundary conditions for the normalized temperatures were

$\theta = 0$ at the entrance, $\theta = 1$ on the surface of both plates and cylinder walls, and $\partial\theta / \partial x = 0$ at the exit.

The numerical solution of the governing equation was carried out in the transformed plane on a rectangular field with a rectangular mesh. Transformed grid equations were discretized using central differencing and the resulting equations were solved by the successive over-relaxation method (SOR). A grid size of 233x31 was used to study flow and heat transfer over a five cylinder array. The distribution of the grid points was not uniform in the physical domain, however, the computational domain was maintained with a uniform rectangular grid. For further information the reader may refer to Kundu et al. (1991a).

The main purpose of their research was to study the effect of different aspect ratios and Reynolds numbers on the pressure drop and heat transfer rate as they play an important role in designing heat exchangers. The entire domain was divided into several Heat Exchanger Modules (HEMs). Each HEM contains one cylinder and bound by two fictitious surfaces located at the mid section between two consecutive cylinders. Except for the first and the last HEM, the pressure drop and Nusselt number across a HEM are almost constant for any specified Re.

Fig. 5.11 provides the results of the dimensionless pressure difference ($\Delta P^* = \Delta P / \rho U_b^2$) for the third HEM as a function of the Reynolds number when *L/D* = 3 and *H/D* = 2. Both numerical (Kundu et al. 1991a) and experimental (Kundu 1989) data were presented and compared with the results generated from the developed code.

Notice that there is good agreement between the pressure data as they monotonically decrease with the increase in Reynolds number.

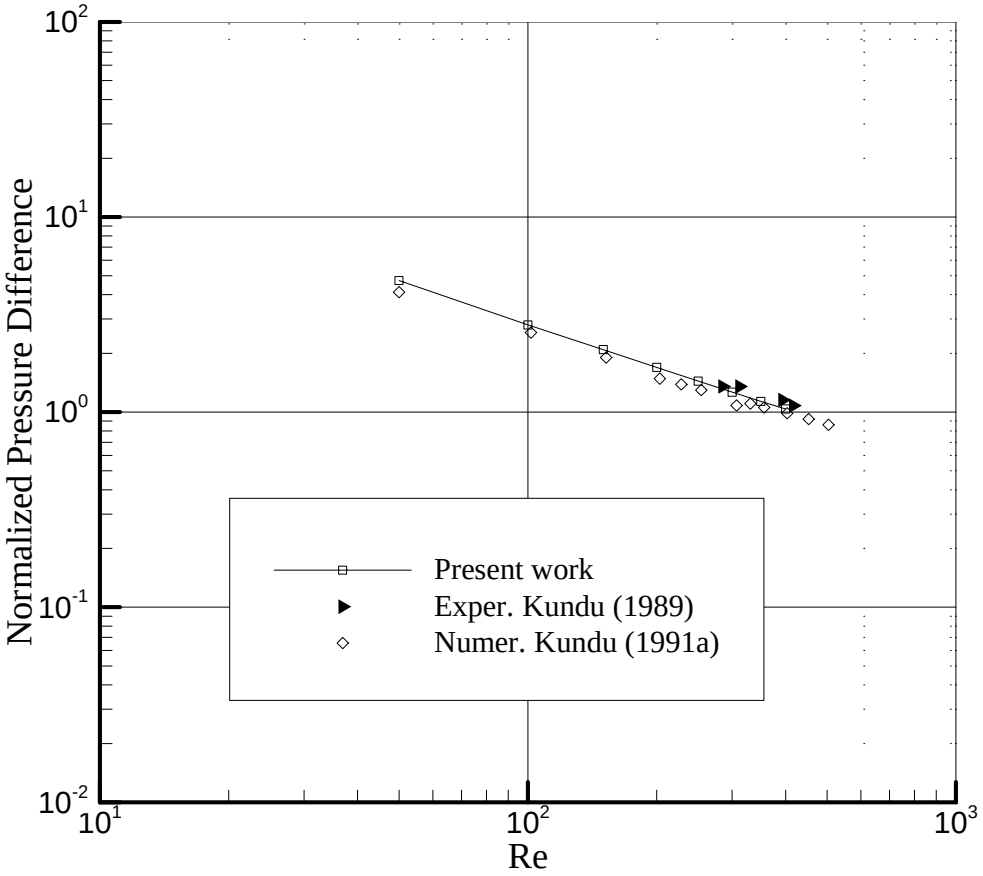

Fig. 5.11 Normalized pressure difference across the third HEM.

The average heat transfer coefficient and the corresponding Nusselt number across the HEMs were also computed and studied. The computed enthalpy between the

HEMs was integrated to calculate the normalized bulk temperature $\theta_{b,i}$ at the inlet and exit of each HEM. The heat flow Q_i for each HEM was computed by calculating the local heat flux and integrating the results over all the surfaces of the HEM. The average heat transfer coefficient $\bar{h}$ was introduced so that

$$Q_i = \dot{m} c_P (\theta_{b,i} - \theta_{b,i-1}) = \bar{h}(1 - \theta_{m,i})(2A_P + A_i) \tag{5.25}$$

where the subscript *i* represents the module number, A is the area of the circular cylinder, A_P is the area of the plate and $\theta_{m,i}$ is the average of the normalized bulk temperatures at the inlet and exit of each HEM defined as:

$$\theta_{m,i} = 0.5(\theta_{b,i} + \theta_{b,i-1}) \tag{5.26}$$

Table 5.2 shows the heat transfer rate that is summarized by the Nusselt number (*Nu*). The Nusselt number is defined earlier in Equation (5.14) and the hydraulic diameter D_H is defined as the channel height (*H*). The geometric parameter values were *L/D* = 3 and *H/D* = 2 for the cases considered for validation. It is evident from Table 5.2 that the numerical predictions of heat transfer using the developed code agrees well with the numerical predictions of Kundu et al. (1991).

TABLE 5.2 Average Nusselt number for *L/D* = 3 and *H/D* = 2.

Re = 50	2nd HEM	3rd HEM	4th HEM
Kundu (1991a)	9.4	9.4	9.8
Present work	9.228	9.229	9.229

Re = 200	2nd HEM	3rd HEM	4th HEM
Kundu (1991a)	12.5	12.6	12.8
Present work	12.44	12.43	12.42

This scheme was applied to several two-dimensional incompressible fluid flow and heat transfer situations. The numerical results have been compared with the analytical solutions, numerical, or experimental results whenever available in literature. On the basis of the results presented earlier, it can be concluded that the validation task has been accomplished. Although the test problems discussed in this chapter do not cover the entire range of possible fluid flow and heat transfer cases, a strong confidence to apply the developed code to study heat and momentum transfer over a bank of flat tubes is established. The study of fluid flow and heat transfer over a flat tube bank will be discussed in the following chapter.

CHAPTER VI

RESULTS AND DISCUSSION

The test problems solved in the previous chapter serve the useful purpose of validation and evaluation of the formulation given earlier in Chapter IV. To this end, having sufficiently proven the accuracy and reliability of the formulation, it is time to demonstrate its potential for solving, the problem mentioned in the objective earlier in Chapter I, the flow field and heat transfer over a bank of flat tubes.

6.1 Geometry Configuration

Fluid flow and heat transfer over a bank (bundle) of tubes in cross flow is relevant to numerous industrial applications, such as steam generation in a boiler or air cooling in the coil of an air conditioner. The two-dimensional geometric configuration is shown in Fig. 6.1. The tube rows of a bank are either aligned (in-line) or staggered in the direction of the fluid velocity. The configuration is characterized by the transverse pitch S_T and the longitudinal pitch S_L measured between the tube centers.

Fig. 6.2 shows an enlarged view of two rows of an in-line flat tube bank that illustrates the domain of interest. The rows in the flow geometry are assumed to be of infinite extent in the direction perpendicular to the paper so that the flow pattern can be considered as two-dimensional. Therefore, the computational domain is limited to the

one shown in Fig. 6.2 by the dashed lines. The longitudinal tube diameters *Db* is twice the length of a circular cylinder with diameter *Da*. The height *H* is equivalent to the transverse distance between two rows or the height of one module and *L* is the longitudinal distance between the tube centers of two successive cylinders or the length of one module.

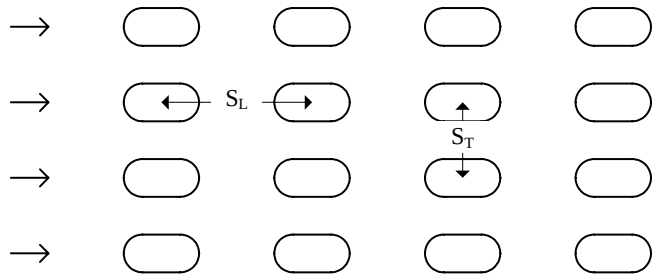

(a) In-line position of flat tube banks.

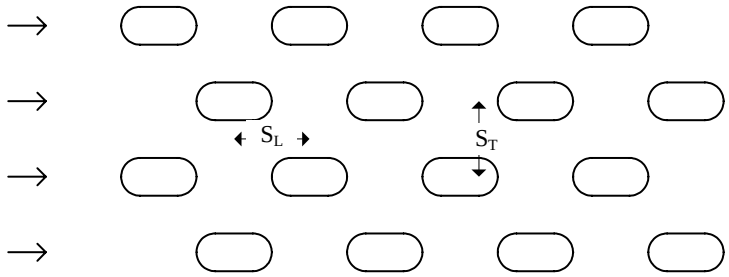

(b) Staggered position of flat tube banks.

Fig. 6.1 Flat tube banks: (a) In-line and (b) Staggered arrangements.

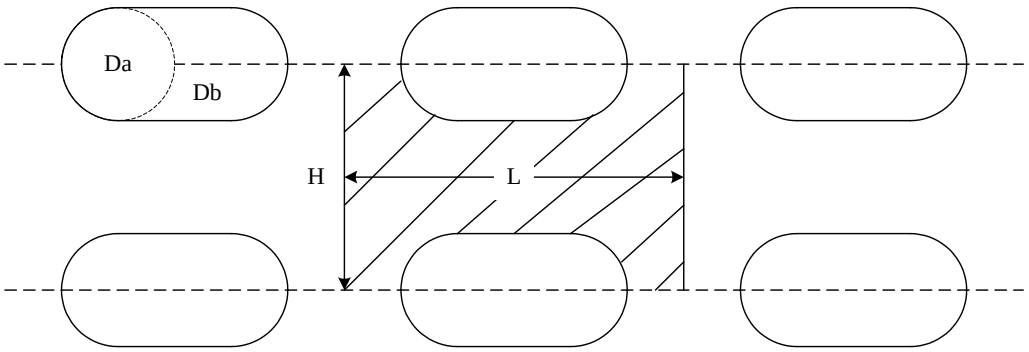

Fig. 6.2 Enlarged view of two rows of in-line position of flat tube banks.

The main purpose of this work is to study the effect of different aspect ratios and Reynolds numbers of different fluids on pressure drop and heat transfer. Thus, four main configurations are studied. All these configurations are considered with different values of *H/Da* and *L/Da*. Therefore, nine in-line positions and nine staggered position designs are studied. Then, five different values of Re are applied for each of the two different values of Prandlt number. The four main configurations for one single module are shown in Fig. 6.3. The values of *H/Da* and *L/Da* will be given in a later section of this chapter. Each case is studied for Re = 25, 50, 100, 200, and 400 and for Pr = 0.7 and 7.0 (i.e., air and water) to finish with a total of 180 cases. The Re is defined as:

$$\mathrm{Re} = \frac{u_b D_H}{\nu} \tag{6.1}$$

where D_H is taken to be twice the height H.

The value *L/Da* for the module of an in-line configuration is taken to be 4 as shown in Fig. 6.3a. The other three configurations are all staggered in position and the *L/Da* values are 7, 6, and 5 as shown in Figs. 6.3b, c, and d, respectively. Although half of the domain of the in-line position can be studied because of symmetry, the entire domain is studied to make sure that the results are symmetric.

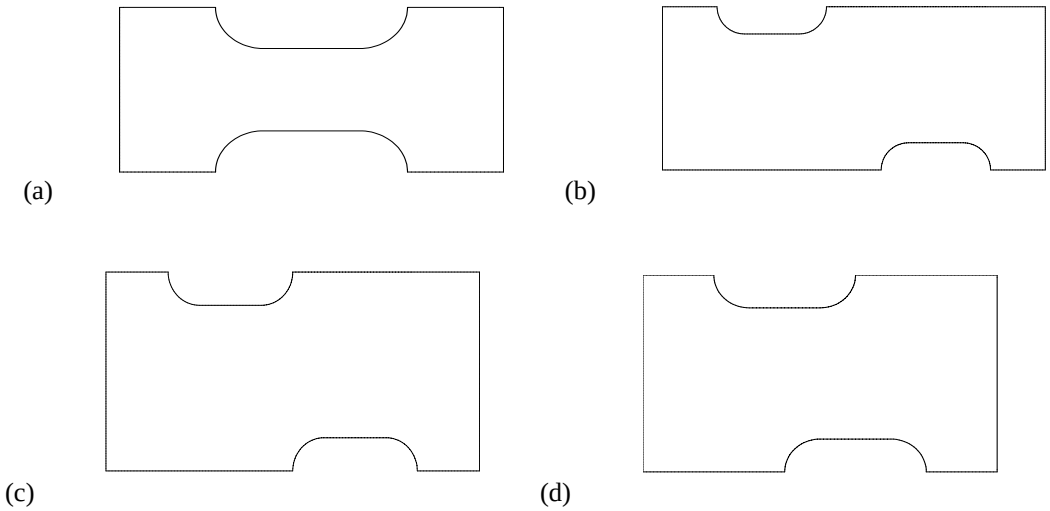

Fig. 6.3 The main configurations for one module of (a) in-line L*4, (b) staggered L*7, (c) staggered L*6, (d) staggered L*5.

6.2 Grid Configuration

In the development of the numerical procedure, the first step is to determine a grid distribution over the flow domain. In each configuration, the domain needs to be discretized into a structured grid by using one of the grid generation techniques. However, the Geometry And Mesh Building Intelligent Toolkit (GAMBIT) has been used for this task to handle the arbitrary shaped domain by which a body-fitted

coordinate system was generated and the irregular physical domain was discretized into numerous square volumes. The resulting grid distribution for one module of in-line configuration is illustrated in Fig. 6.4.

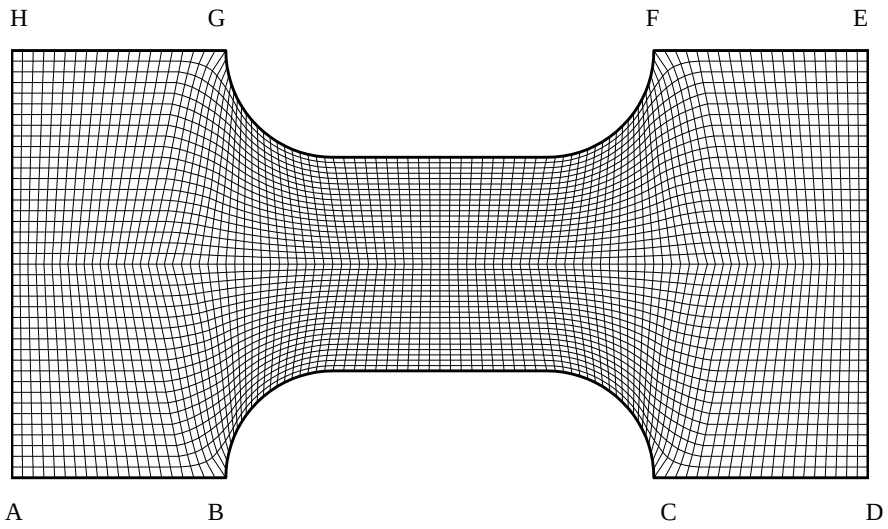

Fig. 6.4 Grid distribution for one in-line configuration module.

The computational domain was divided into three individual regions. These regions are the entry region, the flat tube modules and the exit region. A uniform orthogonal grid was used for both entry and exit regions. The grid distribution shown above (Fig. 6.4) can be repeated successively to generate the domain of flat tube modules. In this study, six consecutive flat tubes are included in the computational domain.

In Fig. 6.4, the surfaces BC and FG are the top wall of the bottom tube and the bottom wall of the top tube, respectively. A no-slip boundary condition was assigned for these two surfaces. The lines AB, CD, EF, and GH are lines of symmetry where no flow crosses these boundaries and the normal component of velocities and the normal gradient of the parallel component of velocity are set to zero. Finally, the lines AH and DE are recognized as the module inlet and module outlet, respectively.

6.3 Grid Independence Test

A grid refinement study (i.e., grid independence test) was performed in order to assess the accuracy of the results presented. The following parameters were considered in the grid independence test; $Db/Da = 2$, $H/Da = 4$, $L/Da = 4$ and Pr = 0.7 at the highest Reynolds number Re = 400 for the in-line configuration. The grid independence test was done for several grid sizes per module. These grids are 101x101, 101x121, 126x121, 126x151, and 151x151 per module for ten modules, in addition to the uniform grid points in the entry and exit regions. The one with the smaller number of grid points (101x101) was chosen throughout this study in order to save time and computational effort.

A summary of the grid independence study is presented in Tables 6.1 and 6.2. Establishing the grid independence test provides strong evidence of the reliability of the present method. In the following section, results of the parametric runs based on the grid independent solution will be presented.

TABLE 6.1 The results for various grids of friction factor.

Module	Grid 1 (101x101)	Grid 2 (101x121)	Percentage Difference	Grid 3 (126x121)	Percentage Difference	Grid 4 (126x151)	Percentage Difference	Grid 5 (151x151)	Percentage Difference
1	0.727	0.725	0.203	0.727	0.167	0.729	0.367	0.728	0.109
2	0.233	0.232	0.468	0.234	0.960	0.235	0.198	0.236	0.503
3	0.202	0.201	0.389	0.203	0.840	0.203	0.062	0.204	0.463
4	0.180	0.179	0.368	0.180	0.780	0.180	0.024	0.181	0.487
5	0.167	0.166	0.386	0.167	0.752	0.167	0.021	0.168	0.498
6	0.159	0.158	0.424	0.159	0.746	0.159	0.043	0.160	0.446
7	0.154	0.153	0.441	0.154	0.723	0.154	0.076	0.155	0.321
8	0.151	0.150	0.419	0.151	0.667	0.151	0.104	0.152	0.175
9	0.149	0.148	0.381	0.149	0.602	0.149	0.115	0.150	0.085
10	0.137	0.136	0.465	0.137	0.740	0.137	0.186	0.138	0.128

TABLE 6.2 The results for various grids of average mean Nusselt number.

Module	Grid 1 (101x101)	Grid 2 (101x121)	Percentage Difference	Grid 3 (126x121)	Percentage Difference	Grid 4 (126x151)	Percentage Difference	Grid 5 (151x151)	Percentage Difference
1	27.925	27.866	0.213	27.793	0.261	27.717	0.273	27.682	0.129
2	16.141	16.120	0.130	16.098	0.136	16.064	0.213	16.062	0.012
3	14.499	14.483	0.110	14.446	0.258	14.415	0.217	14.402	0.090
4	13.670	13.657	0.096	13.619	0.282	13.593	0.191	13.576	0.121
5	13.270	13.256	0.105	13.221	0.265	13.197	0.184	13.179	0.138
6	13.074	13.059	0.115	13.027	0.239	13.001	0.201	12.985	0.127
7	12.978	12.962	0.121	12.931	0.236	12.906	0.200	12.890	0.125
8	12.932	12.917	0.118	12.886	0.240	12.860	0.200	12.843	0.131
9	12.910	12.896	0.110	12.864	0.250	12.838	0.201	12.821	0.134
10	12.720	12.706	0.109	12.688	0.148	12.662	0.202	12.652	0.075

Percentage Difference = |(Grid (I) – Grid (I+1))/Grid (I+1)|*100

6.4 Post-Processing of Calculations

Prior to the discussion of results, selected dimensionless groups of heat and mass transfer need to be introduced. Once the converged solution for velocities, pressure and temperature fields are found, the calculations for these dimensionless numbers are carried out.

6.4.1 Calculation of Streamlines

The values of the streamlines can be computed from the streamfunction which is based on the velocity field as follows:

$$\psi_{x,y} = \psi_{x,y=0} - \int_0^y u dy \tag{6.2}$$

the term, $\psi_{x,y=0}$, is an arbitrary value and can be set to zero. Since a non-dimensional form is more appropriate to be presented, the non-dimensionalized streamfunction, ψ^*, should be introduced as follows:

$$\psi^* = \frac{\psi}{HU_o} \tag{6.3}$$

where *H* is the height of one module as shown in Fig. 6.2 and *Uo* is the uniform inlet velocity. The non-dimensional streamfunction was defined to be 0 and 1 at *Y/H* = 0 and 1, respectively. However, some computed values of ψ^* were found to be lower than zero right behind the lower tubes and higher than the ones behind the upper tubes.

6.4.2 Calculation of Dimensionless Pressure Drop

The dimensionless pressure drop per module length is normalized by dividing the pressure difference by dynamic pressure as follows:

$$\Delta P^* = \frac{P_m(MI) - P_m(MO)}{\rho u_b^2} \tag{6.4}$$

where the subscript *b* stands for bulk value while, MI and MO stand for module inlet and outlet, respectively. The bulk velocity can be calculated as follows:

$$u_b = \frac{\int_0^H u dy}{\int_0^H dy} \tag{6.5}$$

similarly, the mean pressure at a given cross-stream location can be calculated as follows:

$$P_m = \frac{\int_0^H P dy}{\int_0^H dy} \tag{6.6}$$

6.4.3 Calculation of Isotherms

A non-dimensional temperature is introduced for the disscusion of the temperature field as follows:

$$\theta(x) = \frac{T(x) - T_t}{T_b(x) - T_t} \tag{6.7}$$

where T_t is the tube temperature, and T_b is the bulk temperature defined by:

$$T_b(x) = \frac{\int_H T(x)\vec{V}\cdot\vec{n}dy}{\int_H \vec{V}\cdot\vec{n}dy} \tag{6.8}$$

6.4.4 Calculation of Module Average Nusselt Number

The heat transfer rate per module is summarized by the Nusselt number, which is defined as:

$$Nu_i = \frac{\bar{h}_i D_H}{k} \tag{6.9}$$

where D_H is the hydraulic diameter, defined as twice the height (H). The module average heat transfer coefficient $\bar{h}_i$, is given as:

$$\bar{h}_i = \frac{Q_i}{(T_{b,m} - T_t)(A_t)} \tag{6.10}$$

where A_t is the area of the tube interface with the flow, $T_{b,m}$ is the average of the module inlet and outlet bulk temperatures, and Q_i being the total heat flux gained by the fluid in a module, and defined as follows:

$$Q_i = \dot{m}C_P\left(T_b(MI) - T_b(MO)\right) \tag{6.11}$$

6.5 Discussion of Results

The governing independent parameters influencing the fluid flow and heat transfer over a bank of flat tubes are the Reynolds number (Re), Prandlt number (Pr), height ratio (*H/Da*), length ratio (*L/Da*), the aspect ratio of the tube (*Db/Da*), and the configuration or the positioning of the tubes (i.e., in-line or staggered). Table 6.3 shows all configurations considered in this study. Each case is assigned with a different name and studied for a different combination of the following values of Reynolds number (Re = 25, 50, 100, 200, and 400) and two different fluids (i.e., air or water) represented by Prandlt number (Pr = 0.7 and 7.0).

TABLE 6.3 In-line and staggered configurations considered in this study.

Configurations	H/Da	L/Da	Configurations	H/Da	L/Da
In-line H*2-L*4	2	4	Stagg. H*2-L*5	2	5
In-line H*2-L*5	2	5	Stagg. H*2-L*6	2	6
In-line H*2-L*6	2	6	Stagg. H*2-L*7	2	7
In-line H*3-L*4	3	4	Stagg. H*3-L*5	3	5
In-line H*3-L*5	3	5	Stagg. H*3-L*6	3	6
In-line H*3-L*6	3	6	Stagg. H*3-L*7	3	7
In-line H*4-L*4	4	4	Stagg. H*4-L*5	4	5
In-line H*4-L*5	4	5	Stagg. H*4-L*6	4	6
In-line H*4-L*6	4	6	Stagg. H*4-L*7	4	7

Although 180 different parametric runs were made, only representative results are presented in this thesis. The effect of each parameter on the velocity profile, streamline, and normalized temperature field will be discussed separately in the following sections.

6.5.1 Velocity Profile

Fig. 6.5 shows the streamwise developing velocity profiles along the exit of each module. The velocity distribution is normalized by the value of the uniform inlet velocity *Uo* and given as a function of *Y/H*, for *H/Da* = 2 and *L/Da* = 4 for five different values of Reynolds number for an in-line arrangement. It can be established that as the Reynolds number increases, the maximum velocity in the passage increases while, the negative velocity downstream, right behind the tubes, increases in magnitude to satisfy continuity.

The velocity profile is nearly symmetric and repeats itself for other modules except the first and the last. The flow is not fully developed in the first module. Its profile is similar to other modules at low values of Reynolds number. At the exit of the last module, the velocity profile is slightly different due to the absence of additional tubes downstream. The symmetric condition is no longer applicable as the staggered arrangement comes into consideration. The velocity profile that can be seen in Fig. 6.6 – 6.8 are for different spacing between the upper and lower tubes as given earlier in Fig. 6.2.

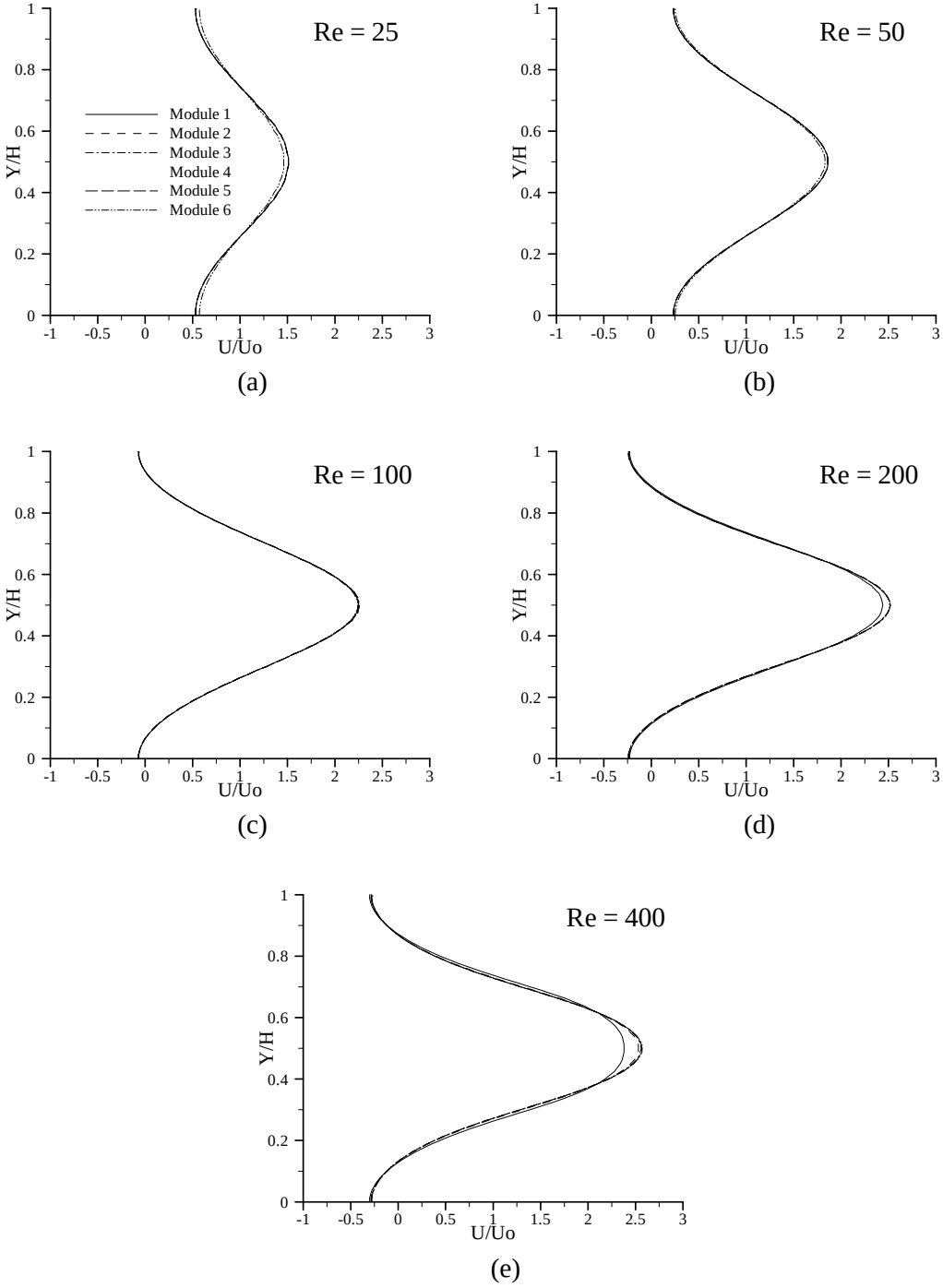

Fig. 6.5 Effect of Reynolds number on the developing velocity profiles along the transverse direction of each module outlet (MO) for an in-line arrangement, *H/Da* = 2 and *L/Da* = 4: (a) Re =25, (b) Re =50, (c) Re =100, (d) Re =200, and (e) Re =400.

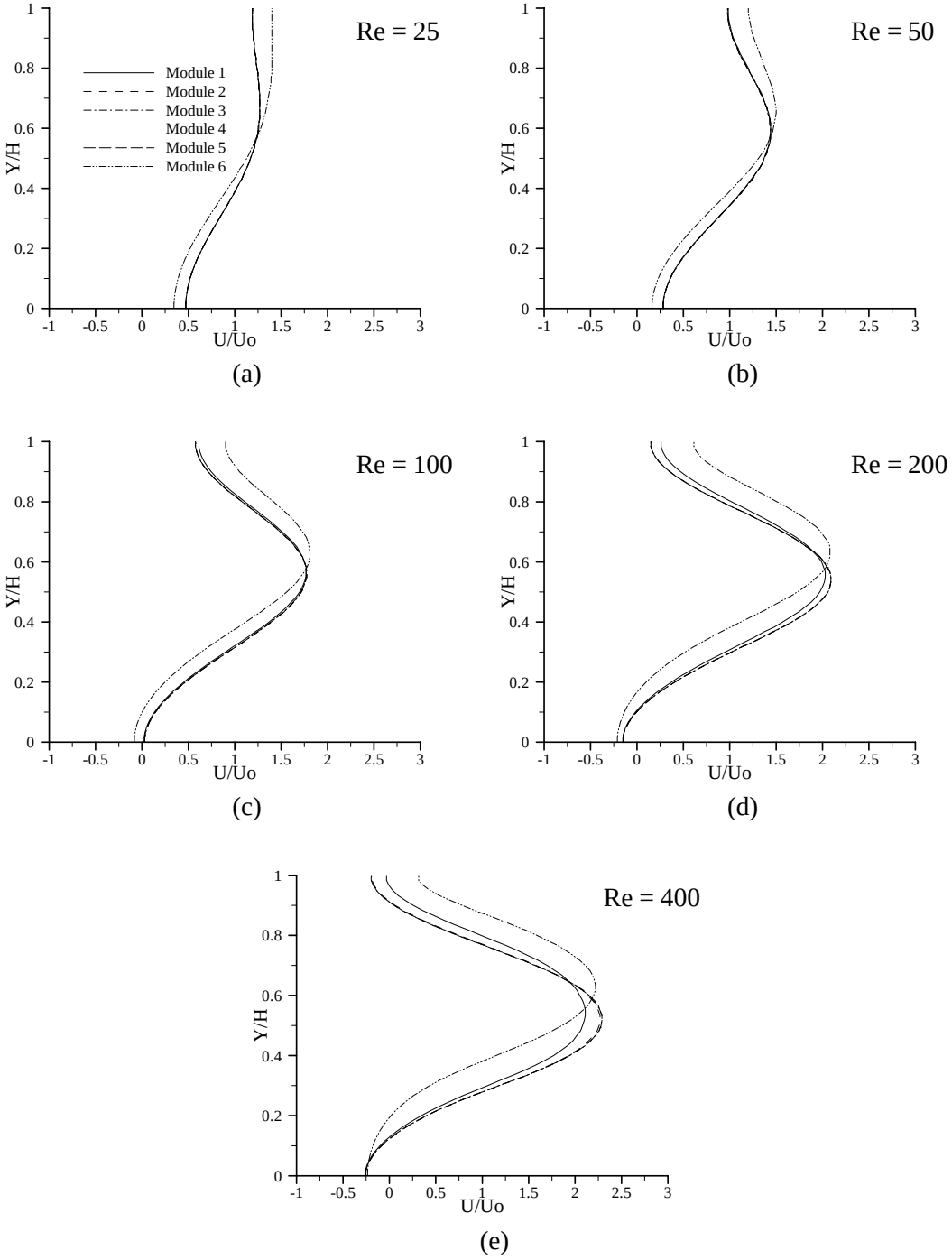

Fig. 6.6 Effect of Reynolds number on the developing velocity profiles along the transverse direction of each module outlet (MO) of a staggered arrangement, *H/Da* = 2 and *L/Da* = 5: (a) Re =25, (b) Re =50, (c) Re =100, (d) Re =200, and (e) Re =400.

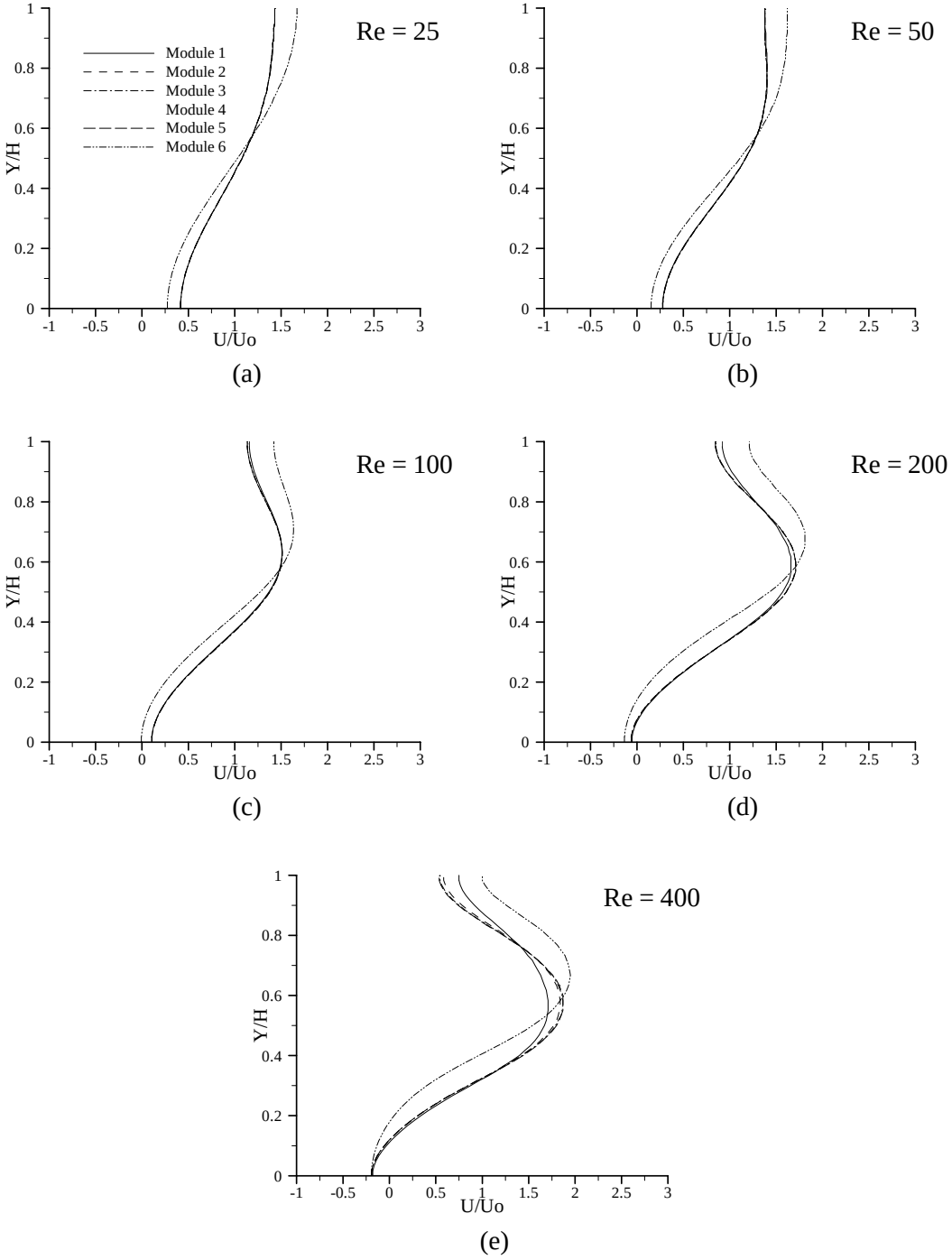

Fig. 6.7 Effect of Reynolds number on the developing velocity profiles along the transverse direction of each module outlet (MO) of a staggered arrangement, *H/Da* = 2 and *L/Da* = 6: (a) Re =25, (b) Re =50, (c) Re =100, (d) Re =200, and (e) Re =400.

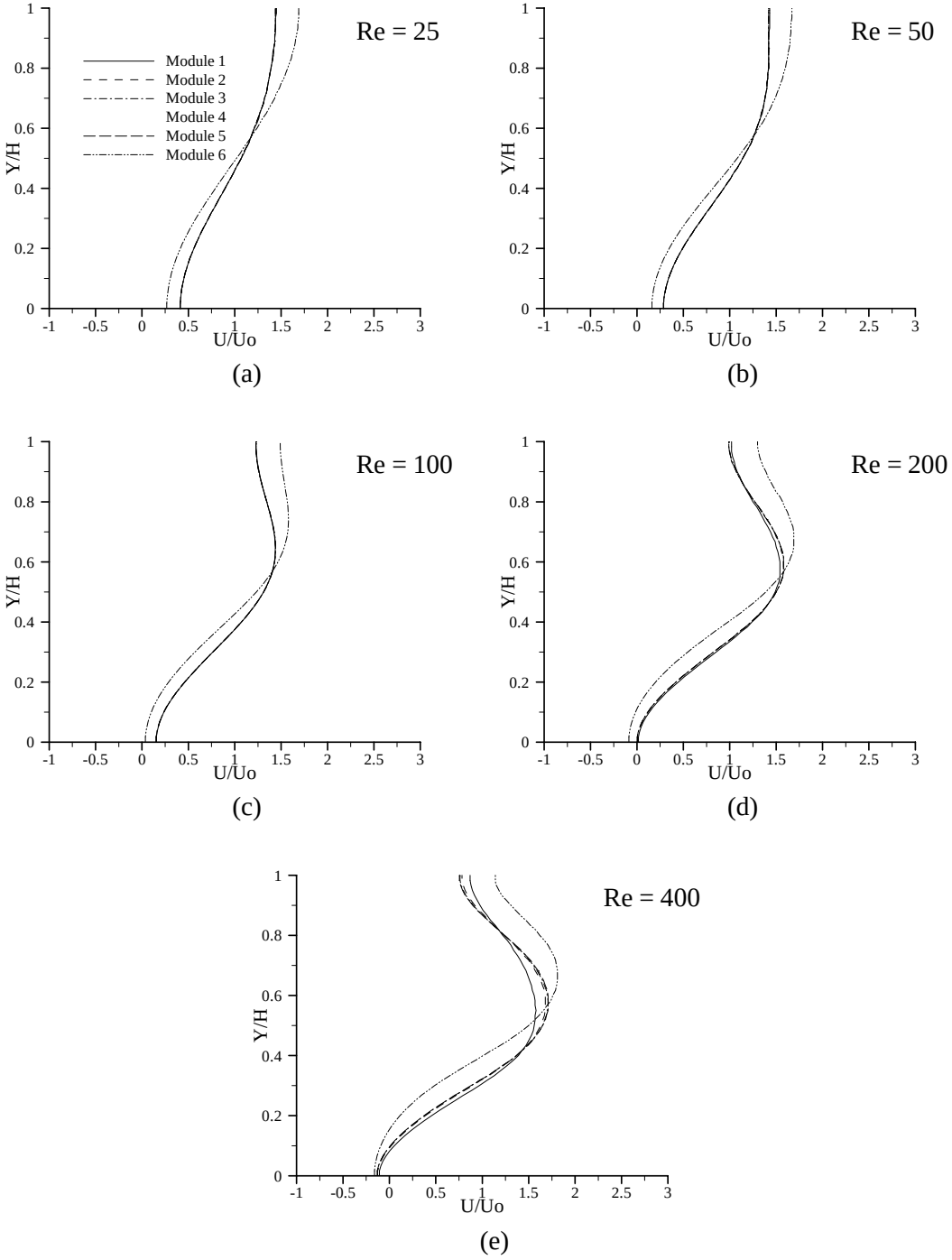

Fig. 6.8 Effect of Reynolds number on the developing velocity profiles along the transverse direction of each module outlet (MO) of a staggered arrangement, *H/Da* = 2 and *L/Da* = 7: (a) Re =25, (b) Re =50, (c) Re =100, (d) Re =200, and (e) Re =400.

The changes in results are more noticeable for the inner four modules with the first and the last especially at higher values of Reynolds numbers (Re = 200 and 400). It has to be noted that the location of maximum velocity has been shifted slightly to the top due to the absence of an obstacle (i.e., flat tube) at the top. As the longitudinal spacing (S_L) between the upper and lower tubes decrease the velocity tends to have higher values at the location of the maximum velocities as well as the negative velocity due to small tube spacing. This can be noticed by comparing Fig. 6.6e, 6.7e, and 6.8e with each other.

Comparison of Fig. 6.5 with Figs. 6.9 and 6.10 shows the most noticeable changes in velocity profiles. These changes are due to the increase in the height ratio. The maximum velocity in the middle of (*Y/H*) the passage considerably decreases because of a larger flow area. The negative velocity in magnitude, downstream right behind the tube, increases as the height ratio decreases. Furthermore, the periodically fully developed profile can be reached in upstream modules as the height ratio decreases. For instance, when Re = 400 at *H/Da* = 2 the flow attains a periodically fully developed profile downstream of the second module as illustrated in Fig. 6.5e. However, at the same Re with *H/Da* = 3 or 4 the flow attains a periodically fully developed profile downstream of the fourth module as illustrated in Figs. 6.9e and 6.10e.

Figs. 6.11 and 6.12 show the velocity profiles for higher length ratios i.e., *L/Da* = 5 and 6, respectively, which can be compared with Fig. 6.5. The maximum velocity decreases slightly as the length ratio increases. For this case, the most changes occur at the lowest value of Re. The velocity profile flattens as the length ratio increases. This is because the flow has enough length to recover to the condition of uniform inlet

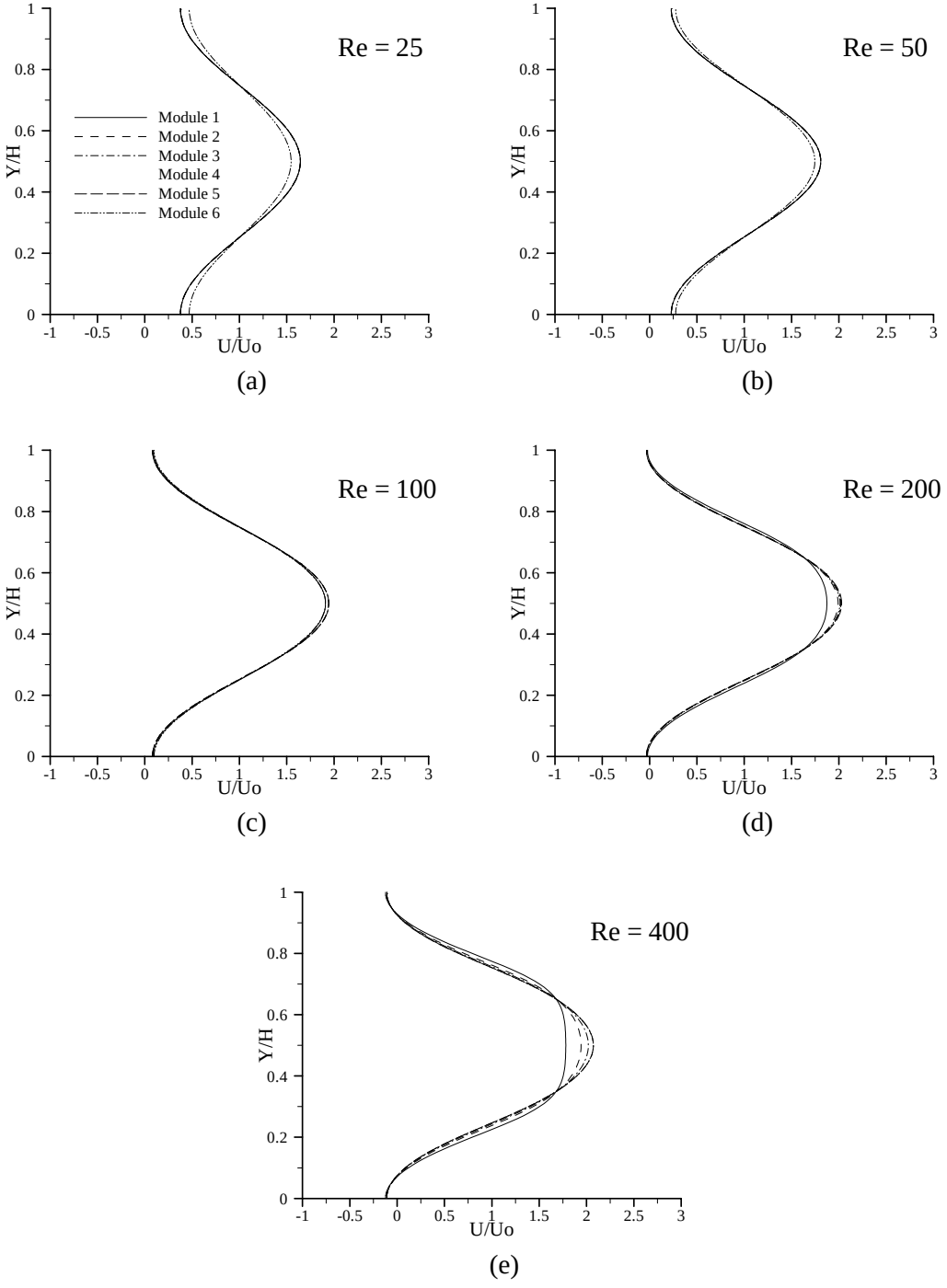

Fig. 6.9 Effect of Reynolds number on the developing velocity profiles along the transverse direction of each module outlet (MO) for an in-line arrangement, *H/Da* = 3 and *L/Da* = 4: (a) Re =25, (b) Re =50, (c) Re =100, (d) Re =200, and (e) Re =400.

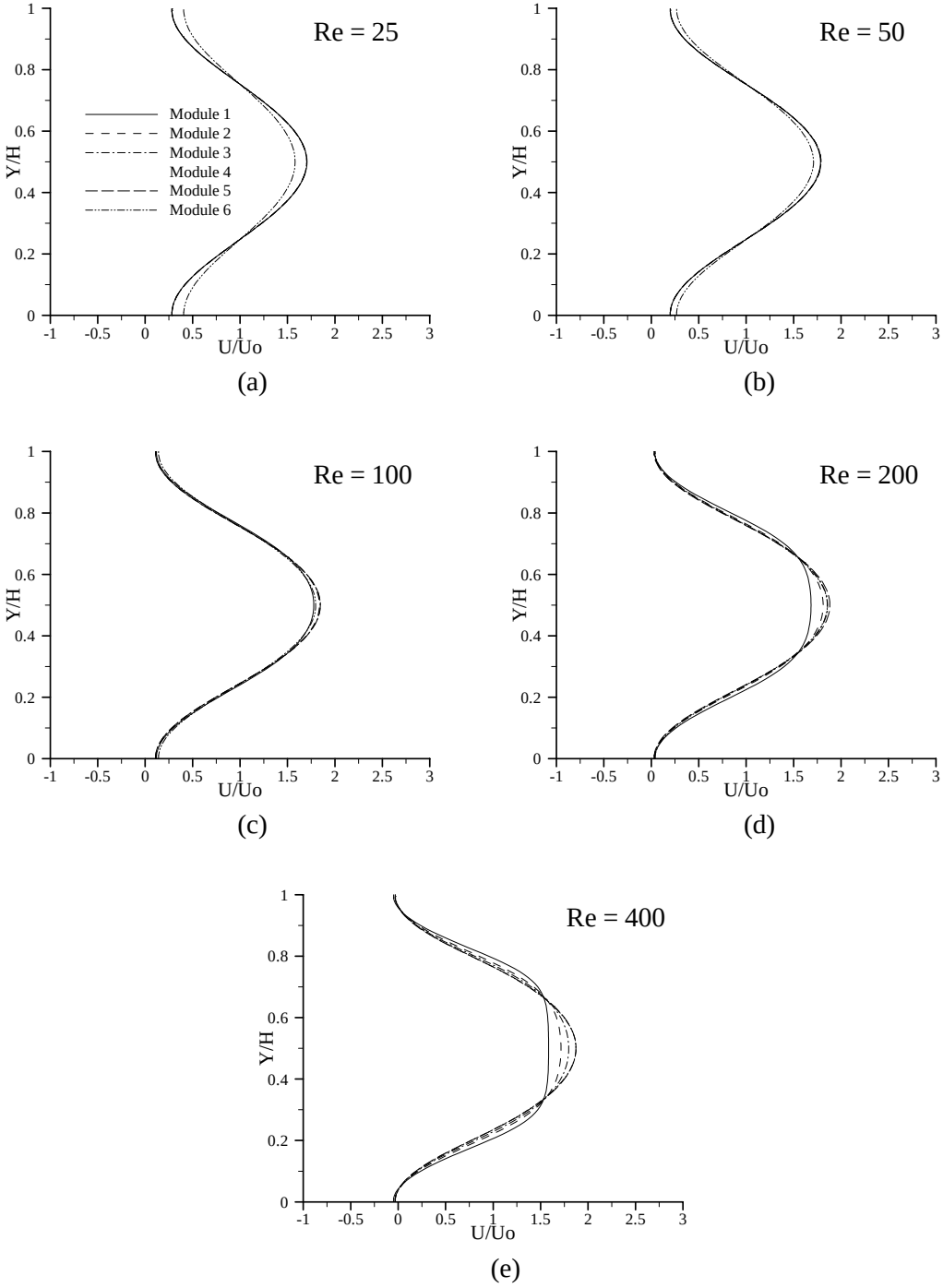

Fig. 6.10 Effect of Reynolds number on the developing velocity profiles along the transverse direction of each module outlet (MO) for an in-line arrangement, *H/Da* = 4 and *L/Da* = 4: (a) Re =25, (b) Re =50, (c) Re =100, (d) Re =200, and (e) Re =400.

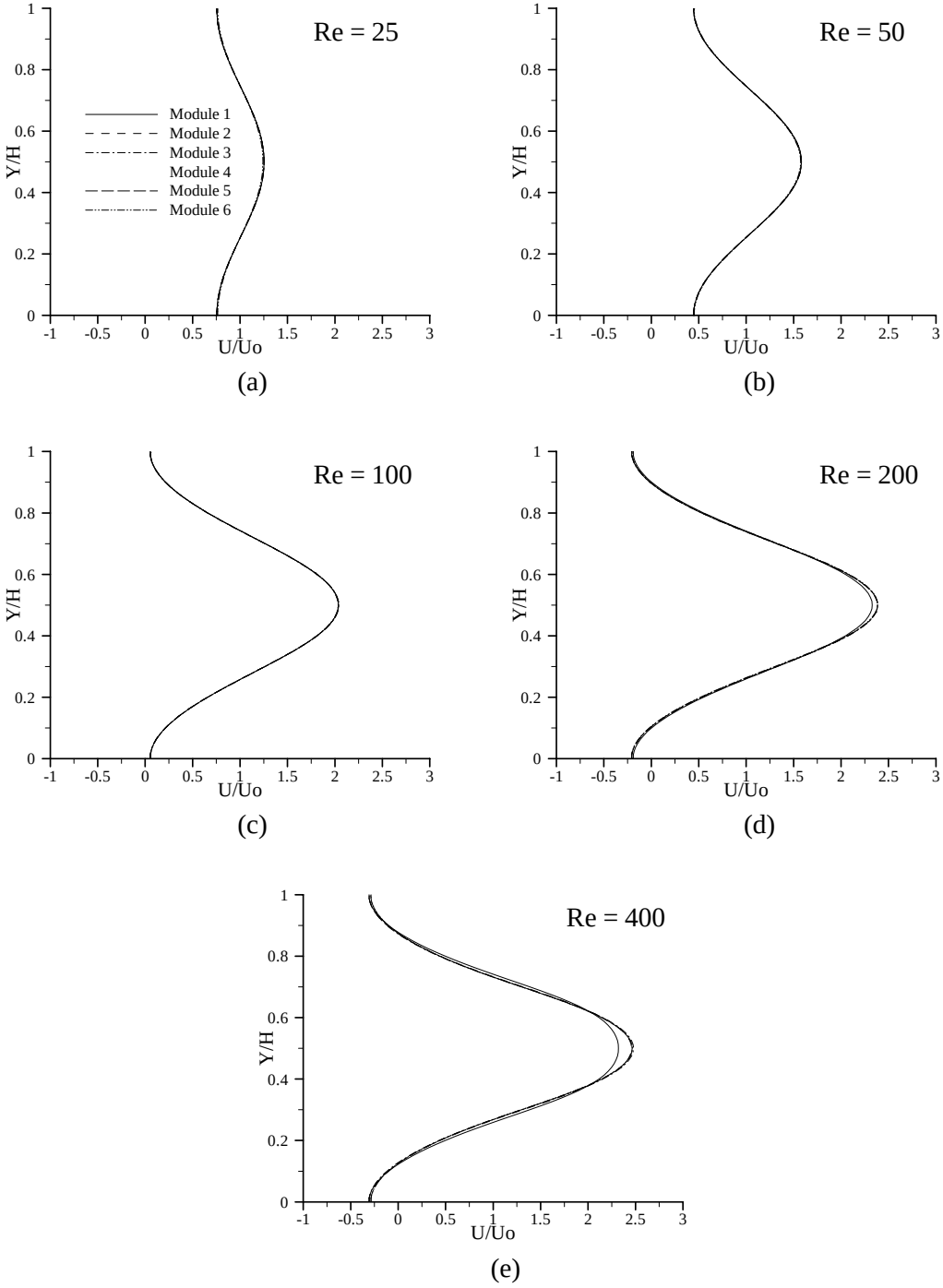

Fig. 6.11 Effect of Reynolds number on the developing velocity profiles along the transverse direction of each module outlet (MO) for an in-line arrangement, *H/Da* = 2 and *L/Da* = 5: (a) Re =25, (b) Re =50, (c) Re =100, (d) Re =200, and (e) Re =400.

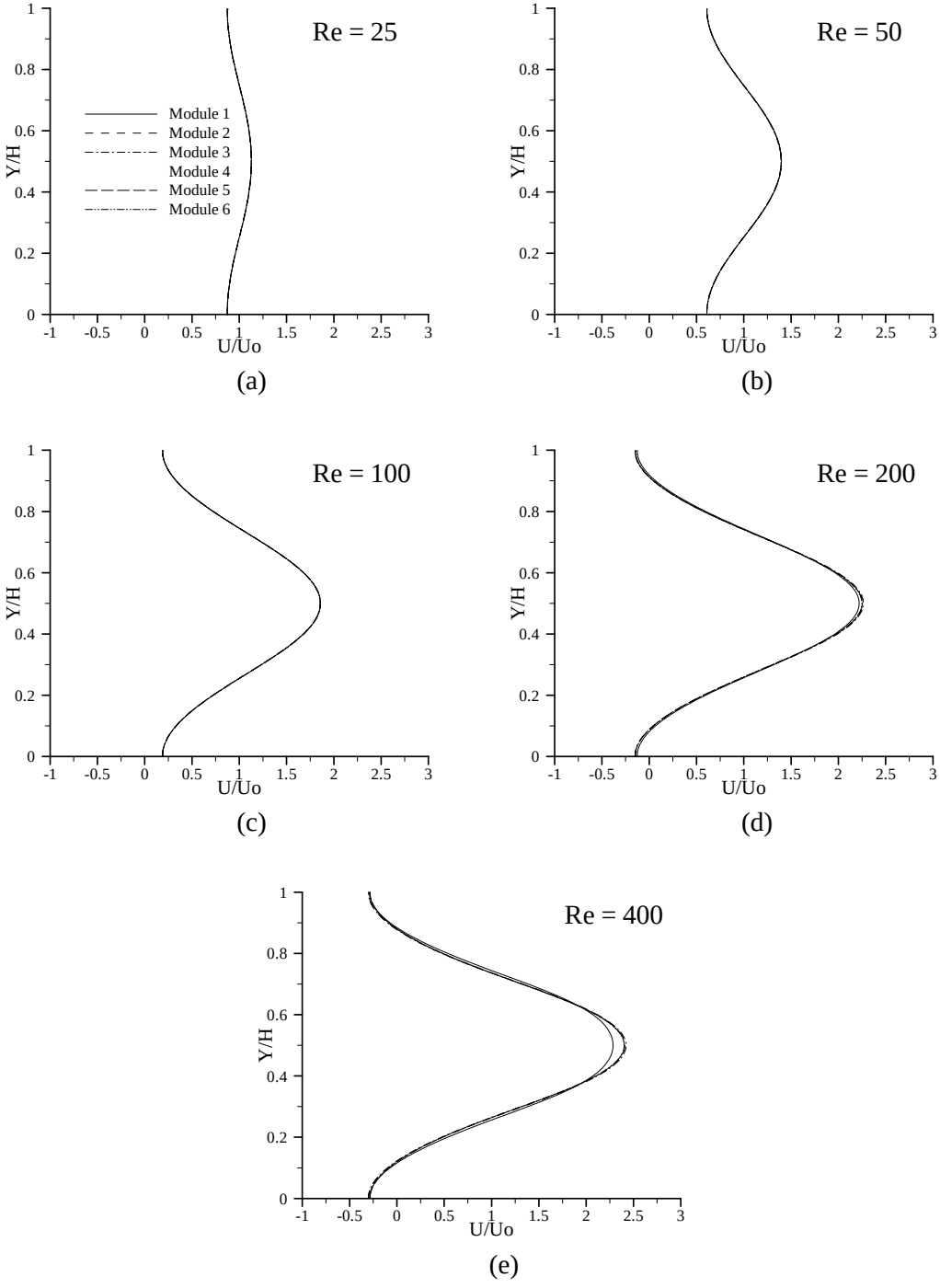

Fig. 6.12 Effect of Reynolds number on the developing velocity profiles along the transverse direction of each module outlet (MO) for an in-line arrangement, *H/Da* = 2 and *L/Da* = 6: (a) Re =25, (b) Re =50, (c) Re =100, (d) Re =200, and (e) Re =400.

velocity profile before being interrupted with the presence of the next tube module. This behavior is evident in Figs. 6.5a, 6.11a, and 6.12a. For higher length ratios, all cases attain periodically fully developed flow profile downstream of the first module.

6.5.2 Streamlines

As can be seen from the velocity profiles given in the earlier subsection, most of the cases attain periodically fully developed profiles downstream of the first module (fourth in some cases). Thus, discussion of the fourth module will be enough to show most of the details needed for examining the streamlines instead of showing the entire domain with dense repeated information. Fig. 6.13 shows the effect of Reynolds number on the non-dimensional stream function for the fourth module for an in-line arrangement, when $H/Da = 2$ and $L/Da = 4$.

Table 6.4 lists the minimum and maximum values of the non-dimensional stream function corresponding to Fig. 6.13. A close examination of Fig. 6.13 and Table 6.4 would disclose certain distinct characteristics. Flow separation can hardly be detected when Reynolds number as low as 25. As Reynolds number increase, the separated flow covers a smaller portion of the domain until it completely covers the area between two consecutive tubes at higher Reynolds number. In fact, the entire area between two consecutive tubes is occupied by recirculation at Re = 200 and 400, though the center of the recirculation is shifted slightly to the right closer to the next tube at Re = 400. This significant difference is a result of a higher flow speed which pushes the recirculation downstream a bit.

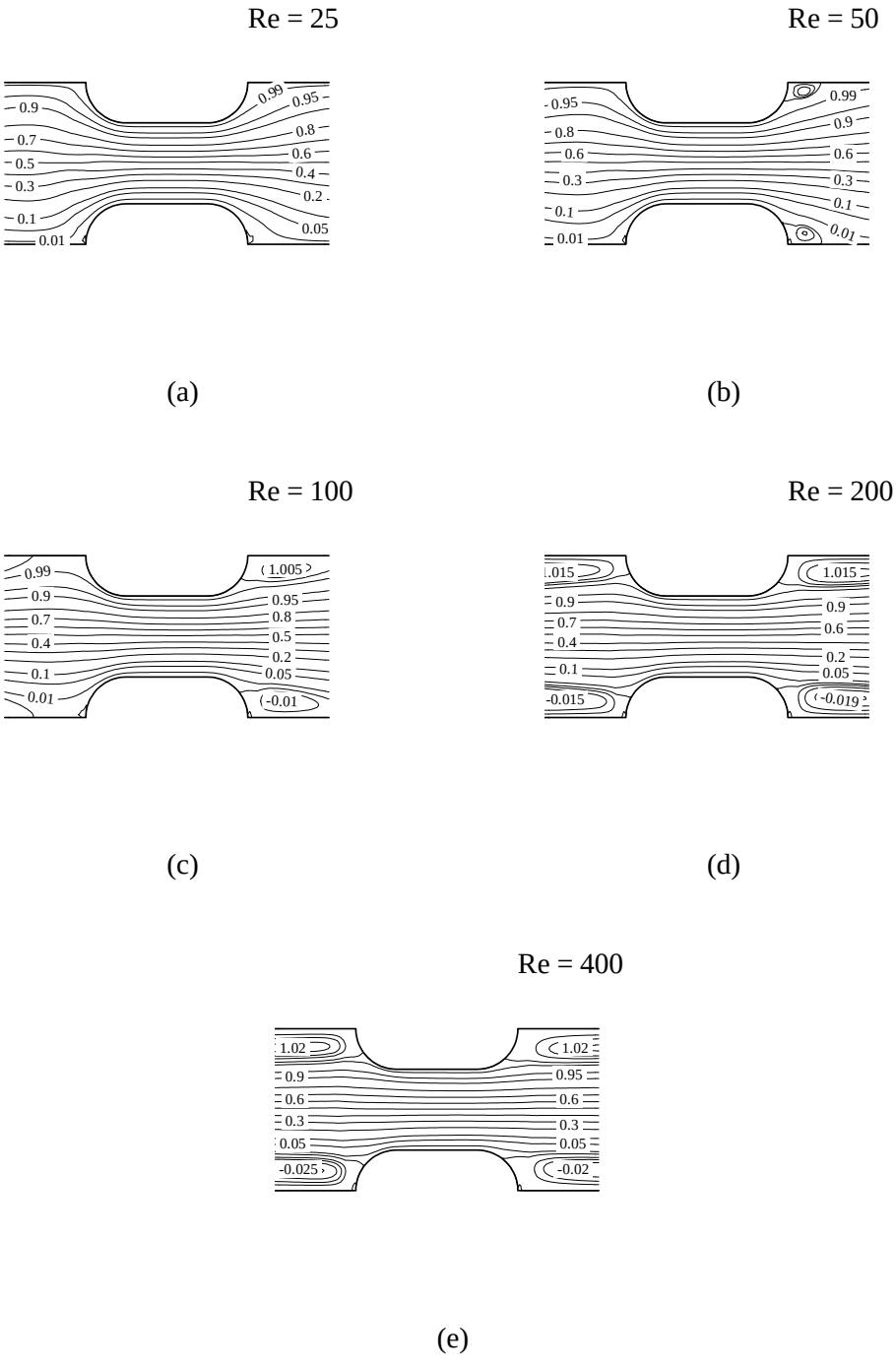

Fig. 6.13 Effect of Reynolds number on the non-dimensional stream function for the fourth module for an in-line arrangement, *H/Da* = 2 and *L/Da* = 4: (a) Re = 25, (b) Re = 50, (c) Re = 100, (d) Re = 200, and (e) Re = 400.

TABLE 6.4 The minimum and maximum values of ψ^*, *H/Da* = 2 and *L/Da* = 4.

Re	Ψ^*_{min}	Ψ^*_{max}
25	-0.00019823	1
50	-0.00199013	1.00142
100	-0.0101553	1.00831
200	-0.019797	1.01666
400	-0.0264667	1.02241

The streamlines shown in Fig. 6.13 are symmetric, however, their magnitudes are not as the streamfunctions are set to 0 and 1 at *Y/H* = 0 and 1, respectively. For the staggered arrangement, this condition is not pronounced. Figs. 6.14 – 6.16 show the effect of Reynolds number on the non-dimensional stream function for the fourth module for a staggered arrangement for different values of tube spacing between the upper and lower rows, (i.e., *H/Da* = 2 and *L/Da* = 5, 6, and 7). The strength and size of the recirculation bubble gets larger as the Reynolds number increases. However, the recirculation behind the upper tube is smaller in size when compared to the one behind the lower tube as can be seen in Figs. 6.14c and d. This is due to the fact that half of the lower tube is located vertically in the same position as the recirculation behind the upper tube which would push the streamlines toward the top. This would restrict the upper recirculation and results in minimizing its size due to the reduction in the flow cross sectional area.

Re = 25

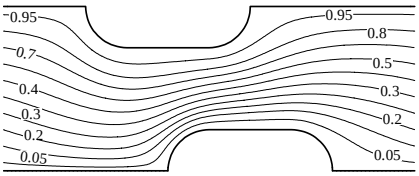

(a)

Re = 50

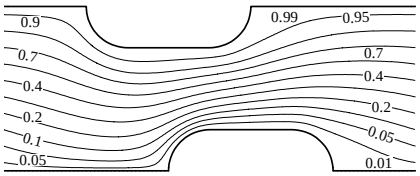

(b)

Re = 100

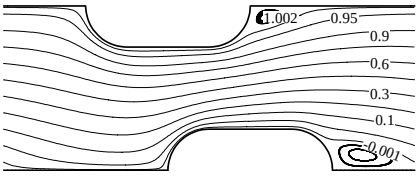

(c)

Re = 200

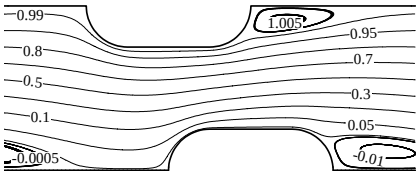

(d)

Re = 400

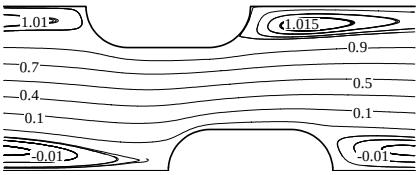

(e)

Fig. 6.14 Effect of Reynolds number on the non-dimensional stream function for the fourth module for a staggered arrangement, *H/Da* = 2 and *L/Da* = 5: (a) Re = 25, (b) Re = 50, (c) Re = 100, (d) Re = 200, and (e) Re = 400.

Re = 25

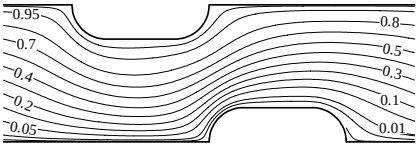

(a)

Re = 50

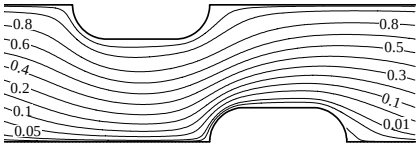

(b)

Re = 100

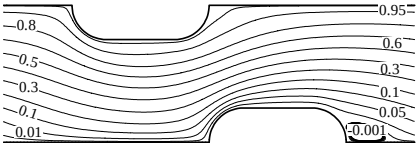

(c)

Re = 200

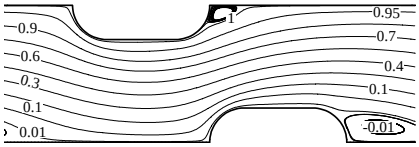

(d)

Re = 400

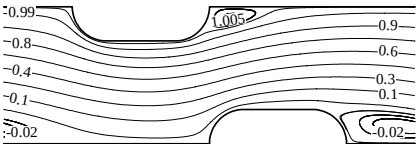

(e)

Fig. 6.15 Effect of Reynolds number on the non-dimensional stream function for the fourth module for a staggered arrangement, *H/Da* = 2 and *L/Da* = 6: (a) Re = 25, (b) Re = 50, (c) Re = 100, (d) Re = 200, and (e) Re = 400.

Re = 25

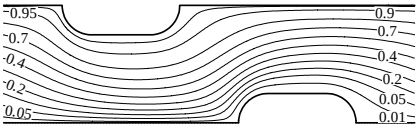

(a)

Re = 50

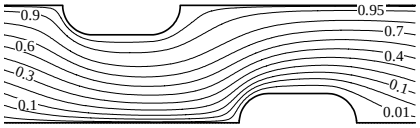

(b)

Re = 100

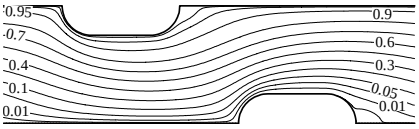

(c)

Re = 200

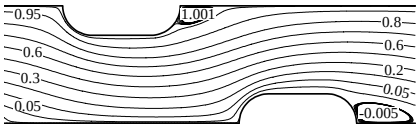

(d)

Re = 400

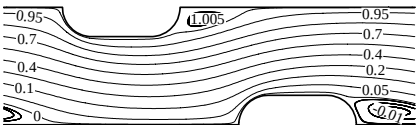

(e)

Fig. 6.16 Effect of Reynolds number on the non-dimensional stream function for the fourth module for a staggered arrangement, *H/Da* = 2 and *L/Da* = 7: (a) Re = 25, (b) Re = 50, (c) Re = 100, (d) Re = 200, and (e) Re = 400.

The spacing between the upper and lower tubes can be increased by shifting the lower tube toward the right. When the entire lower tubes push the streamlines to the top, the recirculation behind the upper tubes would become smaller and even disappear at moderate Reynolds number (Re = 100) which can be seen by comparing Figs. 6.15c with 6.14c. Further increase in the spacing between the upper and lower tubes would not decrease the upper recirculation. In fact, the recirculation would increase because there is enough distance between the rear edge of the upper tube and the front edge of the lower tube for the flow to expand as shown in Fig. 6.16. This fact is documented in Table 6.5 which lists the minimum and maximum values of non-dimensional stream function found in Figs 6.14, 6.15, and 6.16 at Re = 400.

TABLE 6.5 The minimum and maximum values of ψ^*, for staggered configuration, *H/Da* = 2, Re = 400.

L/Da	Ψ^*_{min}	Ψ^*_{max}
4	--	--
5	-0.0513913	1.01914
6	-0.0275414	1.00666
7	-0.0176458	1.0077

Figs 6.17 and 6.18 are representative results to study the variation of the non-dimensional stream function for the fourth module for an in-line arrangement at *H/Da* = 3 and 4, respectively. The length ratio (*L/Da*) was fixed at 4. These results can be compared with the results discussed earlier in Fig. 6.13 for *H/Da* = 2. As the height ratio increases, the strength and size of the recirculation bubble, right behind the tube (both upper and lower), would decrease as the flow has enough space to expand through the

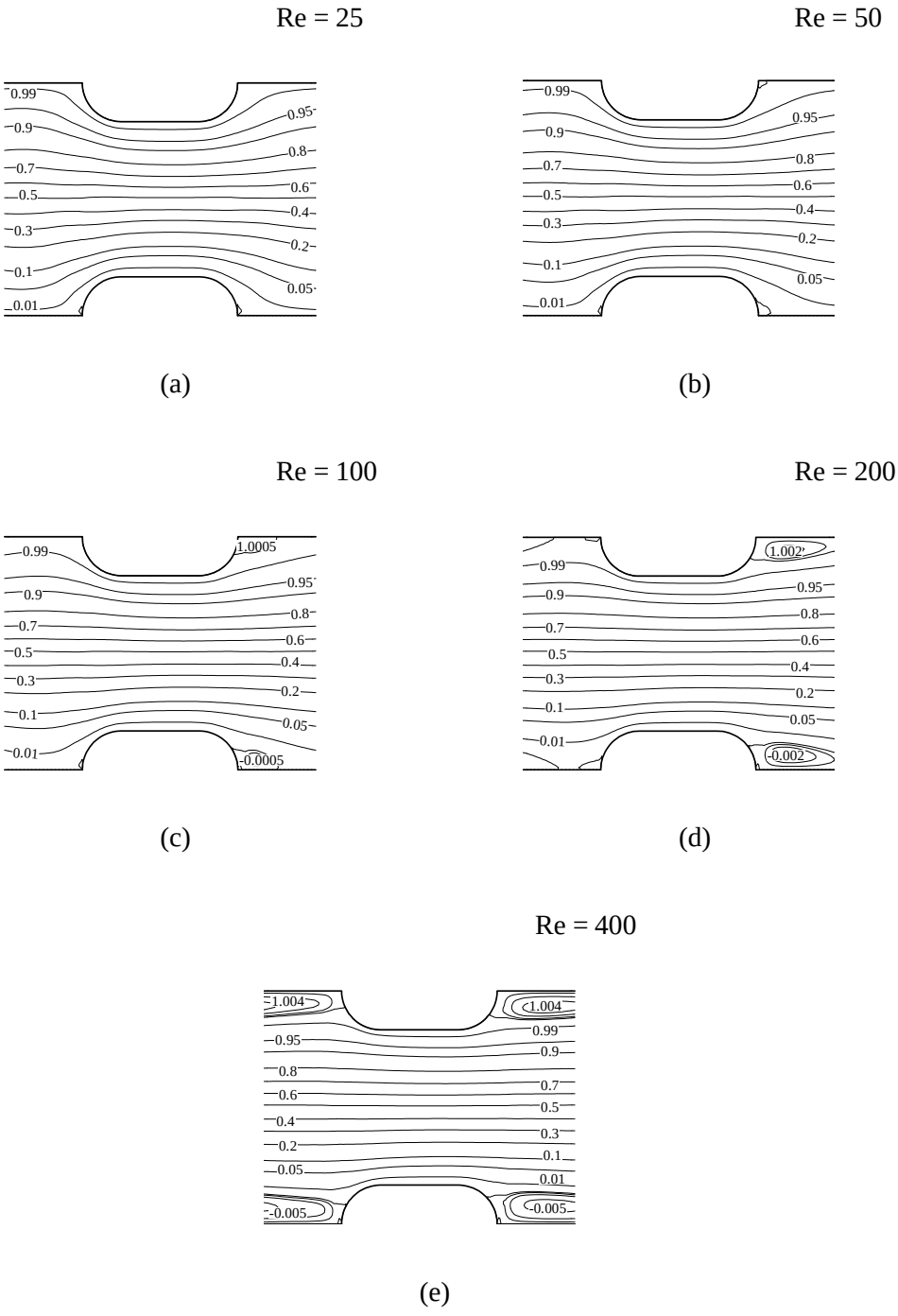

Fig. 6.17 Effect of Reynolds number on the non-dimensional stream function for the fourth module for an in-line arrangement, *H/Da* = 3 and *L/Da* = 4: (a) Re = 25, (b) Re = 50, (c) Re = 100, (d) Re = 200, and (e) Re = 400.

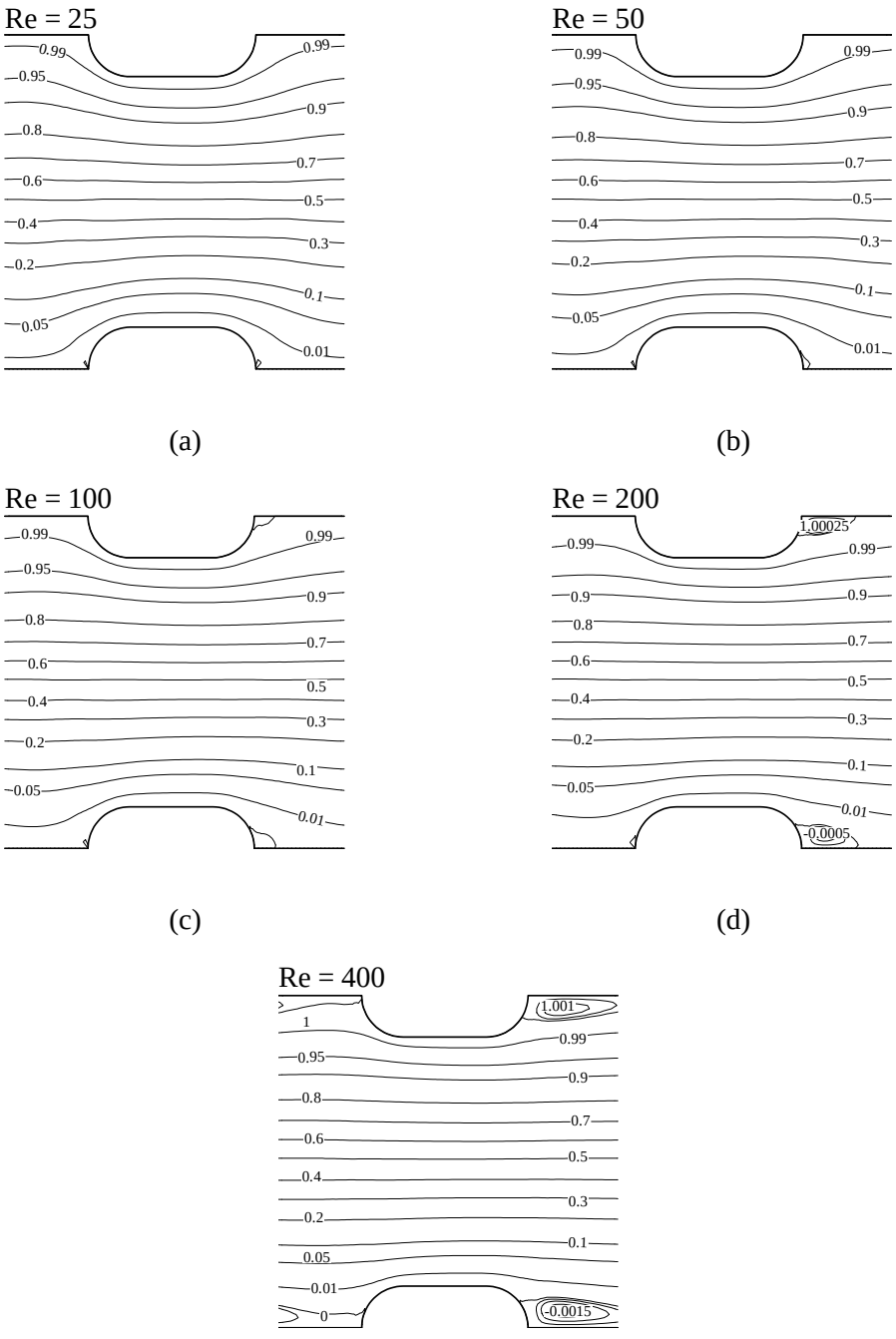

Fig. 6.18 Effect of Reynolds number on the non-dimensional stream function for the fourth module for an in-line arrangement, *H/Da* = 4 and *L/Da* = 4: (a) Re = 25, (b) Re = 50, (c) Re = 100, (d) Re = 200, and (e) Re = 400.

passage. The recirculation almost disappeared as can be seen by comparing Fig. 6.18c with Fig. 6.13c. Table 6.6 lists the minimum and maximum values of the non-dimensional stream function found in Figs. 6.13e, 6.17e, and 6.18e for different height ratio variations.

TABLE 6.6 The minimum and maximum values of ψ^*, for an in-line configuration, with *L/Da* = 4 and Re = 400.

H/Da	Ψ^*_{min}	Ψ^*_{max}
2	-0.0264667	1.02241
3	-0.0068874	1.00557
4	-0.00273447	1.00198

Figs 6.19 and 6.20 are representative results to study the effect of variation of the non-dimensional stream function for the fourth module for an in-line arrangement for *L/Da* = 5 and 6, respectively. The height ratio (*H/Da*) was fixed at 2. These results can be compared with the results presented earlier in Fig. 6.13 for *L/Da* = 4. The increase in length ratio does not significantly alter the strength and size of the recirculation right behind the tube (both upper and lower). The recirculation almost remains the same as can be seen in Figs 6.13, 6.19, and 6.20. this is also reflected in Table 6.7 which lists the minimum and maximum values of the non-dimensional stream function as a result of length ratio (*L/Da)* variations at Re = 400 and *H/Da* = 2.

Re = 25

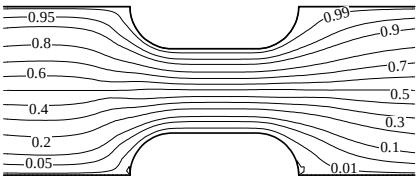

(a)

Re = 50

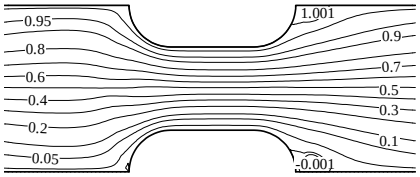

(b)

Re = 100

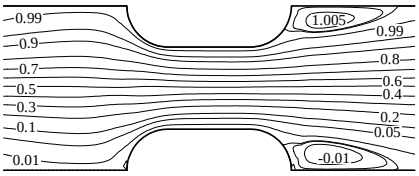

(c)

Re = 200

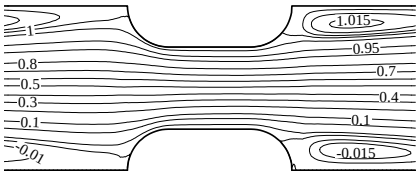

(d)

Re = 400

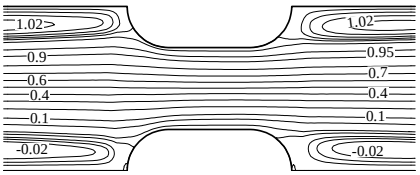

(e)

Fig. 6.19 Effect of Reynolds number on the non-dimensional stream function for the fourth module for an in-line arrangement, *H/Da* = 2 and *L/Da* = 5: (a) Re = 25, (b) Re = 50, (c) Re = 100, (d) Re = 200, and (e) Re = 400.

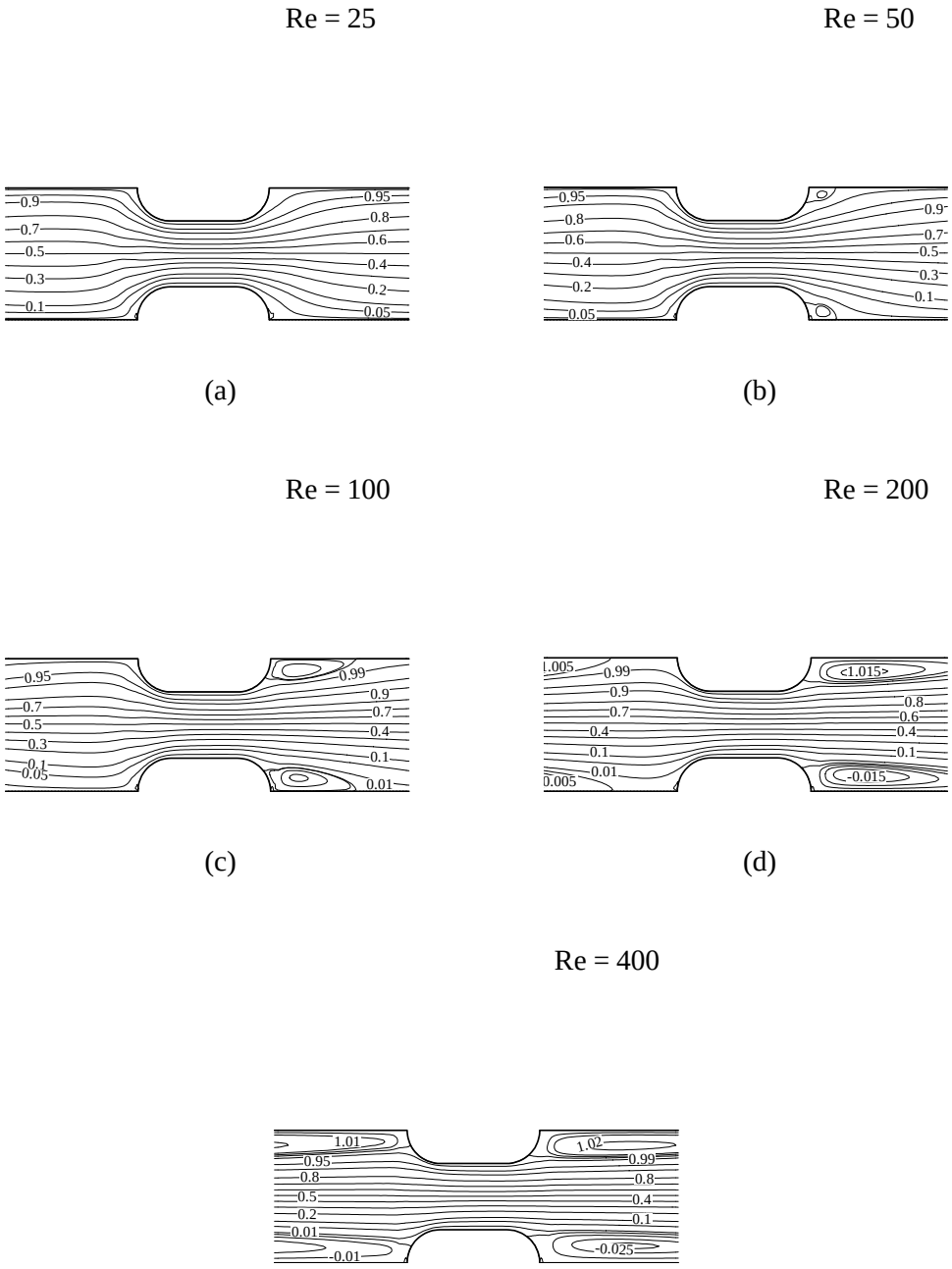

Fig. 6.20 Effect of Reynolds number on the non-dimensional stream function for the fourth module for an in-line arrangement, *H/Da* = 2 and *L/Da* = 6: (a) Re = 25, (b) Re = 50, (c) Re = 100, (d) Re = 200, and (e) Re = 400.

TABLE 6.7 The minimum and maximum values of ψ^*, for an in-line configuration, with *H/Da* = 2 and Re = 400.

L/Da	Ψ^*_{min}	Ψ^*_{max}
4	-0.0264667	1.02241
5	-0.0263192	1.0225
6	-0.0267858	1.02284
7	--	--

6.5.3 Isotherms

Fig. 6.21 shows the effect of Reynolds number on the normalized temperature lines (isotherms). All isotherms are ranging from 0 to 1 that represents a low fluid temperature at the inlet to higher fluid temperature as it reaches the hot tube surface. As the Reynolds number increases the lower value isotherms penetrate deeper which means the colder fluid is getting closer to the hot surface. As a result of this behavior, the heat transfer would be increased as will be shown later in the computed Nusselt number. The symmetric condition is preserved because of symmetric geometry which is not the case for the staggered arrangement with different length spacing as shown in Figs. 6.22 – 6.24. It is clear that the flow is pushed up as a result of the presence of the lower tube.

A comparison of Figs. 6.25 and 6.26 with Fig. 6.21 shows the effect of varying the height ratio on the isotherms. The increase in height ratio would make the cold isotherms penetrate further downstream as clearly shown in Figs. 6.21, 6.25, and 6.26 c

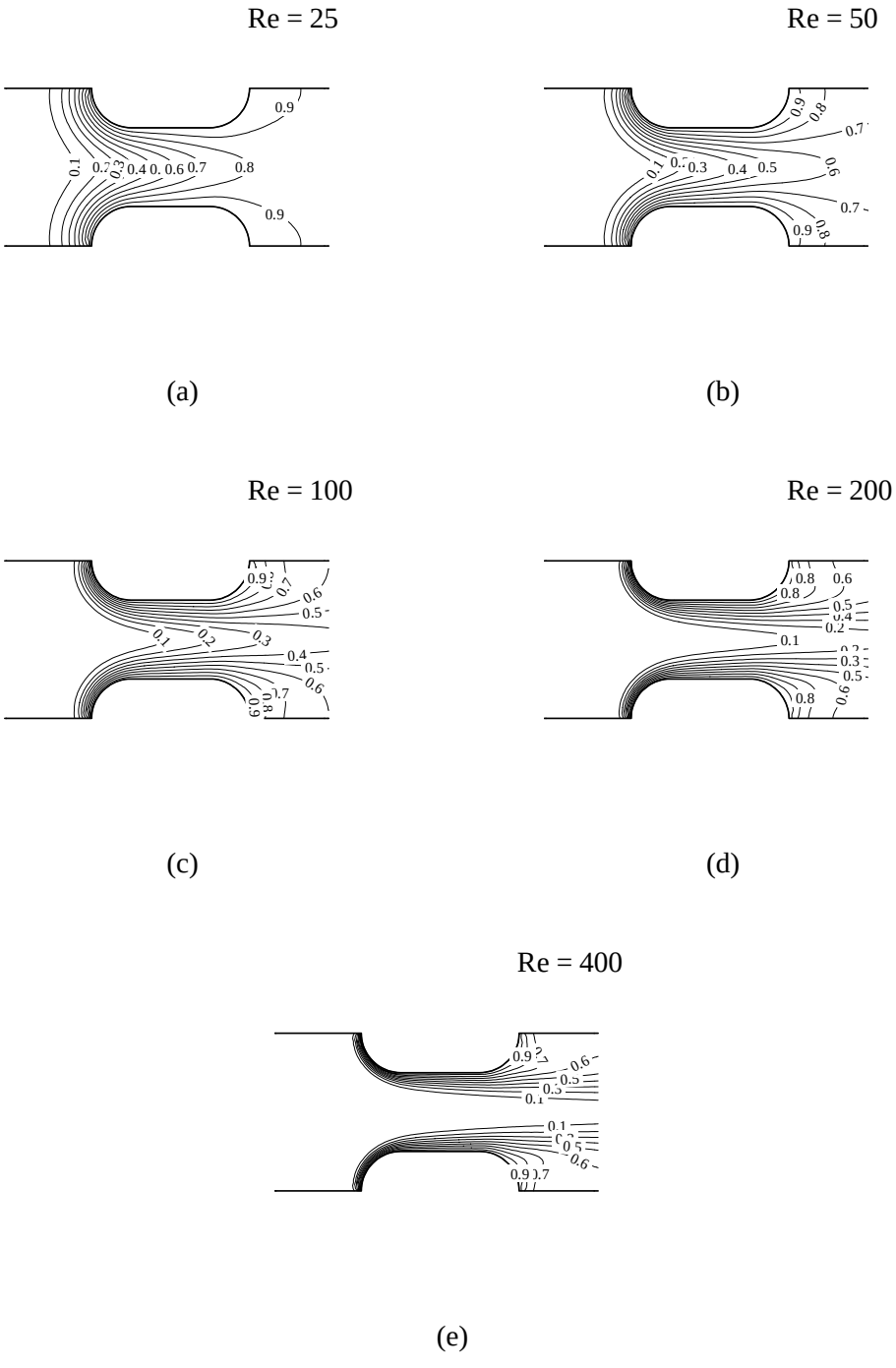

Fig. 6.21 Effect of Reynolds number on isotherms for the fourth module for an in-line arrangement, *H/Da* = 2, *L/Da* = 4, and Pr = 0.7: (a) Re = 25, (b) Re = 50, (c) Re = 100, (d) Re = 200, and (e) Re = 400.

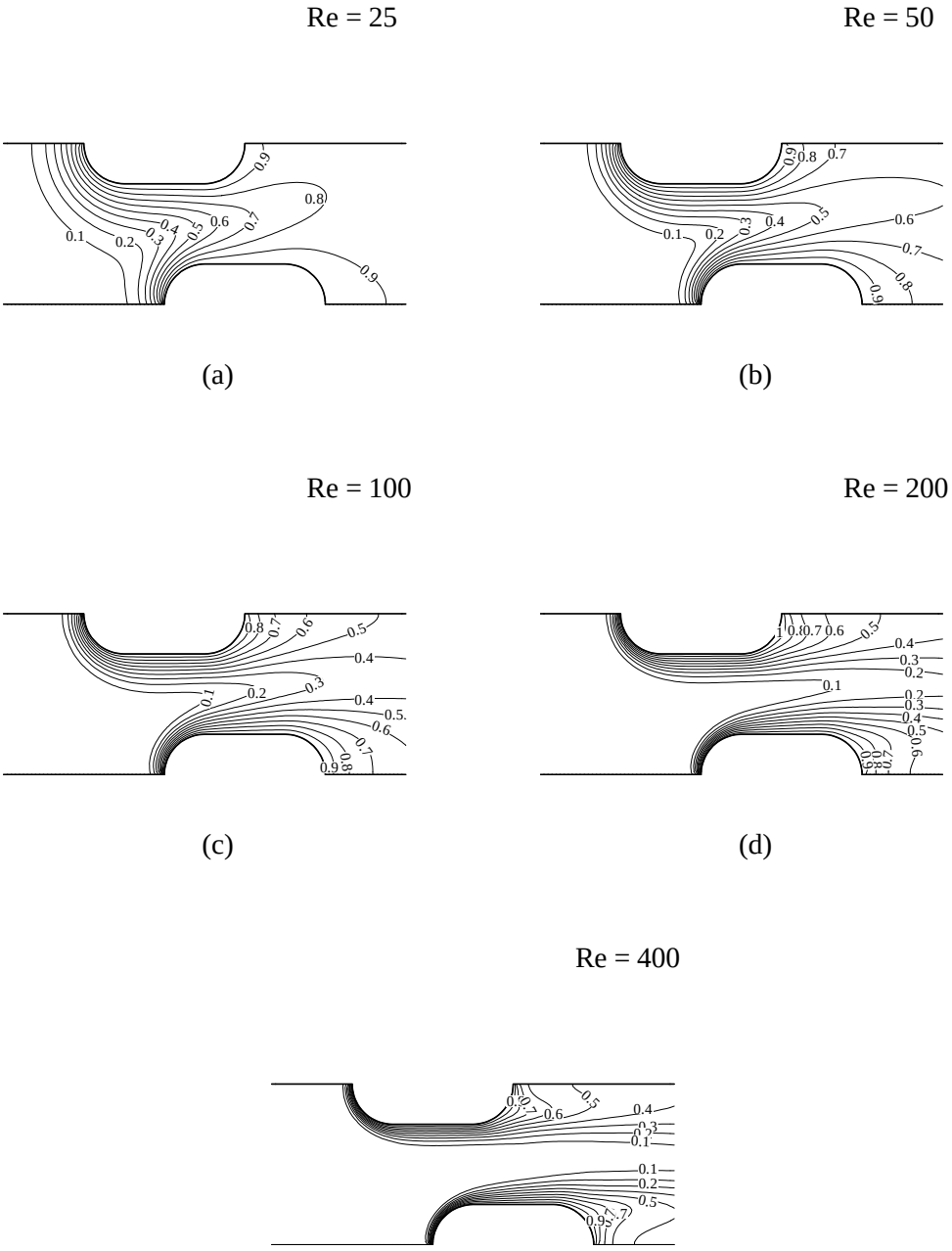

Fig. 6.22 Effect of Reynolds number on isotherms for the fourth module for a staggered arrangement, *H/Da* = 2, *L/Da* = 5, and Pr = 0.7: (a) Re = 25, (b) Re = 50, (c) Re = 100, (d) Re = 200, and (e) Re = 400.

Re = 25

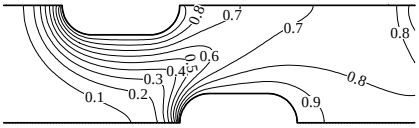

(a)

Re = 50

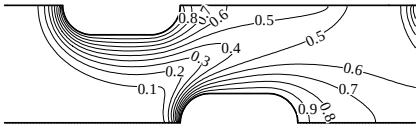

(b)

Re = 100

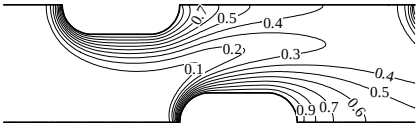

(c)

Re = 200

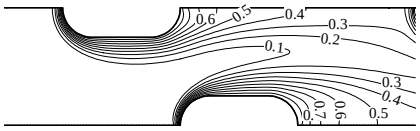

(d)

Re = 400

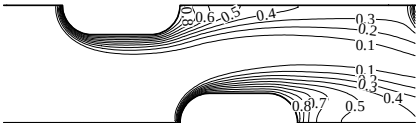

(e)

Fig. 6.23 Effect of Reynolds number on isotherms for the fourth module for a staggered arrangement, *H/Da* = 2, *L/Da* = 6, and Pr = 0.7: (a) Re = 25, (b) Re = 50, (c) Re = 100, (d) Re = 200, and (e) Re = 400.

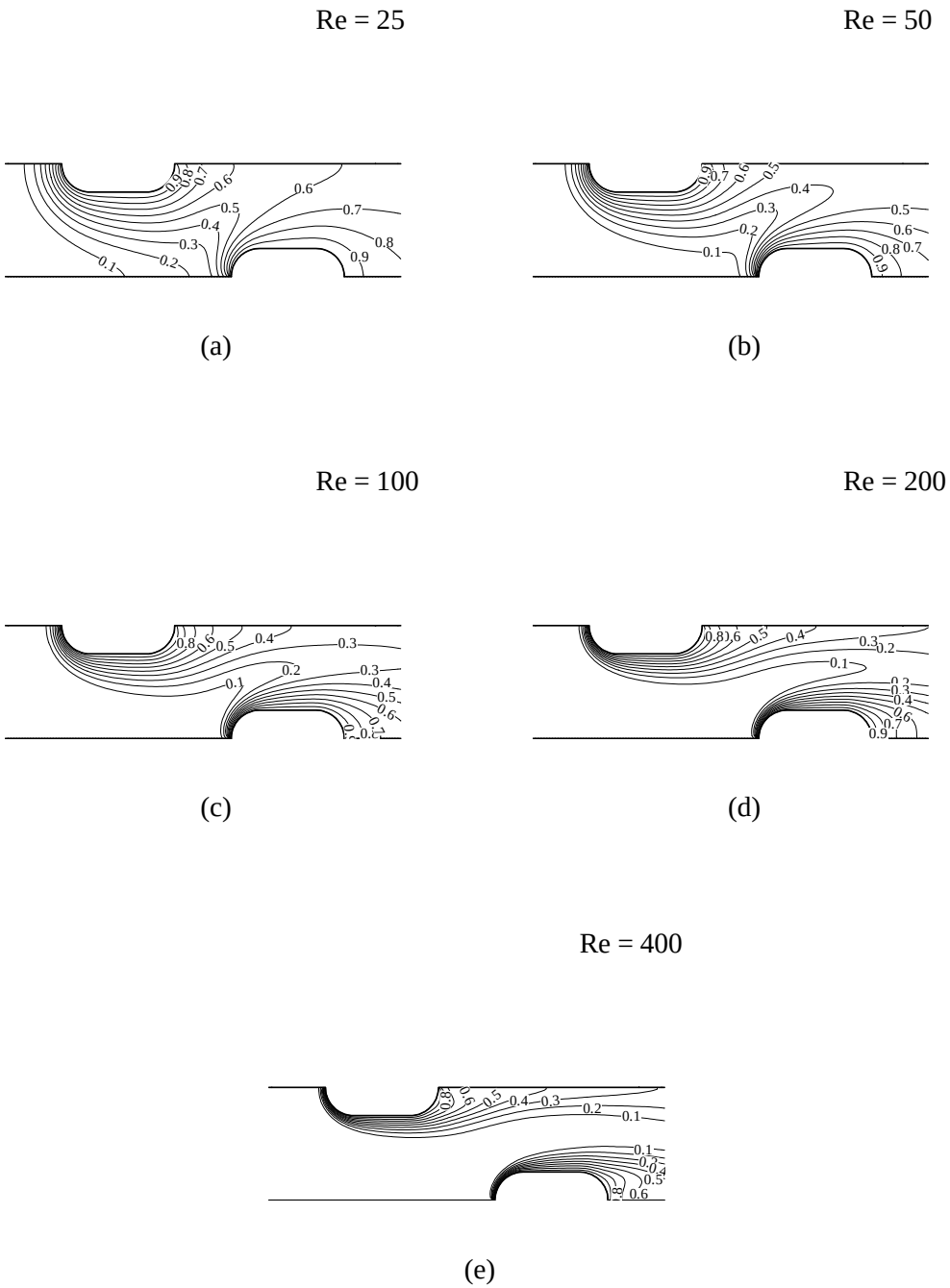

Fig. 6.24 Effect of Reynolds number on isotherms for the fourth module for a staggered arrangement, *H/Da* = 2, *L/Da* = 7, and Pr = 0.7: (a) Re = 25, (b) Re = 50, (c) Re = 100, (d) Re = 200, and (e) Re = 400.

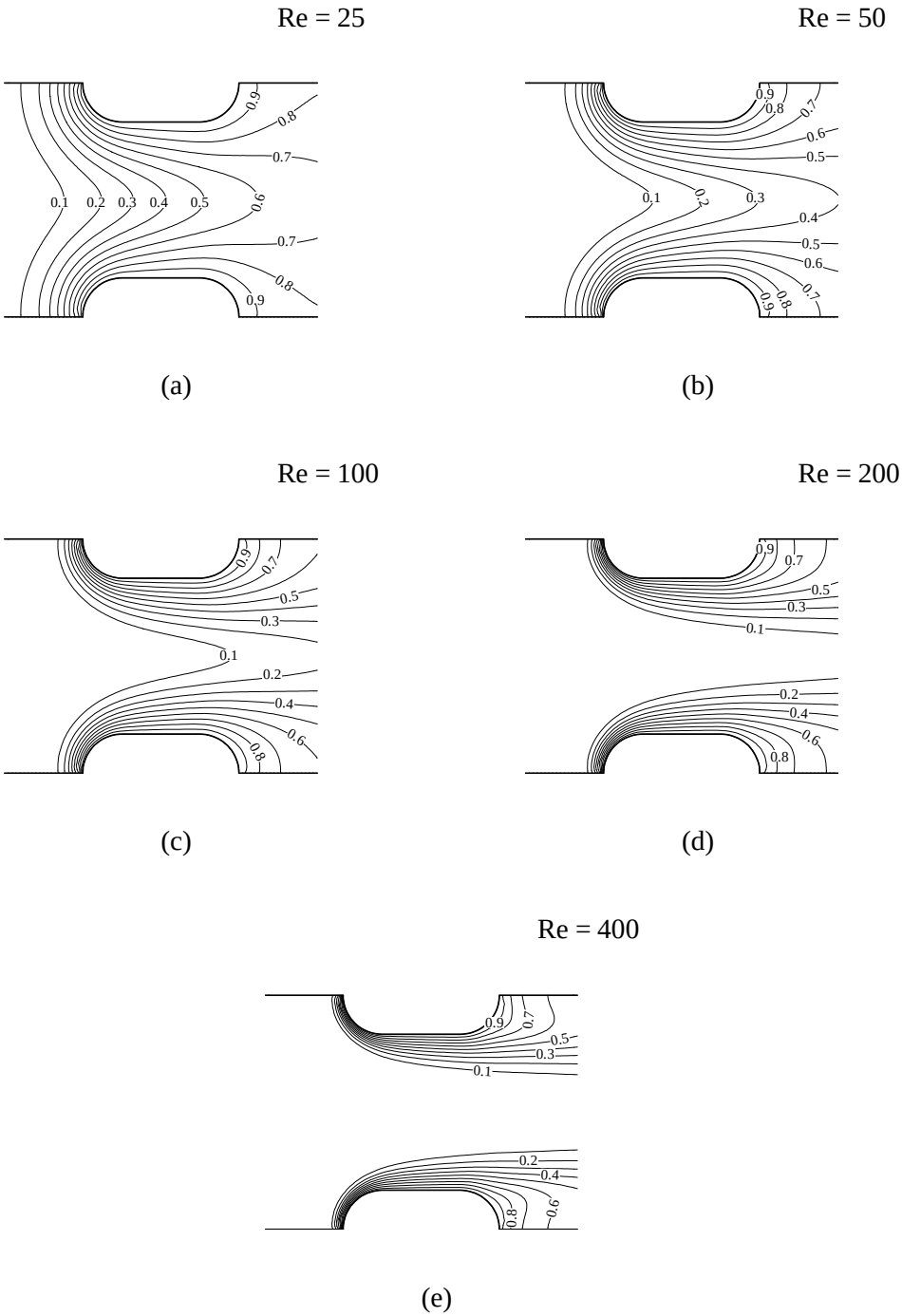

Fig. 6.25 Effect of Reynolds number on isotherms for the fourth module for an in-line arrangement, *H/Da* = 3, *L/Da* = 4, and Pr = 0.7: (a) Re = 25, (b) Re = 50, (c) Re = 100, (d) Re = 200, and (e) Re = 400.

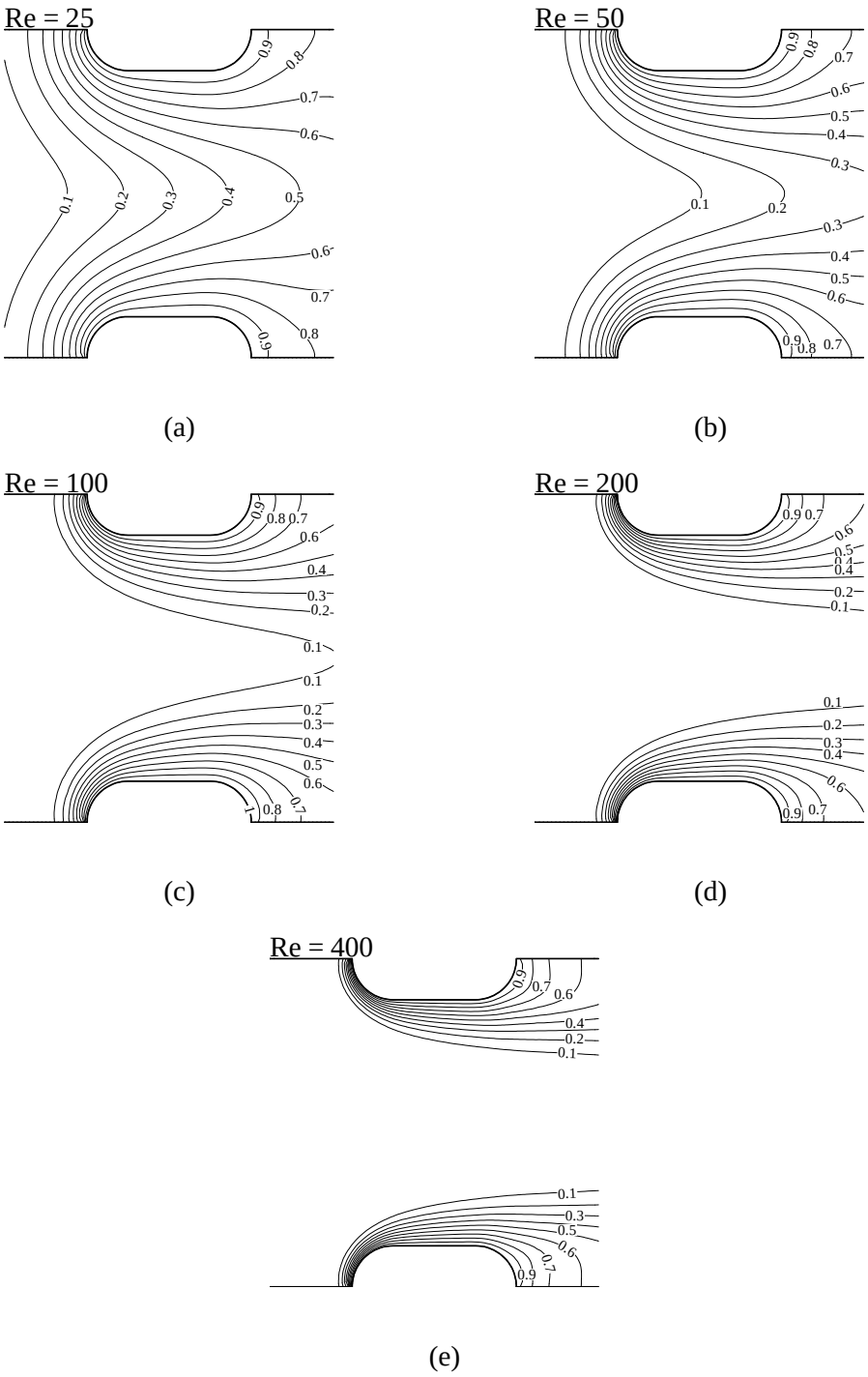

Fig. 6.26 Effect of Reynolds number on isotherms for the fourth module for an in-line arrangement, *H/Da* = 4, *L/Da* = 4, and Pr = 0.7: (a) Re = 25, (b) Re = 50, (c) Re = 100, (d) Re = 200, and (e) Re = 400.

and d. However, the colder isotherms are farther from the hot tube surface which implies lower heat transfer.

Comparison of Fig. 6.21 with Figs 6.27 and 6.28 shows the effect of varying the length ratio (*L/Da*) on the isotherms. The impact of varying length ratio is minimal on isotherms and thus does not have much of an impact on heat transfer. All isotherms given above, Figs. 6.21- 6.28, are for air (Pr = 0.7). Fig. 6.29 has the same parameters given in Fig. 6.21 except the Prandlt number. Increase in Pr significantly impacts distribution of isotherms. At a higher value of Pr the isotherms are more densely packed implying better heat transfer. This behavior is more pronounced at higher Reynolds numbers (Re = 400).

6.5.4 Normalized Pressure Drop

Since the velocity profile is nearly symmetric (for the in-line arrangement only) and repeats itself for other modules, the pressure drop across the modules has a spatially periodic behavior. This is the primary reason that the computed pressure drop is nearly constant for all modules except for the first and the last. Numerical data for dimensionless pressure differences across the interior modules for the in-line arrangements can be found in Table 6.8. The dimensionless pressure differences for the staggered arrangements are presented in Table 6.9. The data shows that the values are nearly constant for a given Reynolds number and a fixed set of aspect ratios. Therefore, it is reasonable to present the pressure drop across one module as a function of the Reynolds number. Minor variations were detected for the first and the last modules due to end effects.

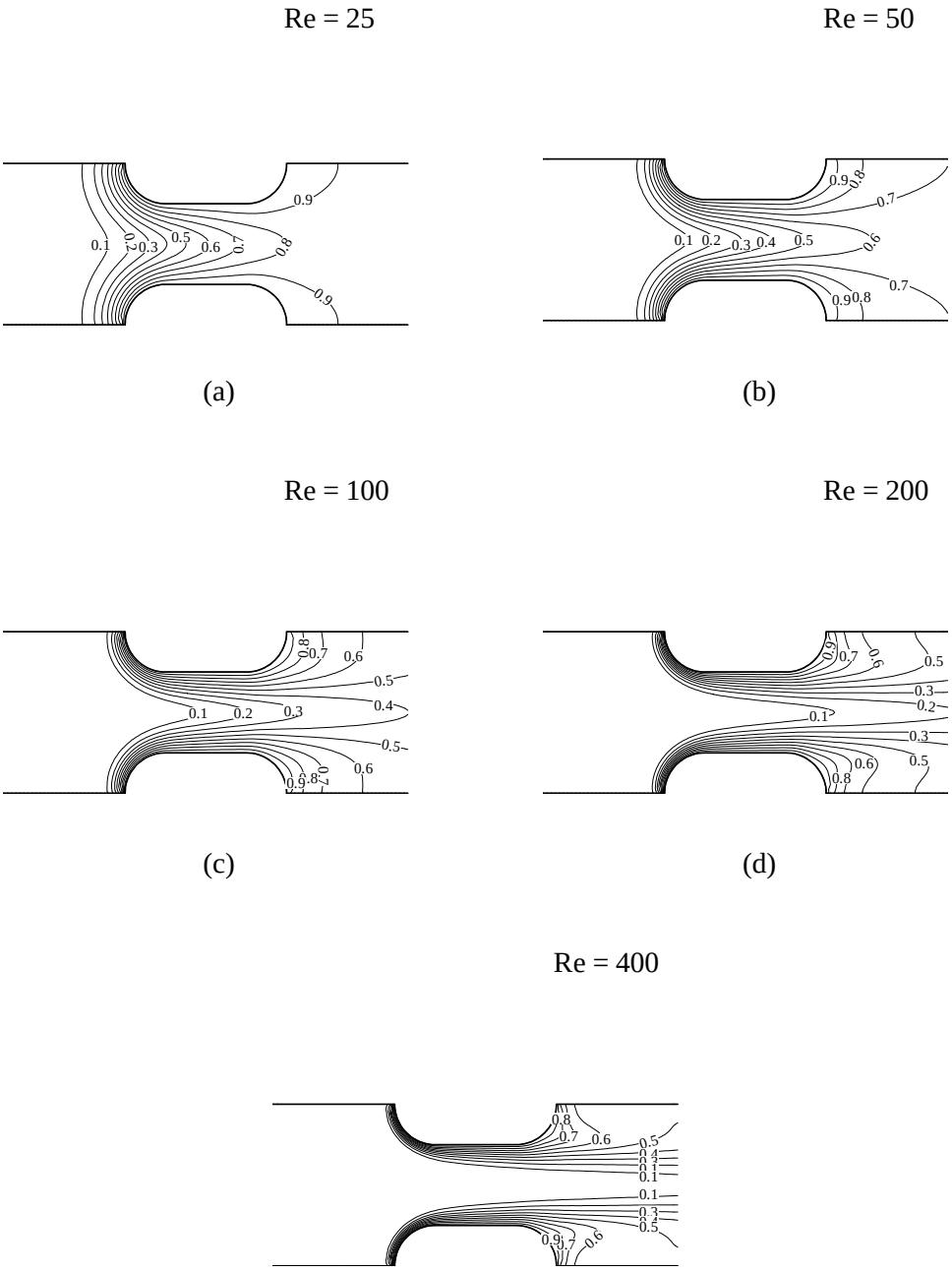

Fig. 6.27 Effect of Reynolds number on isotherms for the fourth module for an in-line arrangement, *H/Da* = 2, *L/Da* = 5, and Pr = 0.7: (a) Re = 25, (b) Re = 50, (c) Re = 100, (d) Re = 200, and (e) Re = 400.

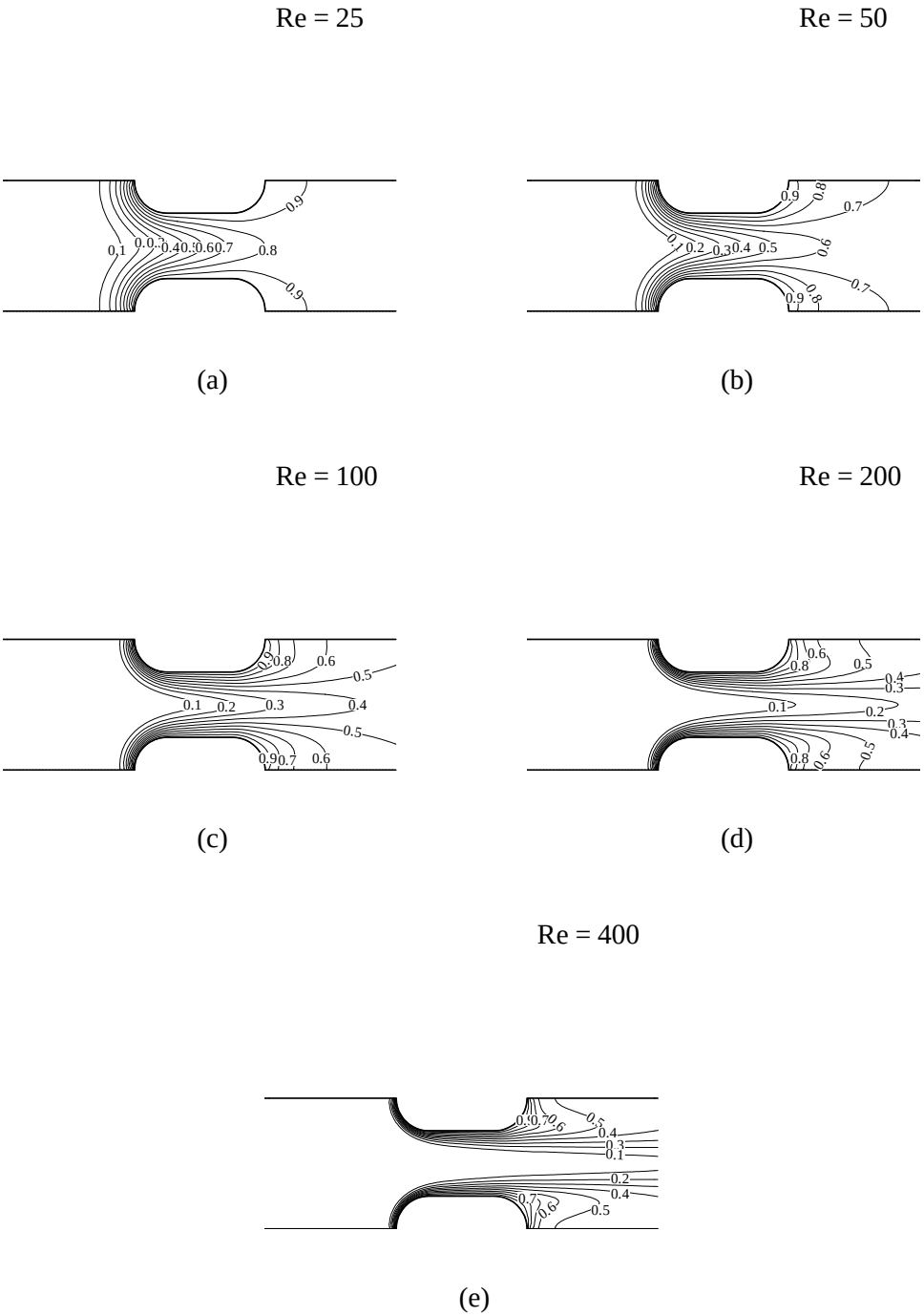

Fig. 6.28 Effect of Reynolds number on isotherms for the fourth module for an in-line arrangement, *H/Da* = 2, *L/Da* = 6, and Pr = 0.7: (a) Re = 25, (b) Re = 50, (c) Re = 100, (d) Re = 200, and (e) Re = 400.

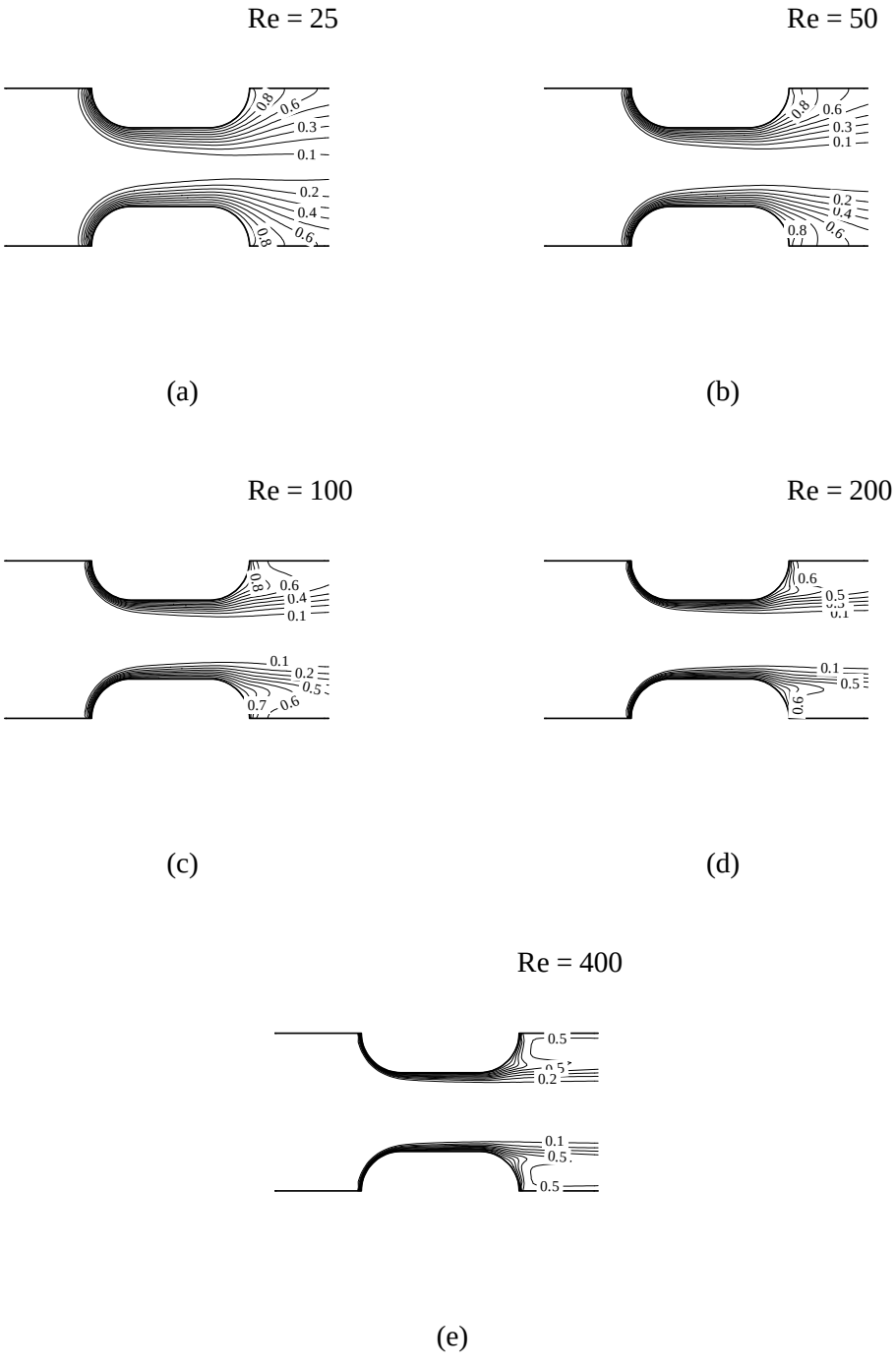

Fig. 6.29 Effect of Reynolds number on isotherms for the fourth module for an in-line arrangement, *H/Da* = 2, *L/Da* = 4, and Pr = 7.0: (a) Re = 25, (b) Re = 50, (c) Re = 100, (d) Re = 200, and (e) Re = 400.

TABLE 6.8 Modules ΔP^* for in-line arrangements at selected Reynolds numbers.

H/Da	Re	2nd	3rd	4th	5th
			L/Da = 4		
2	25	9.094	9.102	9.114	9.125
	100	2.665	2.652	2.649	2.647
	400	1.049	0.968	0.970	0.941
3	25	3.336	3.338	3.339	3.339
	100	0.942	0.914	0.912	0.912
	400	0.375	0.314	0.284	0.269
4	25	2.055	2.059	2.060	2.060
	100	0.584	0.549	0.543	0.542
	400	0.233	0.202	0.180	0.167
			L/Da = 5		
2	25	9.201	9.199	9.191	9.181
	100	2.823	2.817	2.816	2.817
	400	1.083	0.975	0.958	1.002
3	25	3.449	3.448	3.443	3.436
	100	1.014	0.996	0.996	0.997
	400	0.423	0.352	0.324	0.320
4	25	2.165	2.166	2.168	2.170
	100	0.633	0.604	0.602	0.602
	400	0.250	0.216	0.198	0.192
			L/Da = 6		
2	25	9.212	9.212	9.210	9.207
	100	2.928	2.924	2.923	2.922
	400	1.154	1.028	1.032	1.046
3	25	3.490	3.489	3.486	3.482
	100	1.061	1.049	1.050	1.051
	400	0.408	0.310	0.286	0.300
4	25	2.217	2.221	2.226	2.231
	100	0.665	0.643	0.642	0.643
	400	0.273	0.232	0.216	0.215

TABLE 6.9 Modules ΔP^* for staggered arrangements at selected Reynolds number.

H/Da	Re	2nd	3rd	4th	5th
			L/Da = 5		
2	25	7.845	7.844	7.840	7.836
	100	2.490	2.484	2.484	2.483
	400	1.115	0.943	0.925	0.921
3	25	3.568	3.563	3.562	3.561
	100	1.079	1.052	1.055	1.055
	400	0.465	0.363	0.341	0.330
4	25	2.379	2.371	2.372	2.372
	100	0.690	0.662	0.661	0.661
	400	0.285	0.233	0.212	0.200
			L/Da = 6		
2	25	4.702	4.696	4.686	4.676
	100	1.628	1.627	1.627	1.628
	400	0.746	0.673	0.655	0.652
3	25	3.025	3.023	3.023	3.022
	100	0.993	0.976	0.976	0.976
	400	0.465	0.367	0.344	0.335
4	25	2.305	2.295	2.295	2.295
	100	0.710	0.685	0.685	0.685
	400	0.312	0.245	0.225	0.215
			L/Da = 7		
2	25	3.278	3.276	3.276	3.277
	100	1.258	1.256	1.254	1.254
	400	0.579	0.524	0.511	0.508
3	25	2.412	2.412	2.415	2.420
	100	0.861	0.851	0.852	0.853
	400	0.416	0.346	0.322	0.314
4	25	2.026	2.018	2.017	2.017
	100	0.671	0.650	0.650	0.649
	400	0.310	0.244	0.224	0.213

Fig. 6.30 provides the normalized pressure drop for the fourth module for in-line configurations. Figs 6.30 a, c, and e show the impact of height ratio on the normalized pressure drop at fixed length ratio (L/Da = 4, 5, and 6, respectively). As the height ratio increases the normalized pressure drop decreases. Figs 6.30 b, d, and f show the impact of length ratio on the normalized pressure drop at fixed height ratio (H/Da = 2, 3, and 4, respectively). It can be clearly stated that the length ratio has very little effect or even a negligible effect on pressure drop. As expected the normalized pressure drop decreased with an increase in Re. Fig. 6.31 presents the dimensionless pressure difference for the fourth module for staggered configurations. The normalized pressure drop behavior for a staggered configuration is similar to that for an in-line configuration.

6.5.5 Module Average Nusselt Number

Tables 6.10 and 6.11 show the computed average Nusselt number for the interior modules for Pr = 0.7 for in-line and staggered arrangements, respectively. From these tables, it is evident that for a given Reynolds number the module average Nusselt number remains fairly constant thus signifying the existence of a thermally periodically fully developed flow condition. Fig. 6.32 shows the average Nusselt number as a function of Reynolds number for the fourth module for in-line configurations for Pr = 0.7. Fig. 6.32a, c, and e show the effect of height ratio on the average Nusselt number for fixed length ratios. Fig. 6.32b, d, and f show the effect of length ratio on the average Nusselt number for fixed height ratios. In general, the module average Nusselt number increases with an increase in Reynolds number.

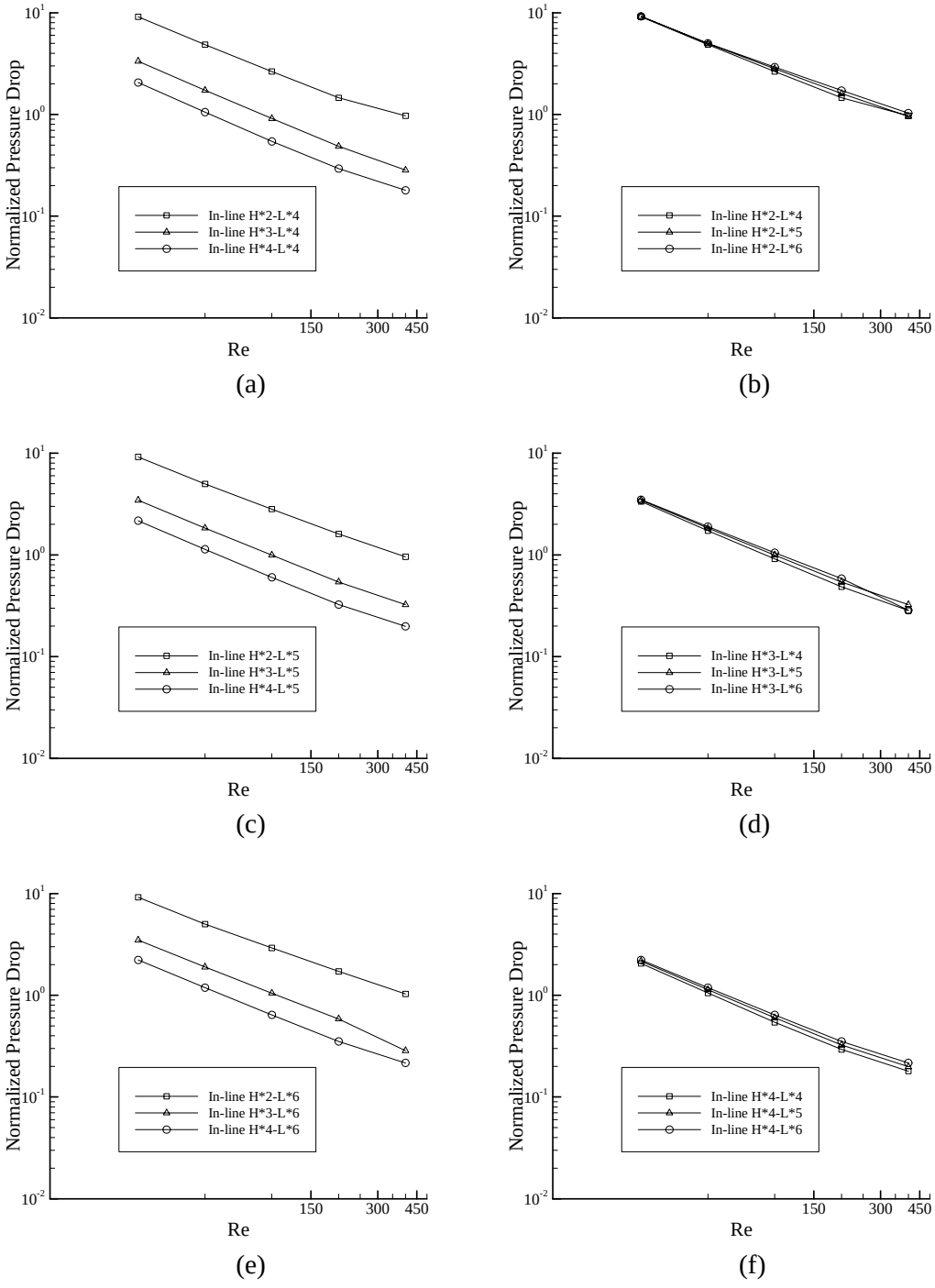

Fig. 6.30 Normalized pressure drop across the fourth module for in-line arrangements: (a) In-line L*4, (b) In-line H*2, (c) In-line L*5, (d) In-line H*3, (e) In-line L*6, and (f) In-line H*4 configurations.

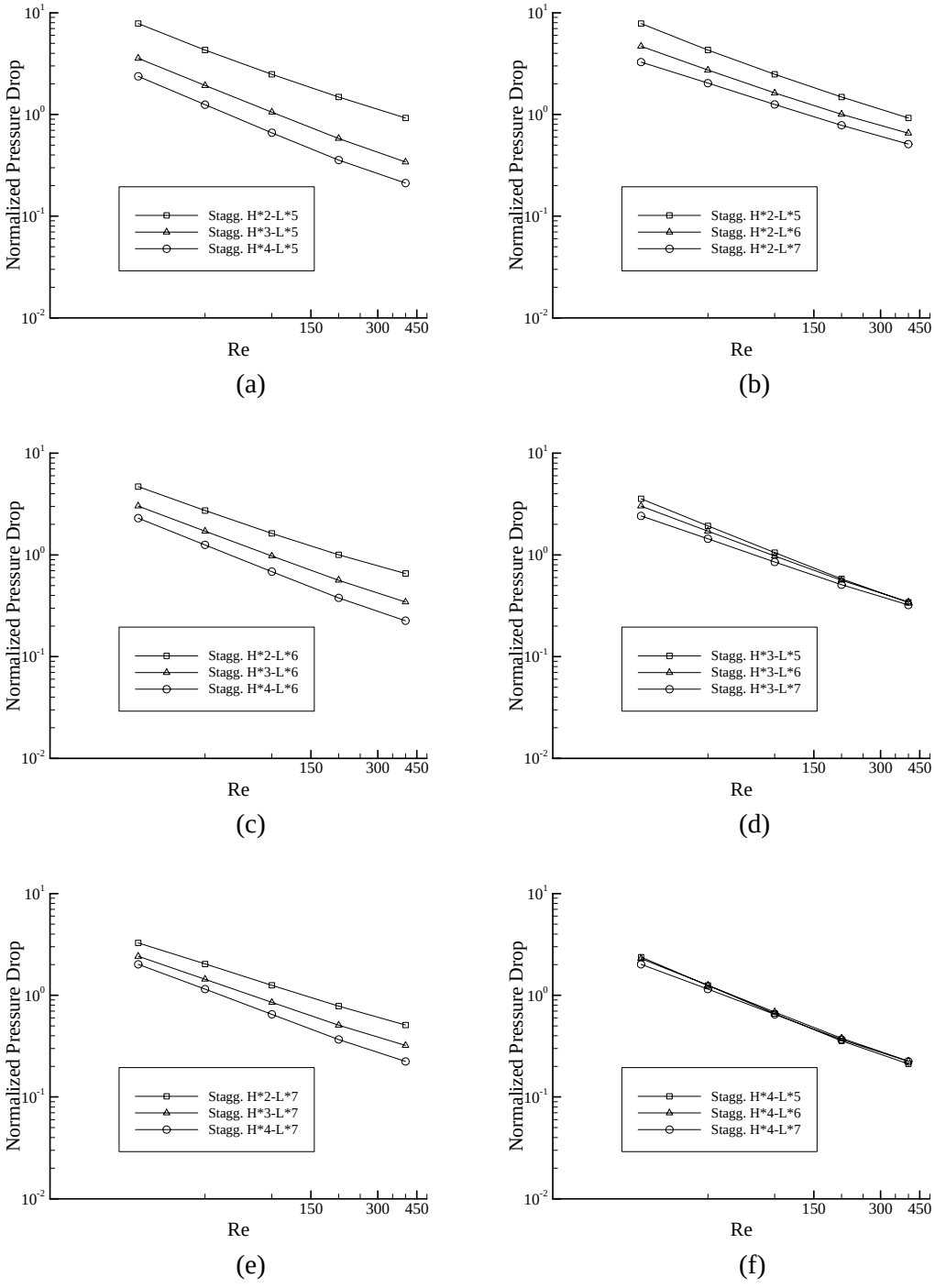

Fig. 6.31 Normalized pressure drop across the fourth module for staggered arrangements: (a) Stagg. L*5, (b) Stagg. H*2, (c) Stagg. L*6, (d) Stagg. H*3, (e) Stagg. L*7, and (f) Stagg. H*4 configurations.

TABLE 6.10 Average Nusselt number for interior modules, in-line arrangements, Pr = 0.7.

H/Da	Re	2nd	3rd	4th	5th
		L/Da = 4			
2	25	10.38	10.38	10.39	10.39
	100	14.61	14.60	14.60	14.60
	400	18.07	17.33	17.29	17.44
3	25	10.75	10.75	10.75	10.75
	100	12.86	12.82	12.82	12.82
	400	16.14	14.74	14.21	14.02
4	25	10.85	10.85	10.85	10.85
	100	12.42	12.24	12.23	12.23
	400	16.14	14.50	13.67	13.27
		L/Da = 5			
2	25	10.43	10.44	10.44	10.43
	100	15.16	15.16	15.16	15.15
	400	19.41	18.73	18.59	18.54
3	25	11.05	11.05	11.05	11.05
	100	13.75	13.73	13.73	13.74
	400	17.24	15.97	15.62	15.52
4	25	11.46	11.46	11.47	11.47
	100	13.49	13.38	13.38	13.38
	400	17.55	15.82	15.12	14.80
		L/Da = 6			
2	25	10.44	10.45	10.44	10.44
	100	15.51	15.51	15.51	15.51
	400	20.07	19.59	19.49	19.45
3	25	11.15	11.15	11.15	11.15
	100	14.36	14.35	14.35	14.35
	400	18.21	17.03	16.74	16.61
4	25	11.72	11.72	11.73	11.73
	100	14.26	14.19	14.19	14.19
	400	18.60	16.93	16.31	16.08

TABLE 6.11 Average Nusselt number for interior modules, Staggered arrangements, Pr = 0.7.

H/Da	Re	2nd	3rd	4th	5th
		L/Da = 5			
2	25	9.99	9.99	9.99	9.99
	100	14.63	14.63	14.63	14.63
	400	19.75	18.78	18.73	18.71
3	25	10.94	10.94	10.94	10.94
	100	13.79	13.74	13.75	13.76
	400	17.45	16.30	15.95	15.86
4	25	11.52	11.51	11.51	11.51
	100	13.63	13.50	13.50	13.50
	400	17.74	16.05	15.35	15.07
		L/Da = 6			
2	25	8.77	8.78	8.78	8.78
	100	13.37	13.40	13.40	13.41
	400	18.09	17.54	17.49	17.49
3	25	10.46	10.46	10.46	10.46
	100	13.97	13.95	13.96	13.97
	400	18.35	17.10	16.82	16.77
4	25	11.54	11.53	11.54	11.54
	100	14.31	14.21	14.22	14.23
	400	18.88	17.16	16.57	16.35
		L/Da = 7			
2	25	7.80	7.80	7.81	7.81
	100	12.59	12.64	12.65	12.65
	400	17.48	17.03	16.98	16.98
3	25	9.79	9.80	9.80	9.80
	100	13.80	13.84	13.87	13.87
	400	18.73	17.55	17.29	17.25
4	25	11.25	11.25	11.26	11.26
	100	14.58	14.54	14.57	14.57
	400	19.69	17.96	17.43	17.25

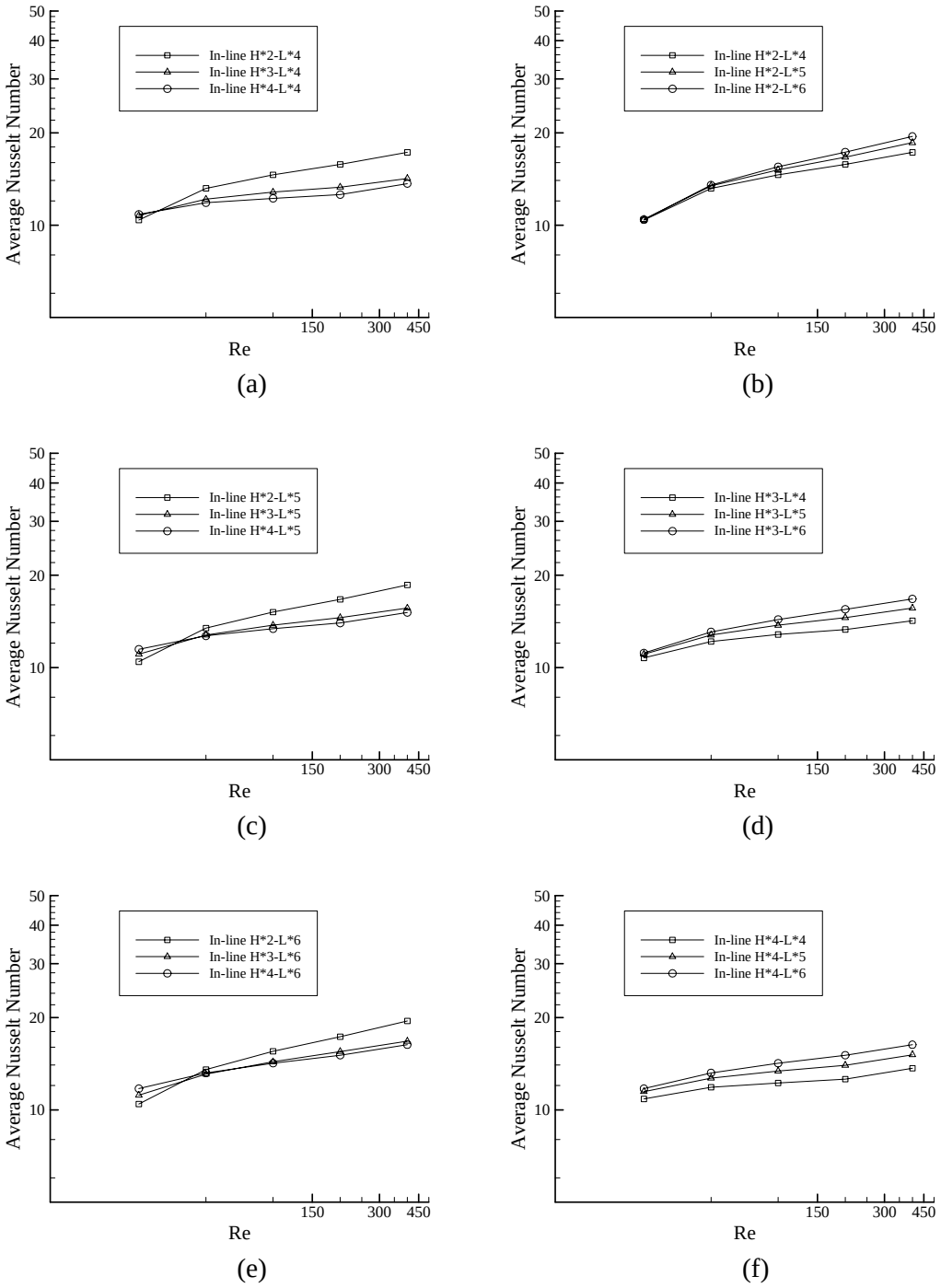

Fig. 6.32 Average Nusselt number for the fourth module, Pr = 0.7, for in-line arrangements: (a) In-line L*4, (b) In-line H*2, (c) In-line L*5, (d) In-line H*3, (e) In-line L*6, and (f) In-line H*4 configurations.

The overall performance of an in-line configuration with a lower height ratio (*H/Da* = 2) is preferable since it provides higher heat transfer rate for all length ratios and Reynolds numbers except for the lowest value (Re = 25) as shown in Fig. 6.32a, c, and e. This fact was established earlier when isotherms were discussed for different height ratios. The vicinity of colder isotherms to the hot tube surface would imply high heat transfer. On the other hand, an increase of the length ratio would result in a slight increase in the module average Nusselt number at a lower height ratio (*H/Da* = 2) and quite a significant increase at a higher height ratio (*H/Da* = 2) as shown in Fig. 6.32b, d, and f. In staggered configurations, the one with minimum spacing between the upper and lower tubes appears to give a higher module average Nusselt number if the height and length ratios are maintained at the lowest value (*H/Da* = 2 and *L/Da* = 5) as shown in Fig. 6.33a and b, respectively. However, at higher height and length ratios (*H/Da* = 4 and *L/Da* = 7) the staggered configuration with the higher spacing gives a higher module average Nusselt number as shown in Fig. 6.33e and f, respectively.

Tables 6.12 and 6.13 show the module average Nusselt numbers for the inner modules when water is used as a working fluid (i.e., Pr = 7.0) for in-line and staggered arrangements, respectively. The presented results indicates an increase in the module average Nusselt number when compared with the data presented in Table 6.10 or Table 6.11 for Pr = 0.7. Both in-line and staggered configurations do not attain a periodically fully developed condition at Re = 400.

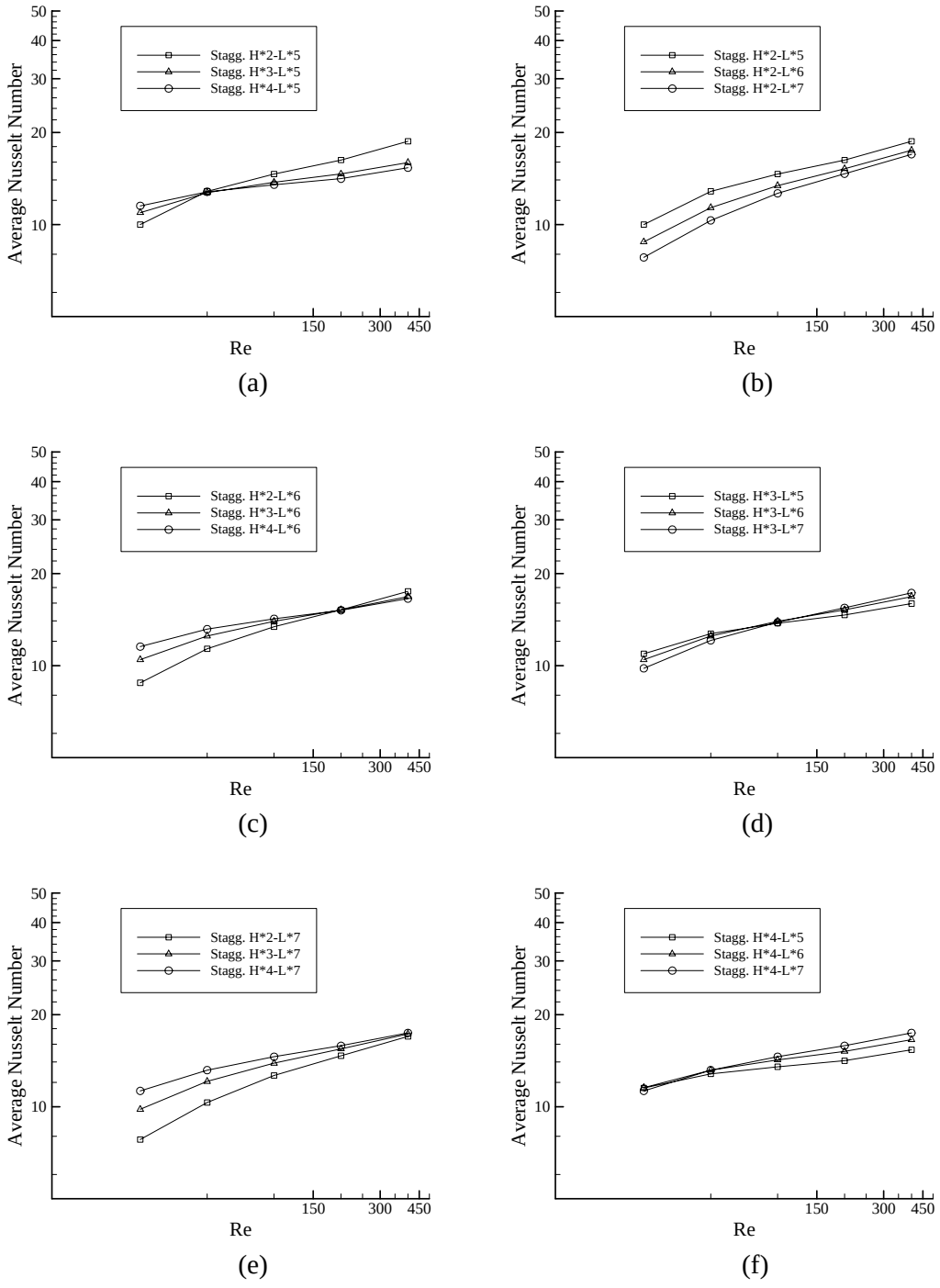

Fig. 6.33 Average Nusselt number for the fourth module, Pr = 0.7, for staggered arrangements: (a) Stagg. L*5, (b) Stagg. H*2, (c) Stagg. L*6, (d) Stagg. H*3, (e) Stagg. L*7, and (f) Stagg. H*4 configurations.

Fig. 6.34 shows the module average Nusselt number for in-line arrangements at Pr = 7.0. Figs 6.34a, c, and e are showing the effect of height ratio on module average Nusselt number for a fixed length ratios (*L/Da* = 4, 5, or 6 respectively). Figs 6.34 b, d, and f show the effect of length ratio on module average Nusselt number for a fixed height ratios (*H/Da* = 2, 3, or 4 respectively). The configuration with lower height ratio (*H/Da* = 2) provides the highest values of module average Nusselt number. The impact of further increase in height ratio (*H/Da* = 3 or 4) was found to be negligible on the module average Nusselt number as can be seen in Fig. 6.34a, c and e. Small changes can be detected as a result of length ratio increase for the configuration with the highest height ratio (*H/Da* = 4) as shown in Figs 6.34 b, d and f. The module average Nusselt number for staggered arrangement at Pr = 7.0 can be seen in Fig. 6.35. The qualitative behavior of module average Nusselt number for Pr = 7.0 is similar to those for Pr = 0.7

6.5.6 Heat Transfer Enhancement and Performance Ratios

The effectiveness of using flat tube was evaluated by studying the ratio of the module average Nusselt number for periodically fully developed flow of flat tube configurations and the module average Nusselt number for periodically fully developed flow for circular tube configurations. Henceforth, this ratio will be referred to as the heat transfer enhancement ratio ($Nu_i^+ = Nu_{i,Flat} / Nu_{i,Circular}$). It has to be noted that the circumference of a flat tube is equal to that of a circular tube in order to establish a valid comparison.

TABLE 6.12 Average Nusselt number for interior modules for in-line arrangements, Pr = 7.0.

H/Da	Re	2nd	3rd	4th	5th
			L/Da = 4		
2	25	15.70	15.46	15.44	15.44
	100	21.06	19.16	18.37	17.99
	400	43.46	37.33	34.88	34.44
3	25	14.19	13.48	13.31	13.27
	100	19.37	17.27	16.21	15.57
	400	35.20	31.17	28.46	26.82
4	25	14.14	13.11	12.74	12.61
	100	19.87	17.44	16.21	15.43
	400	32.67	29.89	27.26	25.59
			L/Da = 5		
2	25	16.57	16.41	16.40	16.40
	100	22.00	20.37	19.69	19.39
	400	46.16	39.72	35.94	33.01
3	25	15.25	14.66	14.54	14.52
	100	20.84	18.74	17.69	17.07
	400	36.07	31.58	29.48	28.14
4	25	15.35	14.41	14.12	14.03
	100	21.54	19.09	17.83	17.05
	400	36.37	31.83	29.41	27.68
			L/Da = 6		
2	25	17.17	17.06	17.06	17.06
	100	23.01	21.45	20.83	20.57
	400	48.11	40.32	36.72	33.62
3	25	16.00	15.53	15.45	15.43
	100	22.04	19.99	18.96	18.37
	400	38.33	33.56	31.43	29.23
4	25	16.23	15.42	15.19	15.13
	100	22.90	20.48	19.23	18.46
	400	38.31	33.24	30.52	28.83

TABLE 6.13 Average Nusselt number for interior modules for staggered arrangements, Pr = 7.0.

H/Da	Re	2nd	3rd	4th	5th
		L/Da = 5			
2	25	15.97	15.83	15.82	15.82
	100	22.05	20.64	20.17	20.00
	400	52.19	41.95	39.98	39.28
3	25	15.32	14.71	14.59	14.56
	100	21.49	19.35	18.37	17.83
	400	36.91	34.43	32.17	31.11
4	25	15.59	14.59	14.29	14.19
	100	22.08	19.57	18.33	17.57
	400	36.33	32.85	30.27	28.87
		L/Da = 6			
2	25	14.54	14.48	14.49	14.49
	100	21.01	19.80	19.36	19.20
	400	40.92	36.81	35.37	34.78
3	25	15.48	15.02	14.95	14.94
	100	22.40	20.31	19.37	18.85
	400	39.06	35.19	33.11	32.12
4	25	16.36	15.46	15.22	15.16
	100	23.57	21.01	19.77	19.00
	400	38.66	34.63	32.15	30.79
		L/Da = 7			
2	25	13.53	13.52	13.54	13.55
	100	20.26	19.24	18.85	18.70
	400	38.92	35.19	33.71	33.09
3	25	15.16	14.84	14.81	14.81
	100	22.51	20.66	19.79	19.31
	400	40.35	35.64	33.50	32.40
4	25	16.54	15.82	15.65	15.61
	100	24.29	21.85	20.65	19.92
	400	40.76	35.81	33.28	31.81

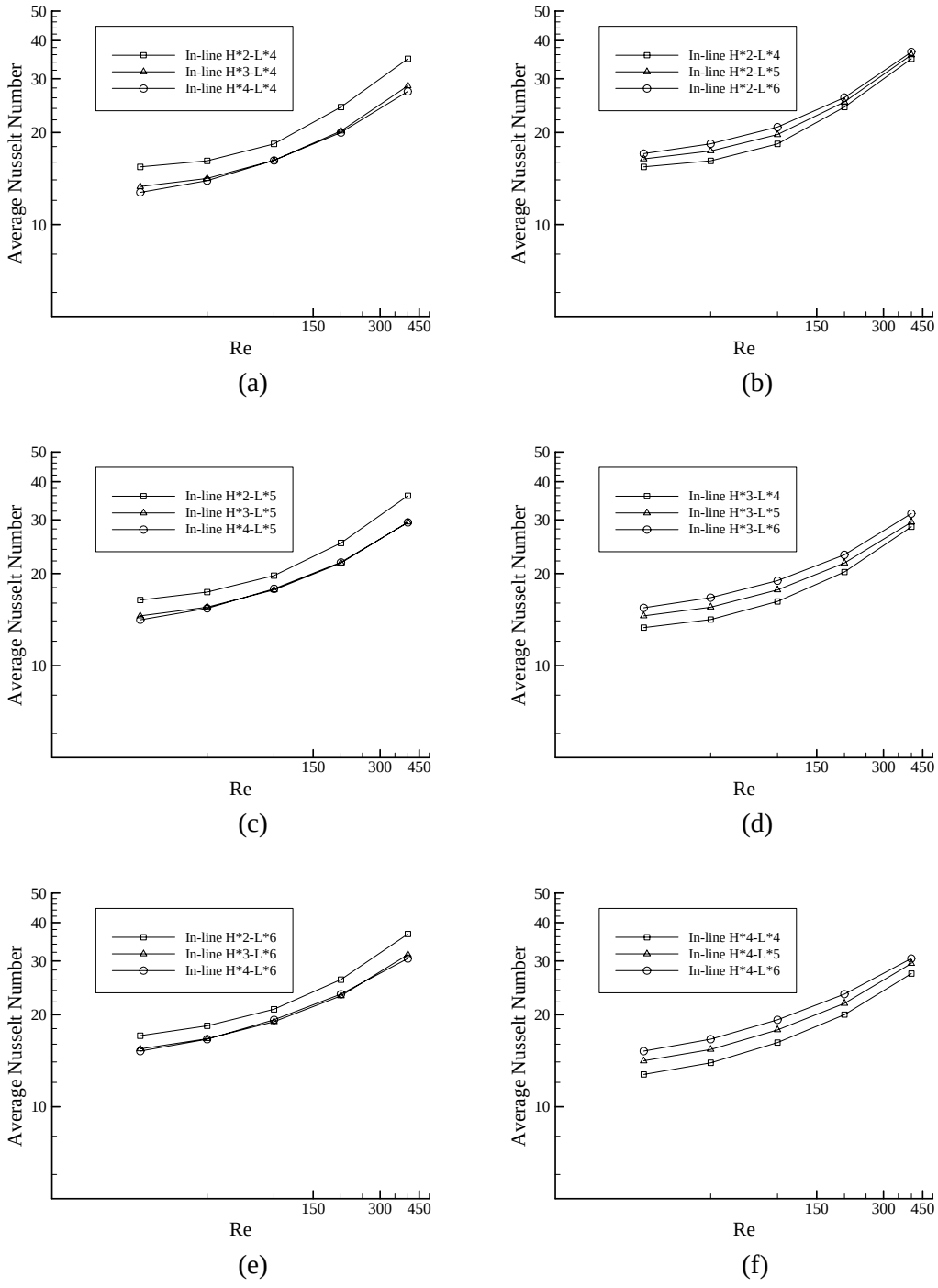

Fig. 6.34 Average Nusselt number for the fourth module, Pr = 7.0, for in-line arrangements: (a) In-line L*4, (b) In-line H*2, (c) In-line L*5, (d) In-line H*3, (e) In-line L*6, and (f) In-line H*4 configurations.

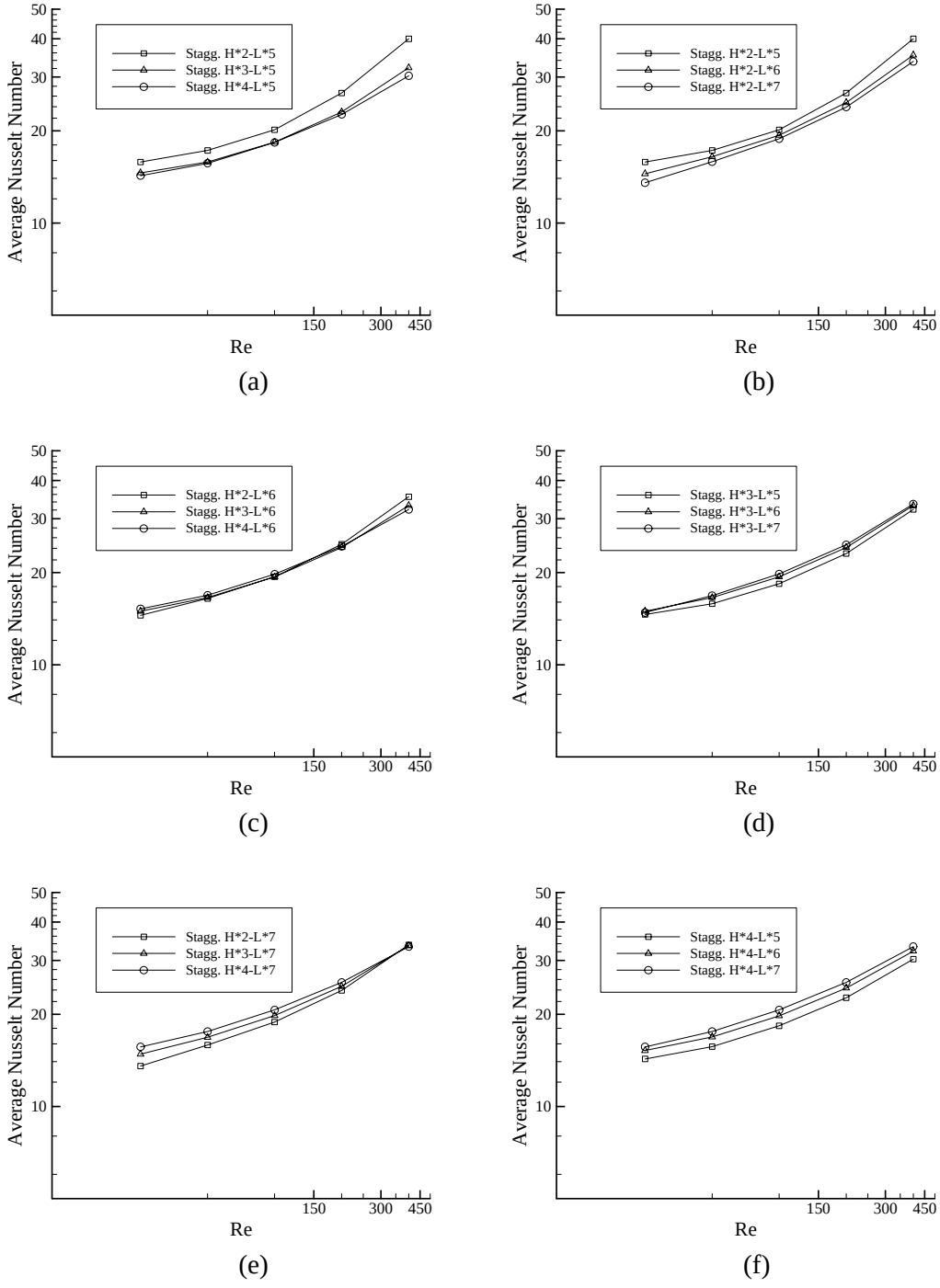

Fig. 6.35 Average Nusselt number for the fourth module, Pr = 7.0, for staggered arrangements: (a) Stagg. L*5, (b) Stagg. H*2, (c) Stagg. L*6, (d) Stagg. H*3, (e) Stagg. L*7, and (f) Stagg. H*4 configurations.

Table 6.14 shows the heat transfer enhancement ratio of the fourth module for both in-line and staggered configurations with fixed height ratio (*H/Da* = 3) and length ratio (*L/Da* = 5 and 6). The heat transfer enhancement ratio is less than unity which indicates that circular tubes out performs flat tubes. The heat transfer enhancement ratio decreases with an increase in Reynolds number, signifying that the increase in the Nusselt number is higher for circular tubes when compared to flat tubes. As expected the staggered configurations perform better than the in-line configurations from a heat transfer point of view.

The effectiveness of using flat tubes can also be studied by evaluating the heat transfer performance ratio. The heat transfer performance ratio is defined as the ratio of heat transfer enhancement to unit increase in pumping power, which can be written as: ($Nu_i^* = Nu_i^+ / (f_{i,Flat} / f_{i,Circular})^{1/3}$). The friction factors are raised to the one-third power as the pumping power is proportional to the one-third power of the friction factor. For applications wherein the pumping ratio is of concern the heat transfer performance ratio should be greater than unity. As evident from Table 6.15 this ratio is always higher than one, signifying the importance of such an application from the pumping power point of view.

TABLE 6.14 Heat transfer enhancement ratio (Nu^{+}).

Re	In-line H*3-L*5	In-line H*3-L*6	Stagg. H*3-L*5	Stagg. H*3-L*6
25	0.942	0.937	0.944	0.972
50	0.932	0.929	0.931	0.955
100	0.918	0.922	0.918	0.939
200	0.881	0.896	0.889	0.912
400	0.833	0.830	0.785	0.891

TABLE 6.15 Heat transfer performance ratio (Nu^{*}).

Re	In-line H*3-L*5	In-line H*3-L*6	Stagg. H*3-L*5	Stagg. H*3-L*6
25	1.154	1.143	1.105	1.056
50	1.165	1.154	1.116	1.070
100	1.175	1.180	1.140	1.096
200	1.152	1.172	1.144	1.125
400	1.067	1.131	1.065	1.323

CHAPTER VII

SUMMARY AND CONCLUSIONS

7.1 Review of the Dissertation

Initially, available relevant literature on the subject was explored. Then, the explanation of covariant and contravariant base vectors were summarized followed by a brief discussion about dependent variable selection in momentum equations. The appropriate choice of grid arrangement was presented. Following that, the theory of coordinate transformations was outlined as well as a detailed explanation of the mathematical formulation adopted in this study was presented. The numerical procedures were validated with several test problems available in the literature.

Finally, a detailed numerical study was conducted on a two-dimensional flow and heat transfer over flat tube bundles found in heat exchanger applications. Both in-line and staggered arrangements were considered in the study. The effects of the Reynolds number (Re), Prandtl number (Pr), length ratio (L/Da), and height ratio (H/Da) on the developing velocity profiles, streamlines, isotherms, pressure drops, and module average Nusselt numbers (Nu) were examined.

7.2 Conclusions

As the Reynolds number increases the maximum velocity in the passage between the upper and lower tubes increases, while the negative velocity downstream, right

behind the tubes, increases in magnitude. The increase in the negative velocity is a direct result of conservation of mass. The maximum velocity in the flow passage considerably decreases with an increase in height ratio for a fixed Reynolds number. The maximum velocity decreases as the length ratio increases.

Flow is observed to attain a periodically fully developed profile downstream of the first module (the fourth in a few cases). The strength and size of the recirculation itself gets larger as the Reynolds number increases in all cases considered in this study. The separated flow covers a smaller portion of the flow field, right behind the tubes, at lower Reynolds numbers (Re = 50). At higher Reynolds numbers (Re = 200 or 400) the area between two consecutive tubes gets covered by the recirculation bubble. An interesting observation was found when staggered configurations were studied. An increase in the spacing between the upper and lower tubes would decrease the recirculation bubble downstream of the upper tube up to a value of 6 and then again increase to a value of 7. As the height ratio increases, the strength and size of the recirculation decreases. The increase in length ratio does not significantly impact the strength and size of the recirculation.

Isotherms show that the colder fluid comes in contact with the hot tube surface as the Reynolds number increases. Accordingly heat transfer increases with an increase in the Reynolds number. As the height ratio increases, the colder isotherms shift farther from the hot tube surface which implies a lower heat transfer. A small change in the heat transfer rate can be predicted since the isotherms have almost the same behavior when the length ratio is increased. The most drastic changes (i.e., increase) on isotherms took

place with an increase in Pr. In general, it is advantageous to use a higher Pr fluid for better heat transfer.

Numerical data for the dimensionless pressure difference for the interior modules shows that the values are nearly constant for a given Reynolds number and a fixed set of geometric ratios. Minor variations were detected for the first and the last modules due to end effects. In all cases, non-dimensionalized pressure drop monotonically decreased with an increase in Reynolds number. The length ratio was found to have very little or even negligible effect on dimensionless pressure drop.

The computed module average Nusselt number at Pr = 0.7 for both in-line and staggered arrangements are nearly constant for a given Reynolds number and the geometric ratios for all inner modules due to the existence of a periodically fully developed flow condition. In general, the module average Nusselt number increases with an increase in the Reynolds number. The results at Pr = 7.0 indicate an increase in the computed module average Nusselt number when compared to those for Pr = 0.7. For both in-line and staggered configuration, the flow did not attain a periodically fully developed condition at Pr = 7.0 and Re = 400.

The overall performance of the in-line configuration for lower height ratio (*H/Da* = 2) and higher length ratio (*L/Da* = 6) is preferable since it provides a higher heat transfer rate for all Reynolds numbers except for the lowest Re value of 25. The heat transfer enhancement ratio is less than unity which indicates that circular tubes out perform flat tubes from a heat transfer point of view. However, the heat transfer performance ratio is always higher than one, signifying the importance of such

application from the pumping power point of view. As expected the staggered configurations perform better than the in-line configurations from a heat transfer point of view.

7.3 Recommendations for Future Studies

Useful extensions to the present work could be achieved by implementing the following suggestions:

1. Since the present study is limited to two-dimensional analysis, future study can be devoted to obtaining the flow and heat transfer performances of a three-dimensional system.
2. Modify the formulation to accommodate an unstructured grid, in which context the use of more advanced linear system solvers like the conjugate gradient method could be explored.
3. Extend the analysis to the computation of transient flow.
4. Since this study considered the developing flow of a repeated geometry, it required a large number of grid points. This problem can be solved by using the Periodically Developed Flow (PDF) formulation.

REFERENCES

Breuer, M., 1998. Numerical and modeling influences on large eddy simulation for the flow past a circular cylinder. Int. J. Heat Fluid Flow 19, 512-521.

Breuer, M., Bernsdorf, J., Zeiser, T., Durst, F., 2000. Accurate computations of the laminar flow past cylinder based on two different methods: lattice-boltzmann and finite-volume. Int. J. Heat Fluid Flow 21, 186-196.

Chang, Y., Beris, A.N., Michaelides, E.E., 1989. A numerical study of heat and momentum transfer for tube bundles in cross-flow. Int. J. Num. Methods in Fluids 9, 1381-1394.

Chen, Chiun-Hsun, Weng, Fang-Bor, 1990. Heat transfer for incompressible and compressible fluid flows over a heated cylinder. Num. Heat Transfer, Part A 18, 325-349.

Chen, Y., Fiebig, M., Mitra, N.K., 1998a. Conjugate heat transfer of a finned oval tube part a: flow patterns. Num. Heat Transfer, Part A 33, 371-385.

Chen, Y., Fiebig, M., Mitra, N.K., 1998b. Conjugate heat transfer of a finned oval tube part a: flow patterns. Num. Heat Transfer, Part A 33, 387-401.

Demirdzic, I., 1982. A finite volume method for computational of fluid flow in complex geometries. Ph.D. Thesis, Imperial College, London.

Demirdzic, I., Gosman, A.D., Issa, R.I., 1980. A finite volume method for the prediction of turbulent flow in arbitrary geometries. Lecture Notes in Physics 141, Springer-Verlag, Berlin Heidelberg, Germany, 144-150.

Demirdzic, I., Gosman, A.D., Issa, R.I., Peric, M., 1987. A calculation procedure for turbulent flow in complex geometries. Comput. Fluids 15, No. 3, 251-273.

Faghri, M., Sparrow, E.M., Prata, A.T., 1984. Finite difference solutions of convection diffusion problems in irregular domains using a non-orthogonal coordinate transformation. Num. Heat Transfer, Part B 7, 183-209.

Ferziger, J.H., Peric, M., 1996. Computational Methods for Fluid Mechanics. Springer-Verlag, Berlin Heidelberg, Germany.

Gordon, W.J., Hall, C.A., 1973. Construction of curvilinear coordinate systems and applications to mesh generation. Int. J. Num. Methods in Engineering 7, 461-477.

Grannis, V.B., Sparrow, E.M., 1991. Numerical simulation of fluid flow through an array of diamond-shaped pin fins. Num. Heat Transfer, Part A 19, 381-403.

Hoffman, J.D., 1992. Numerical Methods for Engineers and Scientists. McGraw-Hill, Inc., New York.

Hsu, F.H., 1981. A curvilinear coordinate method for momentum, heat and mass transfer in domains of irregular geometry. Ph.D. thesis, University of Minnesota, Minneapolis, MN.

Hung, T.K., Brown T.D., 1977. An implicit finite difference method for solving the navier-stokes equation using orthogonal curvilinear coordinates. J. Comput. Physics, 23, 343-365.

Incropera, F.P., DeWitt, D.P., 1996. Fundamentals of Heat and Mass Transfer. John Wiley & Sons, Inc., New York.

Kadja, M., 1987. Computation of recirculating flow in complex domains with algebraic reynolds stress closure and body-fitted meshes. Ph.D. thesis, University of Manchester, Manchester, England.

Karki, K., 1986. A calculation procedure for viscous flows at all speeds in complex geometries. Ph. D. Dissertation, University of Minnesota.

Karki, K.C., Patankar, S.V., 1988. Calculation procedure for viscous incompressible flow in complex geometries. Num. Heat Transfer, 14, 295-307.

Kundu, D., 1989. Computational and experimental studies of flow filed and heat transfer from a row of in-line cylinders centered between two parallel plates. Ph. D. thesis, University of Texas at Arlington, Texas.

Kundu, D., Haji-Sheikh, A., Lou, D.Y.S., 1991a. Heat transfer predictions in cross flow over cylinders between two parallel plates. Num. Heat Transfer, Part A, 19, 361-377.

Kundu, D., Haji-Sheikh, A., Lou, D.Y.S., 1991b. Pressure and heat transfer in cross flow over cylinders between two parallel plates. Num. Heat Transfer, Part A, 19, 345-360.

Maliska, C. R. Raithby, G. D., 1984. A method for computing three-dimensional flows using non-orthogonal boundary-fitted coordinates. Int. J. Num. Methods Fluids, 4, 519-537.

Napolitano, M., Orlandi, P., 1985. Laminar flow in complex geometry: A comparison. Int. Journal Num. Methods in Fluids, 5, 667-683.

Niceno, B., Nobile, E., 2001. Numerical analysis of fluid flow and heat transfer in periodic wavy channel. Int. J. Heat Fluid Flow, 22, 156-167.

Nishimura, T., Murakami, S., Arakawa, S., Kawamura, Y., 1990. Flow observation and mass transfer characteristics in symmetrical wavy-walled channels at moderate reynolds numbers for steady flow. Int. J. Heat Mass Transfer, 33, 835-845.

Ota, T., Nishiyama, H., Taoka, Y., 1984. Heat transfer and flow around an elliptic cylinder. Int. J. of Heat and Mass Transfer, 27 (10), 1771-1779.

Ota, T., Nishiyama, H., Kominami, J., Sato, K., 1986. Heat transfer two elliptic cylinder in tandem arrangement. J. Heat Transfer, 108, 525-531.

Patankar, S.V. 1980. Numerical Heat Transfer and Fluid Flow. McGraw-Hill, Inc., New York.

Patankar, S.V., Spalding, D.B., 1972. A calculation procedure for heat, mass and momentum transfer in three-dimensional parabolic flow. Int. J. Heat Mass Transfer, 15, 1787.

Peric, M., 1985. Finite volume method for the prediction of three-dimensional fluid flow in complex duct. Ph.D. thesis, Imperial College, London.

Raithby, G.D., Galpin, P.F., Van Doormal, J.P., 1986. Prediction of heat and fluid flow in complex geometries using general orthogonal coordinates. Num. Heat Transfer, Part B, 9, 125-142.

Rhie, C.M., Chow, W.L., 1983. Numerical study of turbulent flow past an airfoil with trailing edge separation. AIAA J., 10, 131-146.

Sharatchandra M.C., 1995. A strongly conservative finite volume formulation for fluid flows in complex geometries using contravariant velocity components. Ph. D. Dissertation, Texas A&M University.

Sharatchandra, M.C., Rhode, D.L., 1994a. A new strongly conservative finite-volume formulation for fluid flows in irregular geometries using contravariant velocity components. Part 1-Theory, Num. Heat Transfer, Part B, 26, 39-52.

Sharatchandra, M.C., Rhode, D.L., 1994b. A new strongly conservative finite-volume formulation for fluid flows in irregular geometries using contravariant velocity components. Part 2-Assesment, Num. Heat Transfer, Part B, 26, 53-62.

Shyy, W., Tong, S.S., Correa, S. M., 1985. Numerical recirculating flow calculation sing a body-fitted coordinate system. Num. Heat Transfer, Part A, 8, 99-113.

Shyy, W., Correa, S.M., Braaten, M. E., 1988. Computation of flow in gas turbine combustor. Combust. Sci. Technol., 58, No. 1-3, 97-117.

Shyy, W., Vu, T.G., 1991. On the adaption of velocity variable and grid system for fluid flow in curvilinear coordinate. J. Comput. Phys., 92, 82-105.

Steger, J.L., Sorenson, R.L., 1980. Use of hyperbolic partial differential equations to generate body-fitted coordinates. Num. Grid Generation Techniques, NASA conference publication 2166, Hampton, Va.

Thomas P.P., Middecoff J.F., 1980. Direct control of the grid point distribution in the meshes generated by elliptic equations. AIAA Journal, 18, No. 6, 652-656.

Thompson, J.F., 1982. Numerical Grid Generation. North-Holland, New York.

Thompson, J.F., Warsi, Z.U., Mastin, C. W., 1985. Numerical Grid Generation, Foundation and Applications. North-Holland, New York.

Versteeg, H.K., Malalasekera, W., 1995. An Introduction to Computational Fluid Dynamics the Finite Volume Method. Longman Scientific & Technical, New York.

Wang, G., Vanka S.P., 1995. Convective heat transfer in wavy passage. Int. J. Heat Mass Transfer, 38, 3219-3230.

Webb, R.L., 1993. Principles of Enhanced Heat Transfer. John Wiley & Sons, Inc., New York.

Williamson, C.H.K., 1996. Vortex dynamics in the cylinder wake. Annu. Rev. Fluid Mech. 28, 477-539.

Wung, T., Niethammer, J., Chen, C. 1986. Measurements of heat-mass transfer and pressure drop for some non-standard arrays of tubes in cross flow. In: Tien, C., Carey, V., Ferrell, J. (Eds.), Heat Transfer 1986, Proceedings of the Eighth International Heat Transfer Conference. Hemisphere, San Francisco, pp. 1041-1046.

Yang, H.Q., Yang, K.T., Lloyd, J.R., 1988. Buoyant flow calculations with non-orthogonal curvilinear co-ordinates for vertical and horizontal parallelepiped enclosures. Int. J. Num. Meth. Eng., 25, 331-345.

Yang, H.Q., Yang, K.T., Lloyd, J.R., 1990. A control volume finite difference method for buoyant flow in three-dimensional curvilinear non-orthogonal coordinates. Int. J. Num. Meth. Fluids, 10, 199-211.

Yu, D., Barron, R.F., Ameel, T.A., Warrington, R.O., 1995. Mixed convection from horizontal tube banks between two vertical parallel plates. Num.Heat Transfer, Part A, 27, 473-486.

Zdrakovich, M.M., 1997. Flow Around Circular Cylinders, 1: Fundamentals. Oxford University Press, New York.

APPENDIX A

CONTROL VOLUME FORMULATION

The control volume integration, which represents the main step of the finite volume technique, yields the following form:

$$\int_A \vec{J} \bullet \vec{e}^{\chi} ds = \int_V S dV \tag{A.1}$$

The LHS of the above equation represents the total integrated fluxes through the control surfaces, which can be rewritten as:

$$\int_A \vec{J} \bullet \vec{e}^{\chi} ds = J_e + J_w + J_n + J_s \tag{A.2}$$

where the terms J_e, J_w, J_n and J_s are the fluxes through each face of the elementary cell shown in Fig. 4.2. The methodology that will be followed to derive the mathematical expression for each one of these terms is similar. Since (J_e) was derived earlier, (J_n) is derived below:

$$J_n = \int_{A_{II}} \vec{J} \bullet \vec{e}^{\eta} ds \tag{A.3}$$

where $\vec{e}^{\eta}$ is the unit normal vector, mentioned earlier in Section 3.1.2, to A_{II} surface.

Recall that,

$$\vec{e}^{\eta} = \frac{\frac{\partial x}{\partial \xi}\vec{e}_y - \frac{\partial y}{\partial \xi}\vec{e}_x}{h_{\xi}} \tag{A.4}$$

and ds is the length of elemental arc and can be expressed as $ds = h_{\xi} d\xi$. The total flux $\vec{J}$ can be written mathematically in vector notation as:

$$\vec{J} = J_x\vec{e}_x + J_y\vec{e}_y = \left(\rho u\phi - \Gamma\frac{\partial \phi}{\partial x}\right)\vec{e}_x + \left(\rho v\phi - \Gamma\frac{\partial \phi}{\partial y}\right)\vec{e}_y \tag{A.5}$$

substituting Equations (A.4) and (A.5) into Equation (A.3) to obtain

$$J_n = \int_{A_{II}}\left[\rho\left(v\frac{\partial x}{\partial \xi} - u\frac{\partial y}{\partial \xi}\right)\phi - \Gamma\left(\frac{\partial \phi}{\partial y}\frac{\partial x}{\partial \xi} - \frac{\partial \phi}{\partial x}\frac{\partial y}{\partial \xi}\right)\right]d\xi \tag{A.6}$$

The gradients of a generic scalar field ϕ are expressed in Cartesian coordinates and need to be represented by their counterparts in the transformed (ξ, η) physical plane. This can be accomplished by using the Chain-Rule as follows:

$$\frac{\partial \phi}{\partial x} = \frac{1}{Ja}\left(\frac{\partial y}{\partial \eta}\frac{\partial \phi}{\partial \xi} - \frac{\partial y}{\partial \xi}\frac{\partial \phi}{\partial \eta}\right) \tag{A.7}$$

$$\frac{\partial \phi}{\partial y} = \frac{1}{Ja}\left(\frac{\partial x}{\partial \xi}\frac{\partial \phi}{\partial \eta} - \frac{\partial x}{\partial \eta}\frac{\partial \phi}{\partial \xi} \right) \tag{A.8}$$

Substituting these relationships (Eqs. A.7 and A.8) into Equation A.6 and with some mathematical manipulations, the following expression is obtained:

$$J_n = \left(\rho u^{\eta} h_{\xi} \phi \right)_n \Delta\eta - \frac{h_{\xi}^2 h_{\eta} \Delta\xi}{Ja}\left(\frac{\Gamma}{h_{\eta}}\frac{\partial \phi}{\partial \eta} \right)_n + \frac{h_{\xi}^2 h_{\eta} \Delta\xi}{Ja}\left(\vec{e}_{\xi} \bullet \vec{e}_{\eta} \right)\left(\frac{\Gamma}{h_{\xi}}\frac{\partial \phi}{\partial \xi} \right)_n \tag{A.9}$$

The third term in the RHS of the above equation contains the value of $\left(\vec{e}_{\xi} \bullet \vec{e}_{\eta} \right)$ which appears due to the non-orthogonality of the coordinate system and would disappear for an orthogonal system. This value can be represented mathematically as follows:

$$\vec{e}_{\xi} \bullet \vec{e}_{\eta} = \vec{e}^{\,\xi} \bullet \vec{e}^{\,\eta} = \frac{\dfrac{\partial x}{\partial \xi}\dfrac{\partial x}{\partial \eta} + \dfrac{\partial y}{\partial \xi}\dfrac{\partial y}{\partial \eta}}{h_{\xi} h_{\eta}} \tag{A.10}$$

Equation (A.9) can be rewritten in terms of Primary and Secondary fluxes as:

$$J_n = J_{P,n} - J_{S,n} \tag{A.11}$$

where

$$J_{P,n} = \left(\rho u^{\eta} h_{\xi} \phi\right)_n \Delta\xi - \alpha_{\eta,n} \left(\frac{\Gamma}{h_{\eta}} \frac{\partial \phi}{\partial \eta}\right)_n \tag{A.12}$$

$$J_{S,n} = -\beta_{\eta,n} \left(\frac{\Gamma}{h_{\xi}} \frac{\partial \phi}{\partial \xi}\right)_n \tag{A.13}$$

$$\alpha_{\eta} = \frac{h_{\xi}^2 h_{\eta} \Delta\xi}{Ja} \tag{A.14}$$

$$\beta_{\eta} = \alpha_{\eta} \left(\vec{e}_{\xi} \bullet \vec{e}_{\eta}\right) \tag{A.15}$$

APPENDIX B

PRIMARY FLUXES USING POWER-LAW SCHEME

Following Patankar's (1980) formulation, the primary fluxes J_P which combines both convective and diffusive fluxes is evaluated by using a polynomial expression in terms of the cell Peclet number. The following is the primary flux at each interface:

$$J_{P,e} = F_e\phi_E + A(|P_e|)D_e(\phi_P - \phi_E) \tag{B.1}$$

$$J_{P,w} = F_w\phi_W + A(|-P_w|)D_w(\phi_W - \phi_P) \tag{B.2}$$

$$J_{P,n} = F_n\phi_N + A(|P_n|)D_n(\phi_P - \phi_N) \tag{B.3}$$

$$J_{P,s} = F_s\phi_S + A(|P_s|)D_s(\phi_S - \phi_P) \tag{B.4}$$

where $A(|P|)$ is the polynomial expression defined by Patankar (1980) as:

$$A(|P_e|) = \max\left[\left[0,\left(1-0.1|P_e|^5\right)\right]\right] \tag{B.5}$$

$$A(|P_w|) = \max\left[\left[0,\left(1-0.1|P_w|^5\right)\right]\right] \tag{B.6}$$

$$A(|P_n|) = \max\left[\left[0,\left(1-0.1|P_n|^5\right)\right]\right] \tag{B.7}$$

$$A\left(\left|P_s\right|\right) = \max\left[\left[0, \left(1 - 0.1\left|P_s\right|^5\right)\right]\right] \tag{B.8}$$

The non-dimensional cell Peclet number, P, is defined as the measure of the relative strengths of the flow rate through a control surface, F, and the diffusional conductance, D, as follows:

$$P_e = \frac{F_e}{D_e} \tag{B.9}$$

$$P_w = \frac{F_w}{D_w} \tag{B.10}$$

$$P_n = \frac{F_n}{D_n} \tag{B.11}$$

$$P_s = \frac{F_s}{D_s} \tag{B.12}$$

where

$$F_e = \left(\rho u^{\xi} h_{\eta}\right)_e = \rho_e \left(\alpha_{\xi} u_{\xi} - \beta_{\xi} u_{\eta}\right)_e \tag{B.13}$$

$$F_w = \left(\rho u^{\xi} h_{\eta}\right)_w = \rho_w \left(\alpha_{\xi} u_{\xi} - \beta_{\xi} u_{\eta}\right)_w \tag{B.14}$$

$$F_n = \left(\rho u^{\eta} h_{\xi}\right)_n = \rho_n \left(\alpha_{\eta} u_{\eta} - \beta_{\eta} u_{\xi}\right)_n \tag{B.15}$$

$$F_s = \left(\rho u^{\eta} h_{\xi}\right)_s = \rho_s \left(\alpha_{\eta} u_{\eta} - \beta_{\eta} u_{\xi}\right)_s \tag{B.16}$$

and

$$D_e = \left(\frac{\Gamma \alpha_\xi}{h_\xi} \right)_e \tag{B.17}$$

$$D_w = \left(\frac{\Gamma \alpha_\xi}{h_\xi} \right)_w \tag{B.18}$$

$$D_n = \left(\frac{\Gamma \alpha_\eta}{h_\eta} \right)_n \tag{B.19}$$

$$D_s = \left(\frac{\Gamma \alpha_\eta}{h_\eta} \right)_s \tag{B.20}$$

VITA

Haitham M. S. Bahaidarah was born in Makkah Al-Mukkarrmah, Saudi Arabia (Jan. 1974). He earned his B.S. (Jan. 1996) in mechanical engineering from King Fahd University of Petroleum and Minerals (KFUPM), Dhahran, Saudi Arabia. After that, he worked as a Graduate Assistant in the Department of Mechanical Engineering of the same university (KFUPM) until May 1999. During the same time, he managed to pursue and earn his M.S. degree in mechanical engineering. Then, he was promoted to a Lecturer in the same department. Haitham joined Texas A&M University in College Station, Texas for his Ph.D. in August 1999. He was a Graduate Student at the Numerical Heat Transfer Laboratory and completed his Ph.D. program in August 2004.

Permanent Mailing Address:

Haitham M. S. Bahaidarah
Department of Mechanical Engineering
King Fahd University of Petroleum and Minerals
Dhahran, 31261 Saudi Arabia